

**Multimodal Series Elastic Actuator for Human-Machine Interaction
with Applications in Robot-Aided Rehabilitation**

by

Brayden DeBoon

A thesis submitted to the School of Graduate and Postdoctoral Studies in partial
fulfillment of the requirements for the degree of

Master of Applied Science in Mechanical Engineering

Faculty of Engineering and Applied Science
Ontario Tech University
Oshawa, Ontario, Canada
December, 2019

©Brayden DeBoon, 2019

THESIS EXAMINATION INFORMATION

Submitted by: **Brayden DeBoon**

Master of Applied Science in Mechanical Engineering

Thesis Title: Multimodal Series Elastic Actuator for Human-Machine Interaction with Applications in Robot-Aided Rehabilitation
--

An oral defense of this thesis took place on December 3, 2019 in front of the following examining committee:

Examining Committee:

Chair of Examining Committee	Dr. Martin Agelin-Chaab
Research Supervisor	Dr. Carlos Rossa
Research Co-supervisor	Dr. Scott Nokleby
Examining Committee Member	Dr. Jaho Seo
Thesis Examiner	Dr. Shahryar Rahnamayan

The above committee determined that the thesis is acceptable in form and content and that a satisfactory knowledge of the field covered by the thesis was demonstrated by the candidate during an oral examination. A signed copy of the Certificate of Approval is available from the School of Graduate and Postdoctoral Studies.

ABSTRACT

Series elastic actuators (SEAs) are becoming an elemental building block in collaborative robotic systems. They introduce an elastic element between the mechanical drive and the end-effector, making otherwise rigid structures compliant when in contact with humans. Topologically, SEAs are more amenable to accurate force control than classical actuation techniques, as the elastic element may be used to provide a direct force estimate. The compliant nature of SEAs provides the potential to be applied in robot-aided rehabilitation.

This thesis proposes the design of a novel SEA to be used in robot-aided musculoskeletal rehabilitation. An active disturbance rejection controller is derived and experimentally validated and multiobjective optimization is executed to tune the controller for best performance in human-machine interaction. This thesis also evaluates the constrained workspaces for individuals experiencing upper-limb musculoskeletal disorders. This evaluation can be used as a tool to determine the kinematic structure of devices centred around the novel SEA.

AUTHOR'S DECLARATION

I hereby declare that this thesis consists of original work of which I have authored. This is a true copy of the thesis, including any required final revisions, as accepted by my examiners.

I authorize Ontario Tech University to lend this thesis to other institutions or individuals for the purpose of scholarly research. I further authorize Ontario Tech University to reproduce this thesis by photocopying or by other means, in total or in part, at the request of other institutions or individuals for the purpose of scholarly research. I understand that my thesis will be made electronically available to the public.

STATEMENT OF CONTRIBUTIONS

Part of the work described in Chapter 2 has been submitted for potential publication to *ASME Journal of Biomechanical Engineering* as:

B. DeBoon, R. Foley, N. La Delfa, S. Nokleby, and C. Rossa, “9 Degree-of-Freedom Kinematic Modelling of the Upper Limb Complex for Constrained Workspace Evaluation.”

Part of the work described in Chapter 3 has been published as:

B. DeBoon, S. Nokleby, N. La Delfa, and C. Rossa, “Differentially- Clutched Series Elastic Actuator for Robot-Aided Musculoskeletal Rehabilitation,” in *2019 International Conference on Robotics and Automation (ICRA)*. IEEE, 2019, pp. 1507–1513.

Part of the work described in Chapter 4 has been submitted to the *2020 IEEE International Conference on Robotics and Automation (ICRA)* as:

B. DeBoon, S. Nokleby, and C. Rossa, “Backlash-Compensated Active Disturbance Rejection Control of Nonlinear Multi-Input Series Elastic Actuators.”

At the time of writing, part of the work described in Chapter 5 has been accepted for publication as:

B. DeBoon, B. Kent, M. Lacki, S. Nokleby, and C. Rossa, “Multi-Objective Gain Optimizer for an Active Disturbance Rejection Controller” in *2019 IEEE Global Conference on Signal and Information Processing (GlobalSIP)*. IEEE, 2019.

Finally, at the time of writing, components of Chapter 4 and Chapter 5 are to be submitted to *IEEE/ASME Transactions on Mechatronics* as:

B. DeBoon, S. Nokleby, and C. Rossa, “Gain Selection for Multi-Input Series Elastic Actuator Active Disturbance Rejection Controllers”

ACKNOWLEDGEMENTS

I would like to start by sincerely thanking my supervisors, Dr. Carlos Rossa and Dr. Scott Nokleby, for transforming my way of thinking and for accommodating my seemingly consistent short-notice revision requests. There have been many weekends sacrificed by my supervisors in selfless acts to push for my success and I am forever grateful for their efforts. In addition to this, my supervisors have been more than exceptional in remaining active in my quest for ongoing learning, through the research conducted in this thesis to my various tangents in personal projects. The wisdom I have obtained throughout the past two years is dear to me and I could not have done it without them.

I would also like to thank my parents, Mike and Lana, for their consistent support though my various escapades. Without their continued enthusiasm to push me to become the best version of myself, I would not be the man I am today. I am privileged to have these two distinguished figures as examples throughout my life, as the traits obtained from my father's work ethic to my mother's mind are equally aggregated toward my success.

Thanks to all of my friends and extended family - my grandparents, aunts, uncles, and cousins, all of which provided love and support through this degree, and my brother Skyler, for always having my back.

Finally, I would like to thank my best friend and girlfriend, Kourtney Doucette, for her patience, love, and support over the many years. I cannot begin to express my appreciation for all of the phone calls and trips across the country that helped keep me sane.

Table of Contents

ABSTRACT	i
AUTHOR’S DECLARATION	ii
STATEMENT OF CONTRIBUTIONS	iii
ACKNOWLEDGEMENTS	iv
1 Introduction	1
1.1 Introduction	1
1.2 Robot-Assisted Rehabilitation	2
1.3 Devices Designed for Human-Machine Interaction	4
1.4 Active Actuation Sources	6
1.5 Series Elastic Actuators	8
1.5.1 Hybrid Elastic Actuators	10
1.5.2 Parallel Elastic Actuators	10
1.5.3 Multimodality	11
1.5.4 Clutched Elastic Actuators	11
1.6 Proposed Series Elastic Actuator	12
1.7 Series Elastic Actuator Torque Control	12
1.8 Objectives and Outline	13
2 9-DOF Human Arm Model for Workspace Evaluation with Constrained Inverse Kinematics	15
2.1 Introduction	15
2.2 Forward Kinematics of the Upper Limb	16
2.2.1 Task Space Vector Formulation	18
2.2.2 Forward Kinematics	19
2.3 Constrained Differential Inverse Kinematics	20
2.4 Experimental Validation	23
2.4.1 Data Collection	24
2.4.2 Model Identification	25

2.4.3	Scenario 1 Experimental Results	27
2.4.4	Scenario 2 Experimental Results	29
2.4.5	Scenario 3 Experimental Results	32
2.5	Conclusions	34
3	Design of the Differentially-Clutched Series Elastic Actuator	36
3.1	Introduction	36
3.2	Differential Clutch	37
3.3	Proof-of-Concept	39
3.4	Equations of Motion	41
3.4.1	Free Motion	43
3.4.2	Elastic Mode	44
3.4.3	Active and Resistive Mode	44
3.5	Experimental Results	45
3.5.1	Characterization and Model Identification	46
3.5.2	Model Validation	46
3.5.3	Torque Control Through Spring Deflection	48
3.5.4	Discussion	49
3.6	Conclusions	50
4	Active Disturbance Rejection Controller	52
4.1	Introduction	52
4.2	MIMO Series Elastic Actuator Modelling	54
4.3	Backlash Estimation and Compensation	57
4.4	Multi-Input Active Disturbance Rejection Torque Controller	58
4.4.1	Reference and Transient Output Torque Profiles	58
4.4.2	Nonlinear Weighted Feedback Combiner	60
4.4.3	Extended State Disturbance Observer	61
4.4.4	Control Law	65
4.5	Experimental Results	66
4.6	Conclusions	68
5	Multi-Objective Controller Optimization	71
5.1	Introduction	71
5.2	Reference Point Dominance-Based Nondominated Sorting Genetic Algorithm	72
5.2.1	Convergence and Diversity	73

5.2.2	Reference Points and Distance Measures	74
5.2.3	RP-Dominance and Non-RPD-Dominated Sorting	75
5.3	Performance Objectives for ADRC	77
5.3.1	ADRC Tunable Parameters	79
5.4	Optimizer Validation	80
5.4.1	Validation Results	82
5.5	Multiobjective Optimization of the Differentially-Clutched Series Elastic Actuator Controller	83
5.5.1	Simulation Results	84
5.6	Experimental Results	84
5.6.1	Tracking Error	84
5.6.2	Control Effort	85
5.6.3	Percent Overshoot	86
5.6.4	Rise Time	86
5.6.5	Settling Time	88
5.6.6	Maximum Input	88
5.6.7	Steady-State Error	89
5.6.8	Time to Disengagement	90
5.6.9	Number of Input Crossings	91
5.6.10	Multiobjective Results	92
5.7	Conclusions	94
6	Conclusions and Recommendations for Future Work	95
6.1	Conclusions	95
6.2	Recommendations and Future Work	99
	References	100
	Appendices	115

List of Tables

2.1	Modified Denavit-Hartenberg parameters for the 9-DOF upper limb model.	19
2.2	Rigid Body Anatomical Landmarks	25
2.3	Regular range of motion w.r.t ideal rest angle θ_i^0 (anatomical zero)	26
4.1	Active Disturbance Rejection Tuned Parameters	66
5.1	Number of optimizable gains in an ADRC	80
5.2	Optimizer Boundary Conditions	81
5.3	Optimized Gains for the Inverted Pendulum	83
5.4	Optimized Gains for the DC-SEA	84
5.5	Objective Performance Over 500 Generations	85
5.6	Optimized Gains for Tracking Error	85
5.7	Optimized Gains for Controller Effort	86
5.8	Optimized Gains for Percent Overshoot	87
5.9	Optimized Gains for Rise Time	87
5.10	Optimized Gains for Settling Time	88
5.11	Optimized Gains for Maximum Input Value	90
5.12	Optimized Gains for Steady-State Error	91
5.13	Optimized Gains for Disengagement Time	91
5.14	Optimized Gains for Number of Input Crossings	92
5.15	Multiobjective Fitness Values for 5 Members	93
5.16	Optimized Gains for Multiobjective Problem	94

List of Figures

1.1	Rehabilitation timeline and device requirements	4
1.2	Schematic of actuator topologies	9
2.1	9-DOF kinematic model of the human upper-limb complex	17
2.2	Constrained differential inverse kinematics with joint angle limits	20
2.3	9-DOF arm model experimental scenarios	23
2.4	Rigid body and artificial joint limitation setup for experimental measurements	24
2.5	Experimental results for unconstrained joint angle measurements	26
2.6	Experimental and simulated convex hull workspaces	27
2.7	Transverse plane cross-section of simulated and measured constrained and unconstrained workspaces about the sternoclavicular joint	29
2.8	Experimental and simulated slices of the workspaces in transverse-plane cross-sections above the sternoclavicular joint	30
2.9	Experimental and simulated slices of the workspaces in transverse-plane cross-sections below the sternoclavicular joint	31
2.10	Upper-limb workspace evaluation results for constrained wrist to extended sagittal plane	32
2.11	Joint trajectory results for constrained wrist to extended sagittal plane . . .	33
2.12	Upper-limb workspace evaluation results for constrained wrist to offset frontal plane	34
2.13	Joint trajectory results for constrained wrist to offset frontal plane	35
3.1	Operating modes of the differential clutch	38
3.2	Drawing and CAD model of the differential actuator	40
3.3	Dynamics of the differentially-clutched series elastic actuator	42
3.4	Experimental setup for basic operation of the DC-SEA	45
3.5	DC-SEA characterization results in Scenario 1: Static output shaft	47
3.6	Multimodal PID controller block diagram	48

3.7	Experimental results of torque tracking of the DC-SEA in Scenario 1: Static output shaft	49
3.8	Experimental results of torque tracking of the DC-SEA in Scenario 2: Dynamic torque inference through spring deflection	50
4.1	Labeled image of the DC-SEA	53
4.2	Nonlinear backlash diagram for the DC-SEA	57
4.3	Transient profile generated by active disturbance rejection controller	59
4.4	Active disturbance rejection control nonlinear feedback combiner	61
4.5	Block diagram of a simplified active disturbance rejection controller	62
4.6	Active disturbance rejection controller for the multi-input DC-SEA	64
4.7	Results of single-input deflection control with PID, classical ADRC, and backlash compensated ADRC	67
4.8	Results of multi-input control on the spring deflection	68
4.9	Nonlinearities in DC-SEA from sawtooth deflection control	69
5.1	Simple motor controller demonstrating multi-objective optimization	73
5.2	Pareto front definition	74
5.3	RPD-NSGA-II reference points and distance measures	75
5.4	Reference point dominance-based nondominated sorting genetic algorithm block diagram	76
5.5	Demonstration of the optimized objectives	77
5.6	Simplified setup of an inverted pendulum on a cart	81
5.7	Simulated optimization results with emphasis on tracking error	82
5.8	Experimental results of the cart tracking error	83
5.9	Experimental results of spring deflection tracking error after optimization	86
5.10	Experimental results of control effort after optimization	87
5.11	Experimental results of spring deflection percent overshoot after optimization	88
5.12	Experimental results of spring deflection rise time after optimization	89
5.13	Experimental results of spring deflection settling time after optimization	89
5.14	Experimental results of controller maximum input after optimization	90
5.15	Experimental results of steady-state error after optimization	90
5.16	Experimental results of disengagement time after optimization	91
5.17	Experimental results for number of input crossings after optimization	92
5.18	Experimental results for the multiobjective rehabilitation application	93
6.1	Conceptual devices for upper-limb rehabilitation	96

LIST OF ABBREVIATIONS AND SYMBOLS

ADRC	Active disturbance rejection control
CEA	Clutched elastic actuator
DC-SEA	Differentially-clutched series elastic actuator
DOF	Degree-of-freedom
EMF	Electromotive force
ESO	Extended state observer
GA	Genetic algorithm
HMI	Human machine interaction
MIMO	Multi-input, multi-output
MISO	Multi-input, single-output
MSD	Musculoskeletal disorder
NFC	Nonlinear feedback combiner
PD	Proportional-derivative
PEA	Parallel elastic actuator
PID	Proportional-integral-derivative
ROM	Range of motion
RPD-NSGA-II	Reference point dominance-based nondominated sorting genetic algorithm
SEA	Series elastic actuator
SISO	Single-input, single-output
TD	Tracking differentiator

Chapter 2

x, y, z	Three-dimensional Cartesian coordinates
θ_i	Angle of rotation of joint i about axis z_i
$\mathbf{q} \in \mathbb{R}^{9 \times 1}$	Vector of joint space coordinates
$\gamma(q)$	Hand angle w.r.t z_0 (Hand yaw)
$\varphi(q)$	Hand angle w.r.t y_0 (Hand roll)
$\psi(q)$	Hand angle w.r.t x_0 (Hand pitch)
$\mathbf{p} \in \mathbb{R}^{6 \times 1}$	Vector of task space coordinates
α_{i-1}	Twist angle between axis z_{i-1} and z_i about x_{i-1}
a_{i-1}	Length of link i along axis x_{i-1}
d_i	Distance from x_{i-1} and x_i about z_i
\mathbf{T}_i^{i-1}	Transformation from frame i to frame $i-1$
$\mathbf{T}_i^0 \in \mathbb{R}^{4 \times 4}$	Transformation from frame i to base frame

r_{ab}	Element in the a^{th} row and b^{th} column of \mathbf{T}_i^0
$\ell_0, \ell_1, \ell_2, \ell_3$	Length of upper limb segments
$\Gamma(q)$	Forward kinematics function
\dot{q}, \dot{p}	Joint space velocities, and Cartesian velocity
$\mathbf{J}(q) \in \mathbb{R}^{6 \times 9}$	Jacobian matrix $\partial\Gamma(q)/\partial q$
$\theta_i^0, \theta_i^u, \theta_i^l$	Rest, maximum, and minimum angle of joint i
$v(\theta), \zeta(v)$	Conversion function of angles, and its inverse
$d\zeta \in \mathbb{R}^{9 \times 9}$	Weighing matrix of the transformed Jacobian
$\mathbf{J}_c^\dagger(v)$	Damped pseudoinverse of transformed Jacobian
$\mu \in \mathbb{R}^+$	Damping coefficient of pseudoinverse Jacobian
\hat{p}, \hat{v}	Desired Cartesian trajectory and joint angles
$k_0 \in \mathbb{R}^+$	Inverse kinematics control gain constant

Chapter 3

θ_m	Motor angular position
θ_s	Spring-side differential body angular position
θ_b	Brake-side differential body angular position
θ_u	User-side differential body angular position
Subscript m	Relates to motor body dynamics
Subscript s	Relates to spring-side differential body dynamics
Subscript b	Relates to brake-side differential body dynamics
Subscript u	Relates to user-side differential body dynamics
J	Angular inertia
b	Viscous friction
b_d	Viscous friction in differential from relative motion
k_s	Torsion spring constant
K_m	Motor torque constant
K_v	Motor back EMF constant
R_m	Motor winding resistance
V_m	Motor voltage
V_b	Brake voltage
τ_s, τ_b, τ_u	Differential body torques
τ_{app}	Torque applied by the user
τ_{cb}	Braking torque
τ_{cm}	Motor torque
τ_{ref}	Reference user torque
η_s, η_b, η_u	Differential body efficiency coefficients

Chapter 4

τ_{out}	Output torque
$\hat{\theta}_{bk}$	Backlash angle estimation
α_1	Maximum backlash angle of motor gearbox
α_2	Maximum backlash angle of differential gearbox
e_1	Proportional error
e_2	Time varying error
r_0	Transient profile acceleration rate
h_0	Transient profile precision coefficient
$u_p^i(t)$	Proposed input from feedback combiner i
γ	Nonlinear convergence rate
i	Observed subsystem index
$D(t)$	Term containing unknown disturbances
\bar{b}	Linear approximation of input rate
$\beta_{01,02,03}$	Linear observer gains for a second order plant
$u_q(t)$	Controller input for device q
h_1	Nonlinear feedback combiner precision coefficient
r_1	Nonlinear feedback combiner acceleration rate
c_1	Nonlinear feedback combiner fine tuning parameter
p_q^i	Proportional contribution gain from ESO i to input q
T_s	Sampling period

Chapter 5

$d_{1,2}$	Reference point distance measures
E_t	Tracking error
U_t	Control effort
P_o	Percent overshoot
t_r	Rise time
t_s	Settling time
U_{max}	Maximum input value
t_d	Disengagement time
N_Δ	Number of input direction changes
n	Order of the plant
n_{obs}	Number of extended state observers
n_{in}	Number of inputs

Chapter 1

Introduction

1.1 Introduction

THE RISE of collaborative robotic systems is leading to a paradigm shift in robotics. The robotic systems of today are moving away from confined industrial settings and making their way into more complex environments, such as homes or hospitals, to work alongside humans to complement our natural capabilities. This shift introduces a number of challenges with regard to the safety of human-robot interaction. Anytime there is a possibility for a human to come in close proximity to a robot, the number one condition for the choice of actuation method should depend solely on safety [1]. There is a growing need for high-performance actuators with respect to safety in a multitude of fields as human-robot interaction has become more prominent, deriving from efforts to increase productivity, efficiency, safety, and convenience to the general public. Potential fields for compliant actuators include haptics, manufacturing, shipping, automotive, retail, service, and in the medical field for uses such as rehabilitation or surgery.

The main issue around human-machine interaction is safety. Whenever a machine is interacting with, or in close proximity to, any human operator or bystander, a potential collision always exists. From an engineering standpoint, it is paramount that the devices used to interact with humans are reliable, stable, and safe. Traditional manipulators or devices used to convert electrical to mechanical energy are generally optimized around maximizing the payload of the device. To this end, the large accelerations and torques generated by these devices can be extremely harmful to humans. Without proper torque feedback, a collision with a human operator could go undetected and be disastrous. To mitigate this issue, traditional devices have been closed off to humans and confined to strict industrial workcells or academic settings. Lately, the cost of robotic manipulators and devices have dropped drastically, payload capabilities have been increasing, and the process

of programming has been simplified. This shift from bulky, complicated systems to devices fit to be used by commonplace individuals brings forth the opportunity of small and medium sized companies to take advantage of process automation. However, small and medium sized companies may not be able to accommodate for rigid workcells or assembly lines, and may have applications that benefit from a more intimate collaboration between the devices and the operators. An example of this type of application may include simple sorting tasks, pick and place tasks, packaging, shipping, and many more. In fact, collaborative robotic systems can be applied to medical applications such as robotic surgery, robotic prosthetics, and, the focal-point throughout this thesis, robot-assisted rehabilitation.

1.2 Robot-Assisted Rehabilitation

There is a growing need for novel therapeutic techniques focused on the recovery of upper-limb functionality in individuals experiencing musculoskeletal disorders (MSDs) [2]. MSDs typically result from excessive (i.e., chronic or acute) physical loading on tissues and joints. Physical impairment of the motor system, such as in the cases of stroke and cerebral palsy, can also be classified and rehabilitated in a similar manner as many MSDs [3]. These disorders are best characterized by changes in reflex excitability, muscle tone, and restricted range of motion, all leading to difficulties in performing voluntary movements [4,5]. Only approximately 50% of stroke patients regain full motor function of their upper limbs, suggesting the need for further advancement in upper-limb rehabilitation modalities [2].

The onset for upper-limb MSDs can stem from a variety of sources, ranging anywhere from short-term overexertion to long-term ergonomics. These disorders can result in lost time at work and can be painful and prevalent and, at times, these disorders may have a lifetime effect on the individual. The workforce in Canada is aging and the average age of working individuals is likely going to continue increasing for the foreseeable future, potentially contributing to a greater proportion of the disability burden due to workplace injury [6]. This additional burden on the health care system can lead to delays. A delay in receiving treatment after an injury can lead to severely adverse long-term effects on the recovery progress of the patient. Bruder, et al. emphasize in [7] that starting rehabilitative exercise early, when combined with a shorter immobilization period, is more effective than starting exercise after a longer immobilization period. Mitigation for upper-limb MSDs is delivered through physical rehabilitation, where, conventionally, the patient would go to a clinic or hospital to perform a series of repeated tasks under the supervision of a trained clinician. The entire rehabilitation process can take upwards of months of regular sessions

for severe cases of chronic upper-limb MSD's [8]. This is extremely taxing to both the patient and the clinician, and although there have been advances in ergonomic treatment and the health care system, there has been a paradoxical increase in MSD disability since 1950 [9].

An alternative approach to clinic-based rehabilitation that has emerged with rapid advancements in technology allows patients to receive regular treatments through physically interactive devices in the comfort of their own home. This is known as in-home rehabilitation, where patients are able to perform clinically-recommended exercises using specialized devices without having to be physically present at a health-care centre [10]. The devices designed for home-based rehabilitation are intended to improve the quality of physical rehabilitation, alleviate the labour-intensive aspects, and increase the efficiency of therapists [11].

Recent advances in robotics have introduced compelling new strategies to enhance recovery from upper-limb disability. Two main paradigms that have been gaining attention are assistive and rehabilitation robotics. One may argue that the ultimate goal of an assistive robot is to fully compensate for disability due to a given pathological condition and improve independence in social settings [12]. These technologies intend to allow individuals to accomplish activities of daily living that would otherwise be difficult or impossible to perform, using for example a manipulator arm [13–16]. With this approach, the patient controls the manipulator using a joystick or force feedback device and may interact with a variety of environments and other individuals via a teleoperation scheme.

Alternatively, one may discern rehabilitation robots as those helping therapists facilitate functional motor recovery of individuals with physical disabilities [17, 18]. Rehabilitation robots are typically designed for functional training, relearning, and reactivating residual motor function while preventing secondary complications such as muscle atrophy [19]. Although some symptoms of MSDs are permanent, studies have documented positive effects of robotic-assisted functional training in improving motor function of individuals living with cerebral palsy [20], and post-stroke movement impairments [11]. In the case of post-stroke therapy, robot-assisted therapy has demonstrated short-term reduction in motor impairment when compared to conventional rehabilitation therapy, such as muscle activation and speed of movement [21].

In the near future, it will be possible to combine robot-assistive therapeutic techniques with in-home rehabilitation regimes, allowing individuals to receive quality rehabilitation from within the comfort of their own homes. In-home rehabilitation can be pivotal for those yearning for a familiar environment, potentially decreasing recovery time [22]. In addition to this advantage, it is possible to design specialized devices with kinematic structures

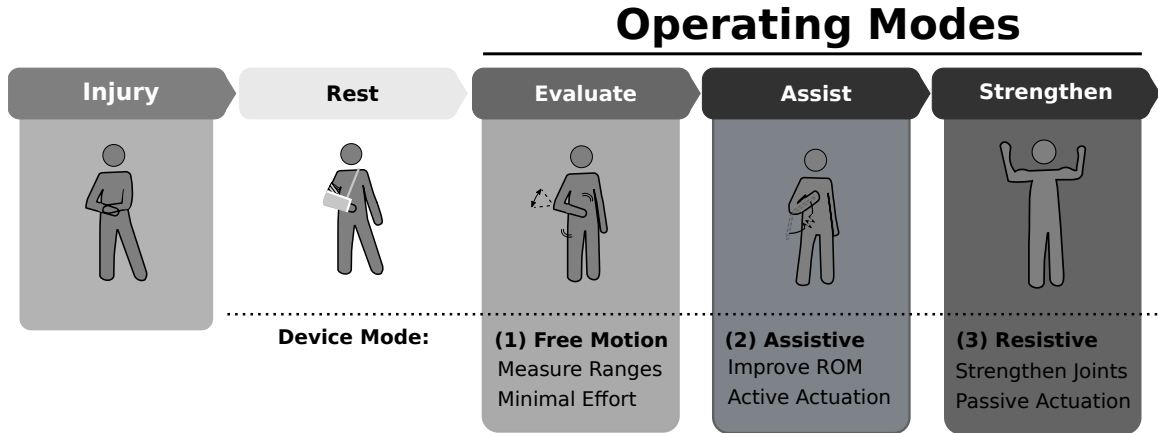


Figure 1.1: Rehabilitation timeline with device requirements to aid in the three final stages: evaluation, assistive, and resistive rehabilitation.

tailored to each individual and their specific rehabilitation requirements. By giving the patient access to these devices, the patient has the ability to receive more frequent training sessions, which would be especially useful in cases where high-dosage therapy is not feasible due to limited access of conventional therapy programs [23].

1.3 Devices Designed for Human-Machine Interaction

Devices designed for human-machine interaction with applications in robot-assistive rehabilitation must be versatile enough to take the form of a range of rehabilitation technologies currently in practice at clinics, from mimicking a simple elastic band to providing precise assistance in completing a complex movement. There have been a number of attempts to fully optimize the ability of a robotic device to provide the performance requirements mimicking conventional rehabilitation devices. Some of the characteristics expected from these devices include force bandwidth, efficiency, transparency, range of motion, size, weight, controllability, and patient comfort.

The rehabilitation devices must satisfy three major operating modes that are coupled to different stages of rehabilitation as shown in Fig. 1.1. The first mode entails that the device has to be able to become fully compliant at a moment's notice, allowing the patient to move the device freely with little effort [24], allowing the device to measure the range of motion (ROM) of the patient's joints. This is known as a device's transparency, where a high transparency is mapped to low effort of manipulation of the device. The second operating mode is patient assistance. This is the stage of rehabilitation in which a patient is unable to achieve a full range of motion about a single or multiple joints due to an impeding inability

to perform coordinated motion due to a MSD. The actuator must provide a reasonable amount of energy to assist the patient in accomplishing a particular task that they would otherwise not be able to complete on their own. This means that the actuator must introduce energy in the system (typically through electro-mechanical means) and be transferred to the patient. The third mode is the resistive mode: once the patient has regained their full range of motion, the injured area must then be strengthened back to as close to the pre-injured state as possible [25]. This requires the device to oppose the motion provided by the patient and dissipate the applied energy in a safe and controlled manner, as well as possess the ability to increase in difficulty as the patient's progress improves [2].

Upper-limb rehabilitation devices for home use can be generalized into two main categories, wearable orthopedic devices and fixed, end-effector based orthopedic devices. Wearable orthopedic devices are mounted externally by the individual receiving treatment, and, therefore, require additional safety measures. According to Veale and Xie [26], the important performance requirements are compliance, high specific power and force, speed, the ability to mimic natural motion, infinitely variable backdrivability, ease of control, and efficiency. They also emphasize that the key physical requirements for upper-limb orthopedic devices include low mass, slim form, low cost, modularity, environmental compatibility, quietness, and ranges of motion tailored to humans. Fixed devices are generally end-effector based, in which the patient manipulates the last link of the system along a desired trajectory complementing their rehabilitation regime. Fixed orthopedic devices have the same performance requirements as their wearable counterparts, however, they are much simpler to design due to the exclusion of some physical requirements such as low mass and slim form. By using desktop-based devices, the patient does not have to bear the additional burden of the weight of an entire mechanical system intended to assist them. In some cases, both branches are mixed to provide wearable devices that are rigidly fixed to a surface to provide support for the weight of the system [27, 28].

Actuators designed to be used in devices for the purpose of upper-limb rehabilitation should encompass the ability to perform the aforementioned rehabilitation exercises: active, passive, and compliant. In order to achieve these modes, the actuator should contain the following elements:

- ***Active Element:*** Active elements in the form of a pneumatic, hydraulic, or electro-mechanical system are necessary to perform assistive rehabilitation as they introduce mechanical energy;
- ***Force or Torque Sensing Capabilities:*** Devices interacting with humans must possess the ability to measure the interaction force with the user to ensure safety

and stability;

- ***Passive Element***: Although active elements can be used to resist motion in a device, passive elements are an optimal alternative as they are inherently stable and have a higher torque-to-mass ratio;
- ***Multimodality***: A switching mechanism allows switching between the differing modalities based on the desired phase of rehabilitation; and
- ***Encoders/Positional Measurement Devices***: Devices used for rehabilitation need to have the ability to track the range of motion a patient is able to achieve.

1.4 Active Actuation Sources

To add any amount of energy to a rehabilitation device, an active element must be present. The active element assists a patient in completing a controlled movement or by applying a range of forces to the user. Here, a variety of active actuation methods used in rehabilitation robotics are discussed and their advantages and shortcomings are compared.

Pneumatic Actuators

Pneumatic actuators use compressed gasses to create mechanical motion. The main advantage of pneumatic actuators include high power-to-weight ratio, mechanical compliance because of the inherent compliance of air, and force controllability [29]. Pneumatic actuators can provide a generous range of motion, with inertia and force-generating capacity matching well with a human arm [30, 31]. Pneumatic actuators are also backdrivable, have low mass, and low cost [26]. These conditions allow complex, multi degree-of-freedom (DOF) devices to be realized in a relatively small and lightweight package - making them suitable for wearable rehabilitation devices [32–34].

The largest drawbacks of pneumatic systems are the sources of compressed air and efficiency. The efficiency of a pneumatic system is only 20% than that of a hydraulic or electrical system [35]. Nonlinearities in both force and airflow dynamics in pneumatic systems contribute to difficulties in controlling these actuators [36] making them more challenging for use in applications requiring precision.

Hydraulic Actuators

Hydraulic actuators create mechanical motion from fluids. Hydraulic actuators can generate the largest amount of force compared to the other active actuation methods

presented in this section, with the drawback of having to include a power source in the design, limiting mobility [26]. There are some exceptions to this condition, for example the system in [37] can provide up to 89 Nm of torque in a package that weighs 4.5 kg. There are other devices that come in a relatively small package, however, they typically involve only a single joint movement. Hydraulic actuators for upper limb-rehabilitation typically target the flexion and extension of the elbow [38–40] with the main goal of providing biomimetic joint stiffnesses in single [41], and multi-joint [42] arm movements [40]. Other advantages of hydraulic actuators include smooth movements, no backlash, and good position tracking [43]. Some devices even take advantage of healthy joints to provide a means of energy to assist an injured joint through a process called bimanual or self-assist therapy [39]. Hydraulic actuation techniques have also been designed specifically for in-home upper-limb rehabilitation [44]. Aside from mobility issues, another drawback of hydraulic actuators includes power efficiency due to pressure differences in hydraulic valves. Efficiency on the order of approximately 14% is relatively standard for various hydraulic mechanisms [45].

Electric Actuators

Electric actuators are essentially electric motors (typically DC) coupled with peripherals such as gearboxes and/or angular displacement encoders. Electric actuators are classically used in robotic applications due to their controllability and relatively high torque to volume ratio. Compared to hydraulic or pneumatic actuators, electric actuators do not need an external pumping mechanism to create motion, reducing the overall size and response times required for the device. Electric actuators also have an efficiency that is much larger than that of hydraulic and pneumatic actuators, allowing some upper-limb rehabilitation devices to be portable [46] and, therefore, ideal for delivering home-based rehabilitation.

Some of the major pitfalls of electric actuators include low backdrivability due to high-reduction gearboxes. These gearboxes and transmission systems also attribute to the overall mass and noise of the actuator. A standalone motor-gearbox pair, like any active transmission systems, can be dangerous if directly coupled to a human for the purpose of rehabilitation. Electric actuators are the least biomimetic active sources discussed in this section and, therefore, require an additional compliant component to make them suitable for upper-limb rehabilitation.

1.5 Series Elastic Actuators

The addition of an elastic element to an actuator may not be intuitive, but with it comes a plethora of advantages over rigidly-coupled actuation topologies. Pratt and Williamson originally created the series elastic actuator in 1995 to improve shock tolerances, force control, stability, efficiency, and inertial characteristics of traditional electric motors [47]. Since then, elastic actuators have proved to be an excellent foundation for rehabilitative devices as they also allow for decoupled actuator inertia, reduced frictional effects, improved safety, and impact resistance as well as energy storage in the elastic element [48]. Additionally, elastic actuators under closed-loop force control can achieve good force bandwidth with a low output impedance [49]. Traditionally, collaborative robots implement force sensors at one or more joints, however, these sensors are expensive and rely on software to guarantee compliance [48, 50, 51]. By measuring the deflection of a spring element in an elastic actuator, precise end-effector force/torque control can be achieved [52–54]. This is desirable when considering actuators for in-home musculoskeletal rehabilitation devices as it creates a low-cost way of measuring patient performance without having to include a force sensor. One of the main intentions of SEAs with regards to rehabilitation is to mimic the elastic properties of the human musculoskeletal system. SEAs have become increasingly complex to better tailor applications in human-machine interaction. The tight constraints around maintaining operator safety in actuator design have produced a number of various actuation topologies that incorporate combinations of active and passive devices.

SEAs are the most common type of elastic actuators used in rehabilitation devices. Fig. 1.2 demonstrates various elastic actuator topologies used in the literature. A SEA is comprised of a single or multiple elastic elements between an actuator's active input and the output shaft. The actuators can be rotational or linear [55] and use any of the aforementioned active means of producing energy [56]. Elastic actuators have the advantage of providing a means of backdrivability and compliance to an otherwise rigid mechanical system. Purposely introducing a mode of compliance to the actuator decouples the inertia of a geared motor from the inertia of the output link, significantly improving the safety of the actuator to the user [1, 57]. Ideally, the spring chosen for an elastic actuator is linear with an infinite range of motion. If this were the case, spring stiffness would not play a role on the capabilities of SEAs. However, realistically, the chosen elasticity of the spring must depend on the resolution of the torque output and the magnitude of the maximum permissible torque [58] to ensure the spring is operating within its linear range. Therefore, careful consideration must be taken in the spring design for a SEA [59–61].

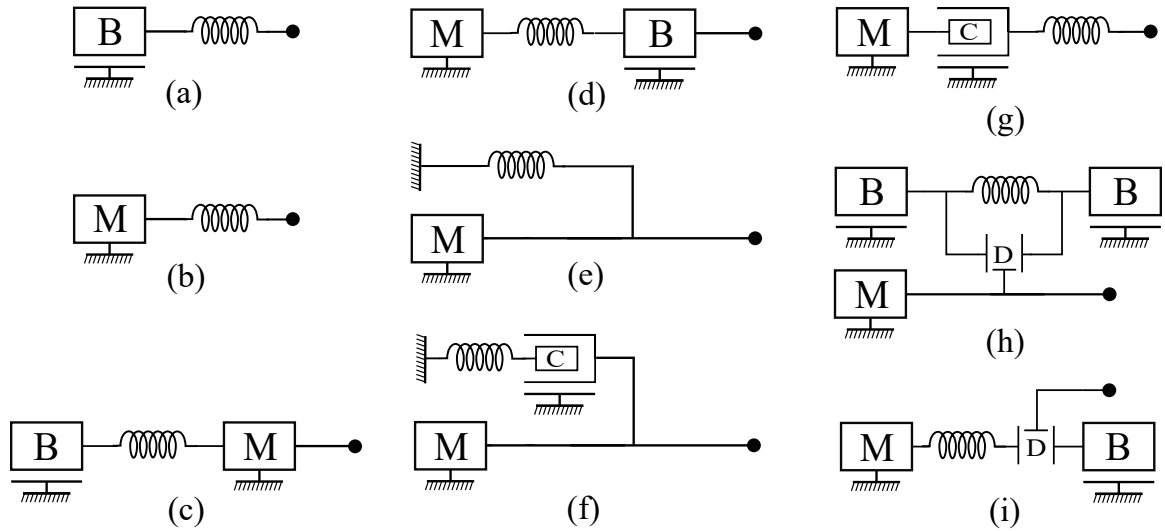


Figure 1.2: Schematic of actuator topologies: Label M represents a motor assembly, B represents a braking mechanism, C represents a clutching mechanism, and D represents a differential. Coils represent elastic elements and the black circles represent the output.

The most basic version of an elastic actuator is shown in Fig. 1.2(a), which is a controllable brake in series with an elastic element. This topology demonstrates the basis of all elastic actuators: by controlling the amount of energy stored in the elastic element, one can effectively control the forces at the output [62]. The actuator is strictly passive in this arrangement, where energy is either dissipated by the brake or stored in the spring. In order to achieve a greater range of forces, an active element is introduced in place of the passive element as outlined in Fig. 1.2(b). This arrangement has a motor in series with an elastic component and was originally designed to partially decouple the end-effector dynamics to that of the motor, improve shock tolerances, force control, stability, and efficiency, as compared to a rigidly connected motor. The main drawback is a reduced zero motion force bandwidth [47]. This arrangement is the most widely used in the literature to date with respect to robot-assisted rehabilitation [47, 49, 52, 54, 55, 58, 63–67].

Some devices make use of multiple elastic elements for the purpose of having a broader range of controllable torques. Others make use of a spring with a low stiffness for more precise force control at a lower force range but have the ability to manage high force impacts using a secondary spring with a larger stiffness [66]. These higher-stiffness secondary springs are generally used as torque limiters, a redundancy to improve safety of devices to be used in home-based rehabilitation [51].

1.5.1 Hybrid Elastic Actuators

In order to improve torque control, torque range, bandwidth, and safety, SEAs are currently migrating to topologies that combine multiple active and passive devices embedded in the same actuator [53, 59, 68–71]. Hybrid elastic actuators are defined as actuators containing two or more controllable elements. Since the introduction of elastic actuators, Conti, et al. [53] improved efficiency and safety by including a controllable brake in addition to the motor, similar to the topology in Fig. 1.2(c). Bridging passive elements such as controllable brakes with elastic actuators provides another means of not only controlling the output force, but also the stored force within the actuator, significantly reducing the total power required to complete a movement [53]. This gives elastic actuators the ability to switch between active and passive modes, making them suitable for rehabilitation of musculoskeletal disorders. In an alternative arrangement shown in Fig. 1.2(d) [59], the brake and motor positions are swapped to increase the amount of output impedance, thereby, increasing the ability of the actuator to resist a patient's motion.

In addition to this improvement, physically dissipative damping of brakes in hybrid actuators have been reported to be more stable in the event of significant noise and phase lag. This improvement allowed elastic actuators to be better implemented into medical devices where both passive and active actuation approaches are desirable.

1.5.2 Parallel Elastic Actuators

Parallel elastic actuators are a subset of elastic actuators where the spring is located in parallel with an active or passive device, sharing a common output. In some circumstances, motion in humans is better represented by the addition of a parallel spring, similar to the arrangement shown in Fig. 1.2(e) [72]. The parallel spring allows for a more fluid and efficient energy transfer on repetitive motion tasks, especially when a limb is frequently halted and re-accelerated [73]. The spring connected in parallel limits the range of motion and hinders the ability to accommodate some phases of motion in which rapid stopping is necessary [74]. A solution to this issue proposed in [74] introduces a clutch to the elastic actuator as shown in Fig. 1.2(f). Parallel elastic elements have advantages with regard to torque control and efficiency in human-robot interactive devices by storing otherwise wasted energy in the springs [72, 75, 76]. Efficiency savings on the order of 80% have been documented while reducing the maximum torque requirement of the active element in an actuator by up to 66% [74].

1.5.3 Multimodality

One of the conditions for the design of a device to be used in robot-assisted rehabilitation is the ability of a device to switch between modes. Further, the ideal device should be able to switch modalities on the fly, ensuring that the actuator can become compliant no matter the current state. A suitable device able to achieve switching can come in the form of a clutch. The addition of a clutch adds a mode of safety and is an important parameter with respect to actuators for upper-limb rehabilitation, as the clutch is the main mechanism that can select the type of exercise the patient experiences. The clutch can also decouple the patient from the active element, increasing overall safety. As well, the clutch allows the actuator to accommodate differing phases of motion by introducing nonlinearities to the system, improving biomimicry in multi-joint motion tasks [74].

1.5.4 Clutched Elastic Actuators

A clutch is traditionally defined as a device that has two states: one state allows the two bodies of the clutch to rotate independently, the other state locks the two bodies together such that the relative velocity is zero [77]. A clutch allows the actuator to engage or disengage an elastic element. Rouse, et al. [68] adapted this concept towards SEAs (Fig. 1.2(g)) with the main advantage of tuning the actuator's compliance using a series clutch to improve biomimicry and efficiency [68]. In fact, it has been shown that the force resolution of an actuator increases exponentially with the number of clutches and springs involved [78]. A recent approach, depicted in Fig. 1.2(h), makes use of a bi-directional clutched parallel elastic actuator that uses a differential spring-brake mechanism to decrease energy consumption and to control the energy stored in the elastic element [76].

Depending on the rehabilitation requirements for each individual, there is a need to switch between motor functions for dynamic robotic systems to improve their behavioral diversity [79]. Clutching mechanisms direct the energy flow in an actuator. In some cases, an actuator's clutch is used to couple parallel springs to the drive train. In the context of safety, an actuator should release any stored energy if a collision is detected. This is where a classical SEA with a low bandwidth falls short as it may not be able to dissipate the energy stored in the elastic element quickly. To mitigate this behavior, elastic actuators can make use of a standard clutch to control the energy stored in the elastic element and provide a means of quickly releasing the stored energy [78].

A recent study was done that relates the functionality of an actuator with the number of springs and clutches the actuator contains, determining that the torque bandwidth of an actuator increased exponentially with the number of clutches and springs involved

[78]. This review also touched on the advantages of using three-body differentials in elastic actuators, but further development is required to introduce them into robotic applications. Although differential clutches have been used in hybrid actuators [80], integrating differentials to elastic actuators has been a work in progress.

1.6 Proposed Series Elastic Actuator

In this thesis, the Differentially-Clutched Series Elastic Actuator (DC-SEA) is introduced. The DC-SEA makes use of a differential clutch paired with an elastic-coupled DC motor and a magnetic particle brake as shown in Fig. 1.2(i). Although differential clutches have been used in hybrid actuators [80], integrating differentials to elastic actuators has not been done. The main goal of the motor and brake working in tandem is to have the ability to couple the user shaft to a small-packaged motor with a high gear ratio, inevitably creating a slower response time, but maintaining the ability to completely decouple the user from the motor/spring pair in the event of an emergency. This provides two independently controlled mechanisms of safely decreasing the amount of energy either by using the motor to decompress the spring or by disengaging the brake, allowing for different operating modes as shown in Fig. 1.2.

In the DC-SEA topology, when a relatively high-gear ratio motor is powered off, this creates a pseudo-ground on one side of the elastic element creating a mode equivalent to that shown in Fig. 1.2(a). When the brake is fully engaged, the differential acts as a clutch between the output shaft and the motor-spring mechanism taking the form of Fig. 1.2(b). As opposed to traditional clutches such as those used in automobiles, the differential clutch can be used to continuously control the amount of force transferred between the output and the motor-spring assembly through the use of the magnetic particle brake, which can be considered to operate as a variable damper. The latter is able to fully recreate the functions of Fig. 1.2(g) and partially encompasses the capabilities of Fig. 1.2(c), (d), (f), and (h).

1.7 Series Elastic Actuator Torque Control

Certainly, the inherent advantages introduced by SEAs do not come without a cost. The nonlinear stiffness and potential backlash of the elastic element pose a challenging control issue in which classical force control methods may not be sufficient. The controller must satisfy its intended goal and control the output torque, while respecting the most important factor of human-machine interaction: the operator's safety. As the number of devices increases in an actuator, classical controllers such as a proportional-integral-derivative

(PID) controllers containing a simple error-based approach may be insufficient for complex output profiles. The ability of an elastic actuator to leverage inferred torque control through deflection measurements brings forth a multitude of advantages over conventional actuators. With this torque inference, external disturbances can be quantified and mitigated through proper robust torque control, as compared to position or velocity control where external disturbances result in an error value with little information about the disturbance. In the context of human-machine interaction, the ability of an actuator to collaborate with a human operator and recognize when a disturbance is caused by interaction with a human is significant [24].

More complex topologies introduce new challenges on their own. They usually come in the form of motors or brakes connected through gearboxes, belts, harmonic drives, or cables. Unfortunately, this creates uncertainty in the form of backlash, that is, the tolerance in the physical meshing of gear teeth in a transmission system. Since SEAs use positional measurements to infer the torque experienced at the output, accurate torque control heavily relies on the controller's ability to compensate for concurrent nonlinear effects due to backlash and nonlinear compliance of the elastic element. Current backlash compensation techniques include dead zone functions [81, 82], exact models [83], describing functions, and hysteresis models [84].

1.8 Objectives and Outline

The issue described in the previous section requires a controller that is robust enough to differentiate between perturbations caused by imperfect models and external inputs to the system [85]. Active disturbance rejection controllers (ADRCs) mitigate this issue by encapsulating these perturbations into a common disturbance term, which can be considered as a new state in the controller model. Active disturbance rejection control is an error-based method used to control the behavior of a generic plant. ADRC has the advantage of being able to compensate for disturbances to the plant compared to PID controllers, improving robustness while maintaining relative simplicity [86]. Generally, a PID controller is tuned for a specific operation, where the disturbance introduced to a plant is constant or negligible. This may be sufficient for many cases, however, if the process is sensitive to control effort or significant and/or random disturbances are experienced, a more robust control method must be used.

Typically, ADRCs designed for SEAs are single-input single-output systems (SISO) [54, 87]. In hybrid SEA topologies, it is common to have multiple control inputs that relate directly to the output torque [87], making SEAs multi-input multi-output

(MIMO) systems. Thus, besides nonlinearities and unmodelled dynamics, SEA controllers must also be able to handle multiple control inputs as opposed to classical single-input controllers reported in the literature [88]. To this end, convergence in multi-input plants with disturbance observers with mismatched disturbances is demonstrated in [89] and, similarly, for unmodelled time-varying load-side dynamics in [90]. Stability proof of ADR controllers for multi-input saturating plants is shown in [91], further demonstrating the advantages of disturbance rejection controllers for the DC-SEA.

The main objectives of the research conducted in this thesis is to develop a novel type of elastic actuator and control strategies suitable for human-machine interaction. Emphasis is placed on designing actuators for home-based, robot-assisted rehabilitation in patients experiencing upper-limb musculoskeletal disorders. However, the research conducted over the course of this thesis can be used in many applications regarding human-machine interaction. Safety of this interaction is mostly concerned with the mode of actuation and, therefore, a new actuation approach was developed to be tailored to these applications. The chapters in this thesis pertaining to the main objectives of this thesis are as follows:

- **Chapter 2** aims to develop a framework for determining the range of motion capabilities for individuals experiencing musculoskeletal disorders modelled through joint constraints. This formulation can be used as a tool in designing or arranging the optimal kinematic structure in robotic rehabilitation devices tailored to the unique needs and joint ranges of the patient.
- **Chapter 3** proposes a novel SEA designed specifically for physical human-machine interaction. The proposed actuator focuses on the three types of actuation modalities most commonly used in rehabilitation and aims to guarantee operator safety through its design features.
- **Chapter 4** proposes a unified torque controller for multi-input SEAs. The controller is based on a modified active disturbance rejection control architecture that has been combined with a backlash compensation model for mitigating nonlinearities in spring deflection measurements.
- **Chapter 5** applies a multiobjective, evolutionary algorithm optimization strategy to determine optimal controller gains for the multi-input plant.

Finally, the conclusions and recommendations towards future developments are highlighted in Chapter 6.

Chapter 2

9-DOF Human Arm Model for Workspace Evaluation with Constrained Inverse Kinematics

2.1 Introduction

THE first step in implementing robotic assistance and rehabilitation is by assessing the individual's pathological conditions. In this stage, the extent of a hindrance from an injury or disability can be quantified and examined. A variety of assessments exist to quantify joint movement ranges. The most common techniques quantify the velocity-dependent response of muscles to passive stretching. One method that has been extensively used clinically involves manually moving a limb through its range of motion and grading the resistance encountered on a five-point ordinal scale [92]. In more sophisticated methods, servo-controlled motors apply controlled displacements or torques to joints while limb angle, torque, and electromyographic responses are recorded [93]. Other measures such as range of motion of each joint achieved with and without assistance, according to the individual's tolerances and level of discomfort, may be included in these assessments.

Based on the identified range of each joint, a kinematic model of the upper limb can be used to identify workspaces where the individual with a disability is able to perform tasks and those regions in which robotic assistance is required. Robotic intervention strategies can then be established based on an individual's specific capabilities. Knowing these workspaces opens up two possibilities. The first possibility concerns assistive and cooperative telerobotics. When an individual interacts with a helper using haptic devices, the teleoperation scheme is often implemented where position control and displacement of

one robot is correlated to displacement of the other robot. Since the individual workspace is different from that of the helper, motion may be scaled accordingly by normalizing the devices' positions to their respective workspaces [94]. Thus, tasks outside the patient's reach envelope can be scaled to match their feasible range of motion, allowing both individuals to interact without posing any risk or discomfort to the individual with the disability. The second possibility relates to rehabilitation. It is assumed that the individual is able to move their arm in a given workspace that can be determined through the kinematic model. Robotic assistance is only provided when they are required to move their arm in a region they are not able to reach without assistance.

In this chapter, the strategies described above are developed and organized around two main contributions: 1) A 9 degrees-of-freedom (DOF) kinematic model of the upper limb is derived to evaluate the individual's range of motion. This is achieved through inverse differential kinematics taking into account the physical limits of each joint. 2) A method to evaluate different workspaces according to unique internal joint constraints, as well as external constraints on the range of motion of the user's hand, while limiting the individual's motion to their feasible range. This is achieved through nonlinear mapping of each joint angle such that the differential inverse kinematics saturates the joint velocities as they approach their respective limits.

There are a number of kinematic models for the upper arm with 7-DOF or greater [95–100], however, the inverse kinematic solution for the redundant models are usually achieved by reducing the number of evaluated joints to six or less. The proposed inverse kinematic solution finds acceptable values of all nine joints at once within a set of predetermined constraints. To the best of the author's knowledge, this is the first 9-DOF model of the upper limb complex incorporating the joint limits in the formulation of its inverse kinematics. It can be used as an invaluable tool to aid in the design of rehabilitation devices. This chapter is organized as follows: Section 2.2 defines the 9-DOF forward kinematic model of the human upper-limb segment. Section 2.3 introduces a novel constrained differential inverse kinematic method for evaluation of the task-space redundant model. This method is experimentally validated in Section 2.4.

2.2 Forward Kinematics of the Upper Limb

As a first approximation, it is a reasonable assumption to model the mechanical structure of the human arm complex to be composed of 9-DOF. As shown in Fig. 2.1(a), it is appropriate to schematize the human arm as a quadruple-pendulum whose segments are the clavicle, humerus, forearm, and the hand, connected through the appropriate number of

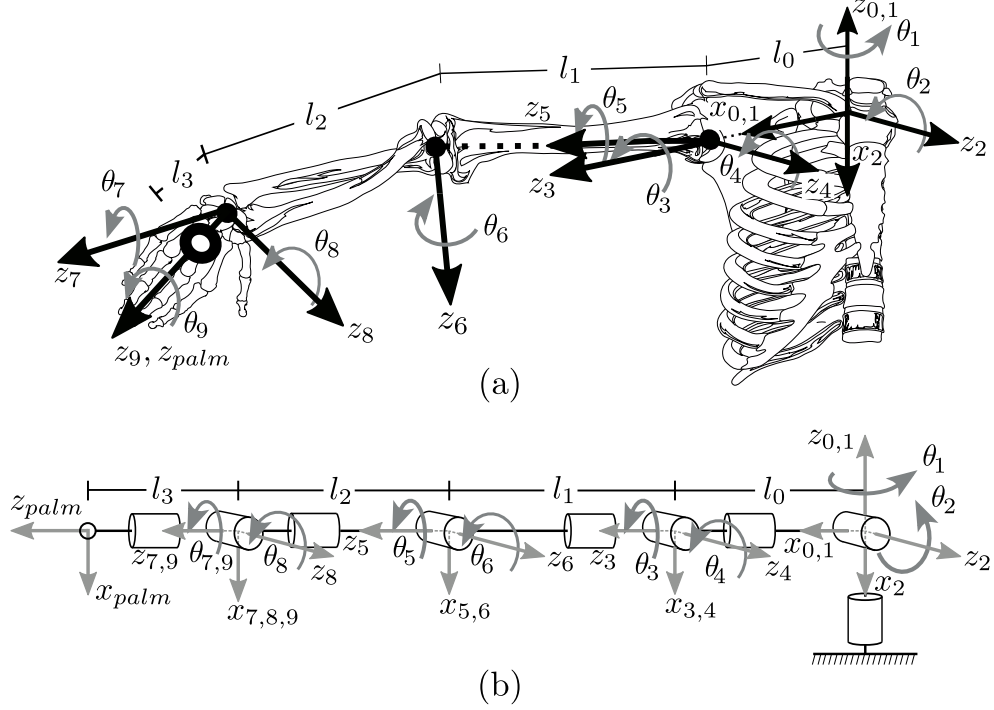


Figure 2.1: (a) The equivalent 9-DOF kinematic model overlaid on the upper limb complex. (b) The equivalent zero displacement model of the upper limb complex with the modified Denavit-Hartenberg parameters from Table 1.

revolute joints [101,102]. From a kinematic standpoint, it is convenient to single out 2-DOF at the sternoclavicular joint to account for scapular retraction/protraction as well as scapular elevation/depression. In a rehabilitative sense, the scapula is essential to include in the kinematic model for cases in which the shoulder is injured [103]. A 3-DOF spherical joint at the shoulder allows for glenohumeral medial/lateral rotation, glenohumeral adduction and abduction, and humeral flexion/extension, 1-DOF at the elbow allowing for extension and flexion of the forearm, and a 3-DOF spherical joint at the wrist, allowing for wrist supination/pronation, flexion/extension, and radial/ulnar deviation. In Fig. 2.1, l_0 is the acromioclavicular interval, l_1 and l_2 are the lengths of the humerus and forearm, respectively, and l_3 is the distance from the distal palmar crease to the wrist crease.

The equivalent kinematic model consisting of nine revolute links is presented in Fig. 2.1(a). A base frame $x_0 y_0 z_0$ is fixed at the sternoclavicular joint. Local body frames $x_i y_i z_i$, $i = 1, 2, \dots, 9$, are fixed at the origin of link $i+1$. Frame $i = 10 = palm$ is at the centre of the hand and corresponds to the position of the end-effector. Following the modified Denavit-Hartenberg convention [104], axis i denotes the axis of the joint connecting link $i-1$ to link i . The angle of rotation from x_{i-1} to x_i about the axis z_i is θ_i . Let a_{i-1} be the length of link $i-1$, i.e., the distance between z_{i-1} and z_i axis along x_{i-1} , and d_i the joint distance,

i.e., the distance between x_{i-1} and x_i along z_i . Let also α_i be the twist angle between axis z_{i-1} and z_i about x_{i-1} . The transformation matrix \mathbf{T}_i^{i-1} from frame i to frame $i-1$ is

$$\mathbf{T}_i^{i-1}(q) = \begin{bmatrix} C\theta_i & -S\theta_i & 0 & a_{i-1} \\ S\theta_i C\alpha_{i-1} & C\theta_i C\alpha_{i-1} & -S\alpha_{i-1} & -S\alpha_{i-1}d_i \\ S\theta_i S\alpha_{i-1} & C\theta_i S\alpha_{i-1} & C\alpha_{i-1} & C\alpha_{i-1}d_i \\ 0 & 0 & 0 & 1 \end{bmatrix} \quad (2.1)$$

where $\mathbf{q} = [\theta_1 \ \theta_2 \ \dots \ \theta_9]^T \in \mathbb{R}^{9 \times 1}$ is the vector of joint variables and S and C represent $\sin(\cdot)$ and $\cos(\cdot)$, respectively. In this section, the subscript of a vector or matrix denotes the frame in which its components are expressed.

The Denavit-Hartenberg parameters for the 9-link mechanism to be used in Equation (2.1) are summarized in Table 2.1. It is worth noting that the shoulder and the wrist have spherical joints since all of their respective revolute axes intersect at a single point and thus a_3, a_4, a_5 , and a_7, a_8, a_9 equal zero. The centre of rotation of the humerus is shifted from the rotation axis of the scapula joint by ℓ_0 and thus $d_3 = \ell_0$. Likewise, the end-effector is shifted from the centre of rotation of the wrist by ℓ_3 and hence $d_{10} = d_{palm} = \ell_3$. For the 9-DOF mechanism, it follows that the coordinates of a point $\mathbf{c}^j = [x_j \ y_j \ z_j \ 1]^T$ that is expressed in frame j , can be converted to the base frame as:

$$\mathbf{c}^0 = \prod_{i=1}^j [\mathbf{T}_i^{i-1}(q_i)] \mathbf{c}^j = \mathbf{T}_j^0(q) \mathbf{c}^j \quad (2.2)$$

The x, y, z position of the end-effector in the base frame is

$$[x \ y \ z \ 1]^T = \mathbf{T}_{10}^0(q) [0 \ 0 \ 0 \ 1]^T \quad (2.3)$$

with $\mathbf{T}_{10}^0 \in \mathbb{R}^{4 \times 4}$ being defined in Equation (2.2). The Cartesian position of the hand as a function of the joint angles is now known. In order to fully specify the pose of the hand, one must also determine its orientation in the base frame.

2.2.1 Task Space Vector Formulation

Without loss of generality, let $r_{a,b}$ denote the element in the a^{th} row and b^{th} column of the transformation matrix \mathbf{T}_0^{10} defined in Equation (2.2). The Cartesian position of the palm centre is given by $x(q), y(q)$, and $z(q)$ referenced from the base frame x_0, y_0, z_0 , where the x_0 axis is parallel to the line passing through the centre of rotation of both shoulder complexes. The y_0 axis runs perpendicular to the face of the sternum (i.e. in front and

Table 2.1: Modified Denavit-Hartenberg parameters for the 9-DOF upper limb model.

i	Motion	a_{i-1}	α_{i-1}	d_i	θ_i
1	Scapular retraction/protraction	0	0	0	θ_1
2	Scapular elevation/depression	0	$-\pi/2$	0	$\theta_2 + \frac{\pi}{2}$
3	Shoulder flexion/extension	0	$\pi/2$	l_0	θ_3
4	Shoulder adduction/abduction	0	$-\pi/2$	0	θ_4
5	Shoulder medial/lateral rot.	0	$\pi/2$	l_1	θ_5
6	Elbow flexion/extension	0	$-\pi/2$	0	θ_6
7	Wrist ulnar/radial deviation	0	$\pi/2$	l_2	θ_7
8	Wrist flexion/extension	0	$-\pi/2$	0	θ_8
9	Wrist pronation/supination	0	$\pi/2$	0	θ_9
10	Palm centre transform	0	0	l_3	0

behind the individual), and the z_0 axis runs above and below the individual, parallel to a gravity vector. The individual's orientation is defined using Euler angles, specifically by the pitch $\varphi(q)$ of the hand (angle with respect to x_0), its roll $\psi(q)$ (angle with respect to y_0), and its yaw $\gamma(q)$ (angle with respect to z_0), which are given as:

$$\varphi(q) = \tan^{-1} \left(\frac{r_{3,2}}{r_{3,3}} \right) \quad (2.4)$$

$$\psi(q) = \tan^{-1} \left(-\frac{r_{3,1}}{\sqrt{(r_{3,2})^2 + (r_{3,3})^2}} \right) \quad (2.5)$$

$$\gamma(q) = \tan^{-1} \left(\frac{r_{2,1}}{r_{1,1}} \right) \quad (2.6)$$

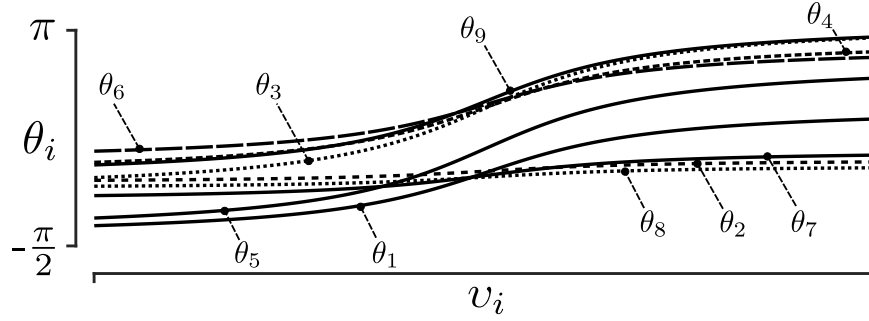
$$x(q) = r_{1,4}, y(q) = r_{2,4}, z(q) = r_{3,4} \quad (2.7)$$

The task space vector that specifies the hand's position (x, y, z) and orientation (φ, ψ, γ) with respect to the base frame $x_0y_0z_0$ denoted $\mathbf{p} \in \mathbb{R}^{6 \times 1}$ can now be defined as $\mathbf{p} = [x \ y \ z \ \varphi \ \psi \ \gamma]^T$.

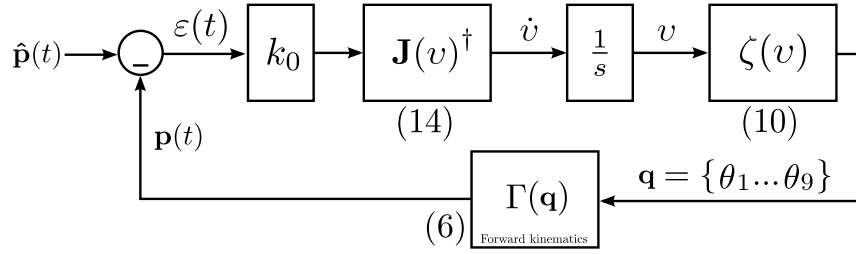
2.2.2 Forward Kinematics

The direct kinematics equation specifies the relationship between the joint vector \mathbf{q} and the Cartesian vector \mathbf{p} as

$$\mathbf{p} = \Gamma(\mathbf{q}) \quad (2.8)$$



(a) Saturation function of joint angles



(b) Overview of the constrained differential inverse kinematics

Figure 2.2: Overview of the inverse kinematics formulation with joint limits. In (a) each curve shows the transformed joint angle θ_i as a function of the new variable v_i for the joint limits given in Table 2.1. In (b) the constrained differential kinematics workflow is shown.

Analogously, the relationship between the joint velocities $\dot{\mathbf{q}}$ and Cartesian velocities $\dot{\mathbf{p}}$ is obtained as

$$\dot{\mathbf{p}} = \mathbf{J}(\mathbf{q})\dot{\mathbf{q}} \quad (2.9)$$

where $\mathbf{J}(\mathbf{q}) \in \mathbb{R}^{6 \times 9}$ is the Jacobian matrix $\partial\Gamma(\mathbf{q})/\partial\mathbf{q}$.

It is now clear that the 9-DOF arm is kinematically redundant since the six variables specified in Cartesian space depend each on nine independent joint space variables [105].

2.3 Constrained Differential Inverse Kinematics

The objective of the constrained differential inverse kinematics is to ensure that the solutions found for each of the nine joint angles for a given end-effector position and orientation fall within the physical limitations of each joint. Instead of discarding potential solutions that do not fall within the limitations of each joint, the purpose of the constrained differential inverse kinematics is to ensure that every solution will meet these requirements. This is accomplished by saturating the joint angle velocities nearing the limits of each joint, similar to natural human motion.

To compute the posture of the upper limb when the hand follows a specific trajectory, the inverse kinematics must guarantee that each joint stays within its physical limits. This can be achieved through a transformation that will bring the joint angles into a new set of variables using a function that saturates a joint angle when it approaches a given limit.

Let θ_i^u and θ_i^l be the upper and lower limits of joint i (see Table 2.3 for numerical values of an adult individual without disability). The function that transforms the joint variables to the new variables $v_i = f(q)$ must be continuously increasing in the open interval (θ_i^l, θ_i^u) . A suitable candidate for this function is the tangent function $\tan(\theta_i)$, where θ_i is linearly mapped from (θ_i^l, θ_i^u) to $(-\pi/2, \pi/2)$, that is:

$$v_i(\theta_i) = \tan\left(\frac{\pi}{2} \frac{2\theta_i - \theta_i^u - \theta_i^l}{\theta_i^u - \theta_i^l}\right) \quad (2.10)$$

and whose inverse

$$\zeta(v_i) = \theta_i(v_i) = \frac{\theta_i^u - \theta_i^l}{\pi} \tan^{-1}(v_i) + \frac{\theta_i^u + \theta_i^l}{2} \quad (2.11)$$

is bounded to (θ_i^l, θ_i^u) as shown in Fig. 2.2(a) for the joint limits given in Table 2.1. This will ensure that the joint limits will not exceed their specified limits in the formulation of the inverse kinematics. Now, one can substitute Equation (2.11) into the forward kinematics given in Equation (2.9) and recompute the Jacobian with respect to the new variable $v = [v_1 \ v_2 \ \dots \ v_9]^T$. The new Jacobian $\mathbf{J}_c(v)$ is calculated as $\partial\Gamma(v)/\partial v$, which is equivalent to setting

$$\mathbf{J}_c(v) = \begin{bmatrix} \frac{\partial x(v)}{\partial v_1} & \frac{\partial x(v)}{\partial v_2} & \dots & \frac{\partial x(v)}{\partial v_9} \\ \frac{\partial y(v)}{\partial v_1} & \frac{\partial y(v)}{\partial v_2} & \dots & \frac{\partial y(v)}{\partial v_9} \\ \frac{\partial z(v)}{\partial v_1} & \frac{\partial z(v)}{\partial v_2} & \dots & \frac{\partial z(v)}{\partial v_9} \\ \frac{\partial \varphi(v)}{\partial v_1} & \frac{\partial \varphi(v)}{\partial v_2} & \dots & \frac{\partial \varphi(v)}{\partial v_9} \\ \frac{\partial \psi(v)}{\partial v_1} & \frac{\partial \psi(v)}{\partial v_2} & \dots & \frac{\partial \psi(v)}{\partial v_9} \\ \frac{\partial \gamma(v)}{\partial v_1} & \frac{\partial \gamma(v)}{\partial v_2} & \dots & \frac{\partial \gamma(v)}{\partial v_9} \end{bmatrix} = \mathbf{J}(q)d\zeta \quad (2.12)$$

where the term $d\zeta \in \mathbb{R}^{9 \times 9}$ is

$$d\zeta = \begin{bmatrix} \frac{\partial \zeta(v)}{\partial v_1} & 0 & \dots & 0 \\ 0 & \frac{\partial \zeta(v)}{\partial v_2} & \dots & \vdots \\ \vdots & 0 & \ddots & 0 \\ 0 & \dots & 0 & \frac{\partial \zeta(v)}{\partial v_9} \end{bmatrix} \quad (2.13)$$

The inverse solution of Equation (2.9) can now be written considering the change of

variables and the saturation of the joint angles as

$$\dot{\mathbf{v}} = \mathbf{J}_c^\dagger(\mathbf{v})\dot{\mathbf{p}}, \quad (2.14)$$

where $\mathbf{J}_c^\dagger(\mathbf{v})$ is the damped pseudoinverse of the transformed Jacobian matrix given by

$$\mathbf{J}_c^\dagger(\mathbf{v}) = \mathbf{J}_c(\mathbf{v})^T [\mathbf{J}_c(\mathbf{v})\mathbf{J}_c(\mathbf{v})^T + \mu\mathbf{I}]^{-1} \quad (2.15)$$

if the Jacobian is full rank, providing a least-squares solution with minimum norm to Equation (2.9). In Equation (2.15), $\mathbf{I} \in \mathbb{R}^{6 \times 6}$ is an identity matrix and $\mu \in \mathbb{R}^+ \ll 1$ is the damping constant scalar used to avoid possible discontinuity of the pseudoinverse at a singular configuration. In detail, this solution satisfies the condition $\min \|\dot{\mathbf{v}}\|$. Furthermore, provided that $\zeta(\mathbf{v})$ is monotonically increasing in the open interval (θ_i^l, θ_i^u) , and given that $\dot{\mathbf{v}} = \dot{f}(q)\dot{q}$, the pseudoinverse Jacobian also satisfies $\min \|\dot{q}\|$.

Let $\hat{\mathbf{v}}(t)$ be a solution to $\hat{\mathbf{p}}(t) = \Gamma(\mathbf{v})$ relative to a desired Cartesian trajectory $\hat{\mathbf{p}}(t) \in \mathbb{R}^{6 \times 1}$. A purely proportional control law in the form of

$$\dot{\mathbf{v}} = k_0 \mathbf{J}_c^\dagger(\mathbf{v}) [\hat{\mathbf{p}}(t) - \Gamma(\mathbf{q})] \quad (2.16)$$

can be shown to ensure that $\boldsymbol{\varepsilon} = \hat{\mathbf{p}}(t) - \Gamma(\mathbf{q}) \rightarrow 0$ and then $\mathbf{v} \rightarrow \hat{\mathbf{v}}$, provided that $k_0 > 0$. It is important to underscore that $\Gamma(\mathbf{q})$ is the forward kinematics computed with the physical joint angles θ_i calculated through the inverse transformation $\mathbf{q} = \zeta(\mathbf{v})$ using Equation (2.11). Obviously, the maximum tracking error $\boldsymbol{\varepsilon}$ depends on $\hat{\mathbf{p}}$, and inversely on $k_0 \in \mathbb{R}^+$, however, the steady-state error ($\boldsymbol{\varepsilon}$ when $\hat{\mathbf{p}} = 0$ and $t \rightarrow \infty$) is zero [106]. Fig. 2.2(b) summarizes the closed-loop differential kinematics workflow incorporating the joint limits.

Here, four remarks shall be considered before moving forward:

1. Close scrutiny of Equation (2.15) reveals that $\mathbf{J}_c(\mathbf{v})^\dagger = \mathbf{J}(\mathbf{q})^\dagger d\zeta^{-1}$ (for $\mu = 0$), meaning that the transformation of variable acts as a gain in the velocity of joints and stiffens those that are close to their limits.
2. The formulation in Equation (2.16) implies that the arm tends to move from an initial point $\hat{\mathbf{p}}(t = t_0)$ to a new point $\hat{\mathbf{p}}(t = t_1)$ following a trajectory that minimizes the joint velocities. In other words, the hypothesis is that trajectories are chosen to minimize metabolic energy costs, as proved in [107, 108].
3. Because of (2), the trajectory between two points is likely to be a straight line. To accurately represent human behaviour, point-to-point motion must be discretized into several motion primitives.

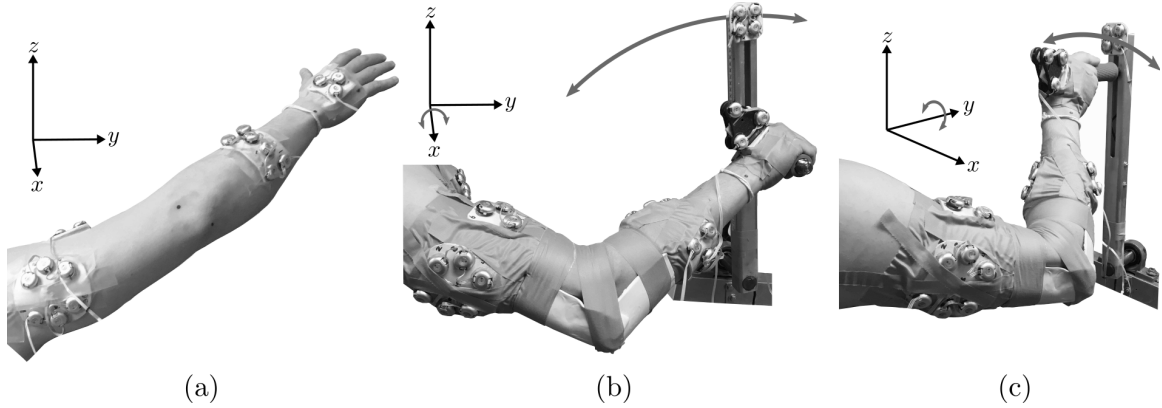


Figure 2.3: Experimental scenarios: (a) Scenario 1: The subject’s palm is unconstrained and able to move freely in 3-dimensional space. (b) Scenario 2: The subject is grasping the device that is constrained on a plane normal to the subject’s stance. The device constrains the hands translational movement to the $y - z$ plane. The roll rotation $\psi(q)$ of the hand is also constrained. (c) Scenario 3: The subject is grasping the device constrained on a plane parallel to the subject’s stance. The device is restricting translational motion to the $x - z$ plane as well as the subjects rotational roll.

4. The boundaries of the workspace calculated through the model do not depend on (2) nor (3).

2.4 Experimental Validation

The constrained workspace evaluation is a method used to determine the reachable workspace of an individual subject to one or more joint limitations. This reduced subset of the reachable workspace can be compared to the workspace of the individual under ideal unconstrained conditions. This evaluation can provide information on locations in Cartesian space under which, for example, a patient may feel discomfort. Three experimental scenarios were conducted to validate the performance of the model. The experimental scenarios are demonstrated in Fig. 2.3. Scenario 1, shown in Fig. 2.3(a), evaluated the total reachable workspace of a subject with and without an emulated internal joint constraint. Scenarios 2 and 3, shown in Fig. 2.3(b) and Fig. 2.3(c), respectively, demonstrate the total reachable workspace of the subject under additional external constraints of the subject’s palm to a predefined trajectory.

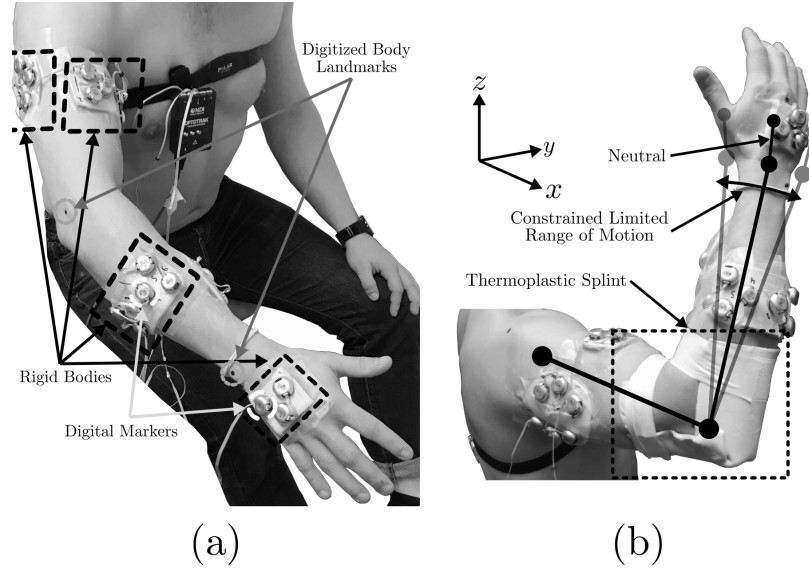


Figure 2.4: (a) Picture of the rigid body setup on an unconstrained subject. This image demonstrates the clusters of rigid bodies used to determine the position and orientation of the limbs of the upper arm complex. Black marks on the body represent points of reference that are calibrated with respect to two or more digital rigid body clusters. (b) Thermoplastic splint limiting the range of motion of the elbow joint approximated by the grey lines.

2.4.1 Data Collection

The model was validated through experimental procedure using an array of Northern Digital Instruments Optotrak 3D Investigator cameras combined with digital markers to provide precise measurements of various points on the upper limb complex as shown in Fig. 2.4. Three of the cameras were placed along three walls of a room to ensure the digital marker rigid bodies remained within line of sight of at least one of the cameras at all times. The position and orientation of each camera was calibrated to create a global reference frame that is consistent throughout this work and denoted by a coordinate frame in most figures presented hereafter. Once calibration of the cameras was complete, the subject was instrumented with the active digital marker rigid bodies, which are stiff plates used to maintain position and orientation of a small cluster of digital markers. This cluster is then used to calculate the position and orientation of the rigid body. Once the rigid bodies were secured to the subject, various anatomical landmarks were chosen to evaluate the joint angles throughout the experiment. Each landmark which posed a risk of bodily occlusion was instrumented with two or more rigid bodies and, therefore, added redundancy for positional measurements. Table 2.2 lists the anatomical landmarks and the rigid bodies associated with each landmark. The experiments conducted in this work used at least two rigid bodies on the thorax, two rigid bodies mounted along the humerus, namely the

Table 2.2: Rigid Body Anatomical Landmarks

Thorax Bodies	Hand Bodies	Upper Arm Bodies	Forearm Bodies
right acromioclavicular	ulnar styloid process	right acromioclavicular	medial epicondyle
left acromioclavicular	radial styloid process	medial epicondyle	lateral epicondyle
right iliac crest	tip of middle finger	lateral epicondyle	ulnar styloid process
left iliac crest	dorsal base, 2 nd metacarpal	olecranon process	radial styloid process
C7 vertebrae	dorsal base, 5 th metacarpal		olecranon process
suprasternal notch	palm centre		
xiphoid process	dorsal base, 3 rd metacarpal		
proximal sacrum			
lateral spine of scapula			

biceps and triceps positions, two rigid bodies mounted along the dorsal and ventral forearm, as well as two rigid bodies attached to the hand. In cases where the virtual landmarks were referenced by two or more rigid body clusters, an optimal Bayesian estimation [109] determined the location of the point used for evaluation.

2.4.2 Model Identification

As a precursor to the experiments, and to determine the appropriate range of motion for each of the nine aforementioned joint angles, the subject performed a range of exercises tailored to measure the full range of motion of one joint at a time.

Unconstrained scapular joint limits: The first test was to measure the limits of scapular retraction and protraction (θ_1). For this experiment, the subject moved the glenohumeral joint as far in front and behind the coronal plane of the body while attempting to maintain neutral posture. The tests were repeated several times to evaluate the absolute maximum and minimum achievable angles by the subject without external intervention. The results for this test are shown in Fig. 2.5(a). The next test measured scapular elevation and depression (θ_2) where the subject elevated and depressed the shoulder complex as far as possible while maintaining a stable torso posture in Fig. 2.5(b).

Unconstrained shoulder complex: Both flexion and extension (θ_3) as well as adduction and abduction (θ_4) were used to evaluate joints 3 and 4. The results are shown in Fig. 2.5(c) and Fig. 2.5(d), respectively. Adduction and abduction of the upper arm was evaluated by having the subject stand and elevate the arm from anatomical zero in the $x - z$ (coronal) plane until the maximum height of the palm was reached. Flexion and extension were evaluated in a similar fashion along the $y - z$ (sagittal) plane. Medial and lateral rotation of the glenohumeral joint was measured by abducting the right arm by $\pi/2$ radians and the elbow flexed at $\pi/2$ radians. The subject then attempted internal and external

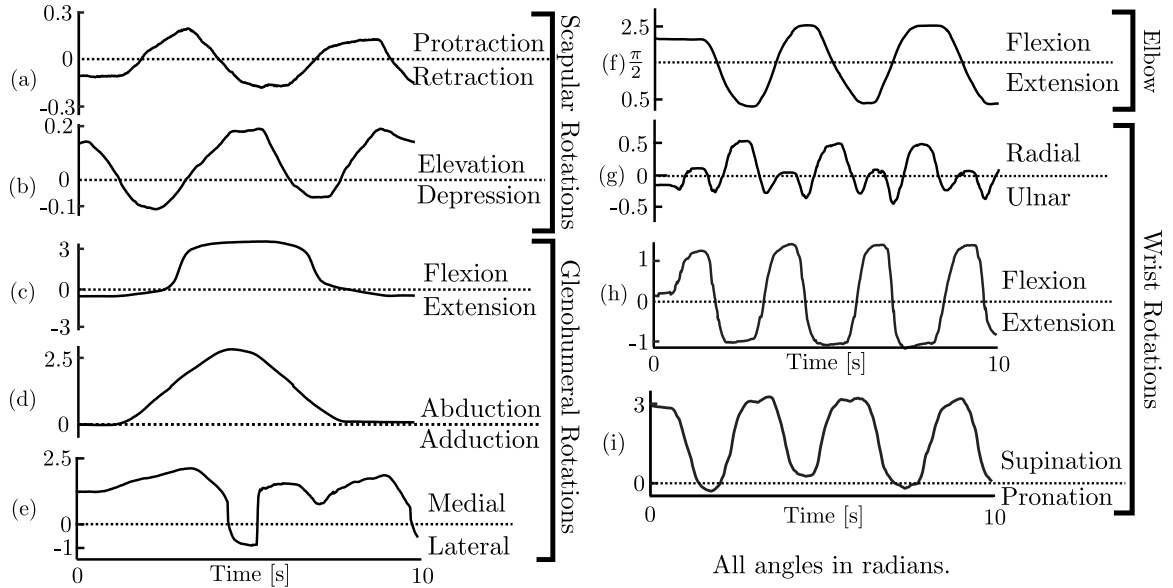


Figure 2.5: Unconstrained joint limits. (a) and (b) demonstrate the scapular retraction/protraction and elevation/depression, respectively. (c), (d), and (e) represent the shoulder adduction/abduction, flexion/extension, and medial/lateral rotation, respectively. (f) represents the humeroulnar joint, (g) is the wrist ulnar/radial deviation, (h) is the wrist flexion/extension, and (i) demonstrates wrist pronation and supination. All angles along the vertical axis are shown in radians.

rotation of the forearm while maintaining a static position of the humerus. Results of this experiment for θ_5 are shown in Fig. 2.5(e).

Unconstrained elbow complex: Fig. 2.5(f) demonstrates flexion and extension of the elbow (θ_6) which was evaluated by starting at anatomical zero with an outward facing palm and then complete full flexion and extension movements along the sagittal plane.

Unconstrained wrist complex: Fig. 2.5(g) demonstrates wrist ulnar/radial deviation (θ_7). Fig. 2.5(h) shows wrist flexion and extension (θ_8), and Fig. 2.5(i) demonstrates pronation and supination of the wrist (θ_9). The numerical values for the results are shown in Table 2.3. Note that the numerical values are with respect to the kinematic model described in Section 2.2.

Table 2.3: Regular range of motion w.r.t ideal rest angle θ_i^0 (anatomical zero)

	θ_1	θ_2	θ_3	θ_4	θ_5	θ_6	θ_{6c}	θ_7	θ_8	θ_9
θ_i^0	0	0	0	90	0	20	90	0	0	0
θ_i^l	-14.1	-6.4	-21.3	0.4	-68.0	15.8	64.2	-27.9	-72.1	-5.0
θ_i^u	13.4	12.2	180.0	160.7	133.0	150.5	114.0	29.7	81.2	179.4

The subject then donned a thermoplastic brace to the elbow joint to incur a constraint on the individual to demonstrate the validity of the kinematic model as shown in Fig. 2.4(b). Range of motion tests were done with the constrained joint similar to that of Fig. 2.5(f) to determine the range of motion for the constrained elbow (θ_{6c}) which was found to be between 1.12 rad (64°) and 1.99 rad (114°). With this information, the model was adapted to fit the newly measured limits using Equation (2.11). The subject was found to have link lengths of: clavicle = 188 mm, humerus = 286 mm, radius/ulna = 259 mm, and wrist to palm centre = 74 mm. Note that the link lengths correspond to the length between each of the rotational centres of motion and not the length of the bone segments. All values of the joint limits for the range of motion were entered into the simulation model to be used in the assessment of the remaining experiments in this chapter. Following the range of motion tests, a series of workspace evaluation experiments were conducted to evaluate the performance of the kinematic model.

2.4.3 Scenario 1 Experimental Results

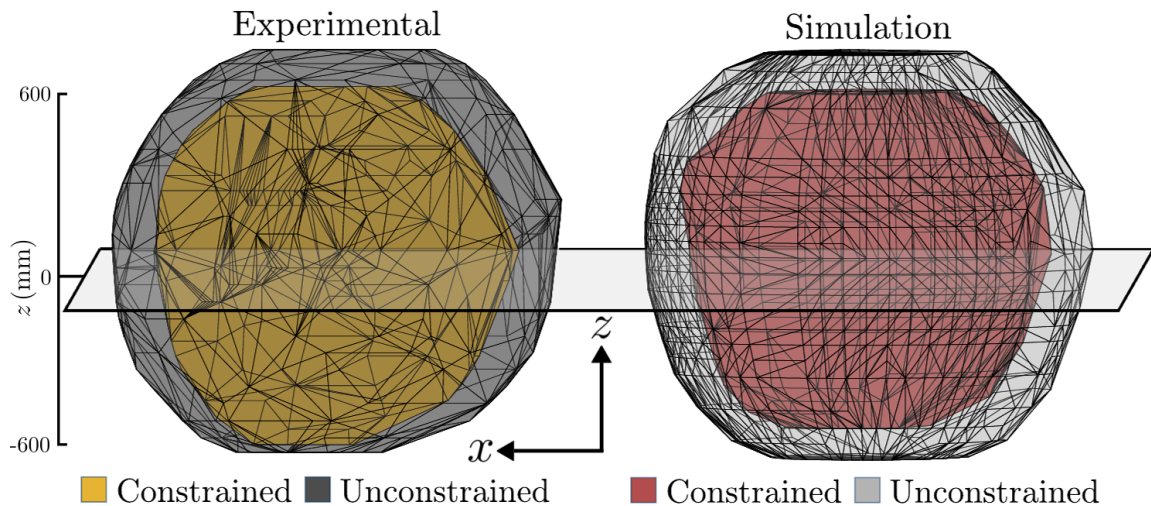


Figure 2.6: Experimental and simulated convex hull and slice profile for $z = 0$ mm with respect to the subject's sternoclavicular joint. Note that the constrained workspace is a subset of the unconstrained workspace. The 2-dimensional workspace slice profile is shown in Fig. 2.7

The subject was asked to achieve a reachable workspace by performing a series of movements with an extended arm. Careful precaution was taken to attempt to create a sphere around the subject that best represented the total reachable workspace. The model was compared to the actual reachable workspace of the subject using in vivo motion capture as outlined above. In the first set of experiments, the subject performed the tests to evaluate

the total reachable workspace of the individual with no physical limitations to any of the nine joint angles. After this workspace was evaluated, the subject then donned the thermoplastic brace that limited the range of motion of (θ_6) from 0.28 rad to 2.63 rad to (θ_{6c}) which was between 1.12 rad and 1.99 rad. The tests were then duplicated to evaluate the total reachable workspace of the individual under this joint limitation. Convex hull spheres of the resulting experimental and simulated workspaces are shown in Fig. 2.6. Note that the constrained workspaces are a subset of the unconstrained workspaces in both the simulated and experimental cases. Fig. 2.6 also contains a transverse plane situated about the subject's sternoclavicular joint, in which planar images of the workspace can be obtained to better demonstrate the workspaces. Throughout this chapter, all Cartesian translations are with respect to a reference frame with its origin centred at the subject's right sternoclavicular joint. The x-axis of this reference frame is along the coronal plane, parallel to the ground. The y-axis of this reference frame is along the sagittal plane, parallel to the ground. The z-axis, centred at the sternoclavicular joint, runs collinear to a gravitational vector, pointing in the direction of the subject's head. A reference frame with this convention is shown in each figure.

Multiple tests were run to collect information on palm locations in Cartesian space under both constrained and unconstrained conditions of the elbow. This was then compared to the simulated model and an overview of the results are shown in Fig. 2.6. This figure is then extended by demonstrating points of the experimental and simulated workspaces about the transverse slice in in Fig. 2.7. This slice and other slices in this chapter were constructed by considering all measured points within ± 10 mm of a transverse plane referenced to the z-axis. In total, 13 slices situated 100 mm apart from one another were evaluated for the experimental and simulated, constrained and unconstrained workspaces. Fig. 2.8 demonstrates six slices above the sternoclavicular joint, with a final slice at 600 mm above this reference frame. Both the experimental and simulated values are superimposed to demonstrate model accuracy. It is important to note that for these experiments, the total reachable workspace was evaluated and not the total dexterous workspace. That is, the Cartesian position of the end-effector was the only variable to be considered and not the orientation of the palm. The simulated model demonstrates all possible palm locations for all valid arm topologies. For example, the island points in the encased dashed box in Fig. 2.7 can be physically achieved by an over-the-shoulder topology. The slices shown in Fig. 2.8 illustrate the achievable regions in which a constrained and unconstrained elbow with the provided joint limitation can physically reach. Note that for slices $z = 100$ mm to $z = 400$ mm, the locations near point $(x, y) = (0,0)$ have cutouts for the subject's head.

In each of the slices demonstrated by Fig. 2.8 and Fig. 2.9, both the experimental and

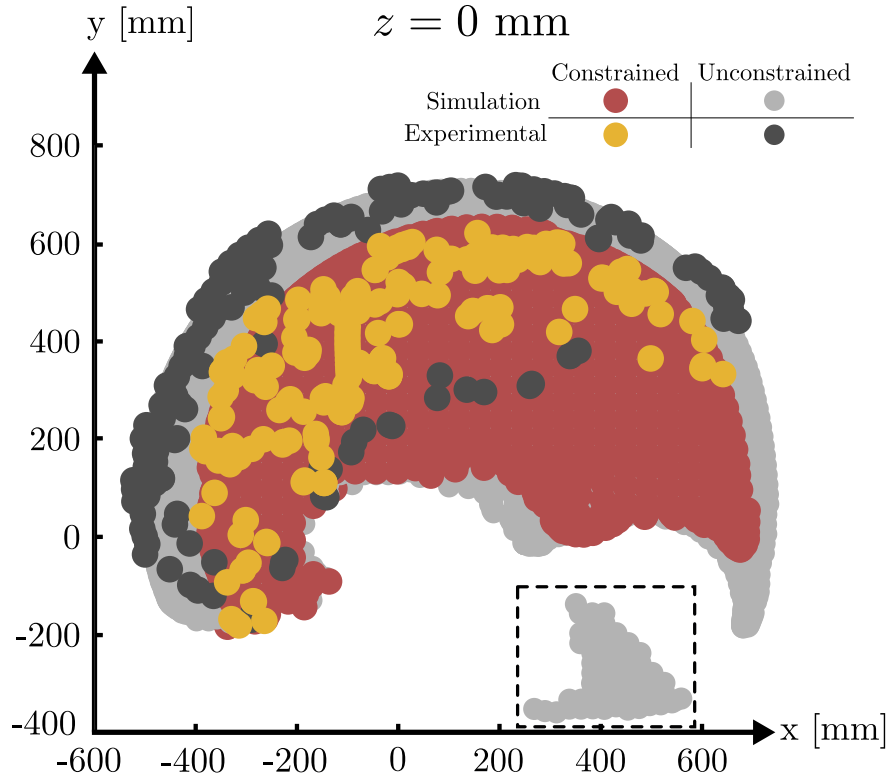


Figure 2.7: Slice at $z = 0$ mm in the workspace volume shown in Fig. 2.6. $z = 0$ mm represents the transverse plane located at the subjects sternoclavicular joint. The locations encapsulated by the dashed box represent reachable locations from an over-the-shoulder topology.

simulated values for the constrained and unconstrained cases compose similar curvatures. As shown, the slices demonstrate that the model can accurately represent experimental data. Similarly for slices under the sternoclavicular reference frame in Fig. 2.9, cutouts for the subject's torso and lower extremities were provided.

2.4.4 Scenario 2 Experimental Results

In addition to the emulated internal elbow constraint, two experiments were run to evaluate the workspace of the subject under additional end-effector constraints as well as to measure the joint angles throughout the externally constrained motion. In the first experiment, shown in Fig. 2.3(b), the subject manipulated a device that constrained the end-effector translation to the sagittal plane. This experiment was conducted at varying radii to validate the performance of the model to evaluate the constrained joint limits. Both scenarios were subject to a new set of constraints, namely the position of the palm (subject to be constrained along the plane $x = 150$ mm, measured mean $x = 149.80$ mm), and orientation

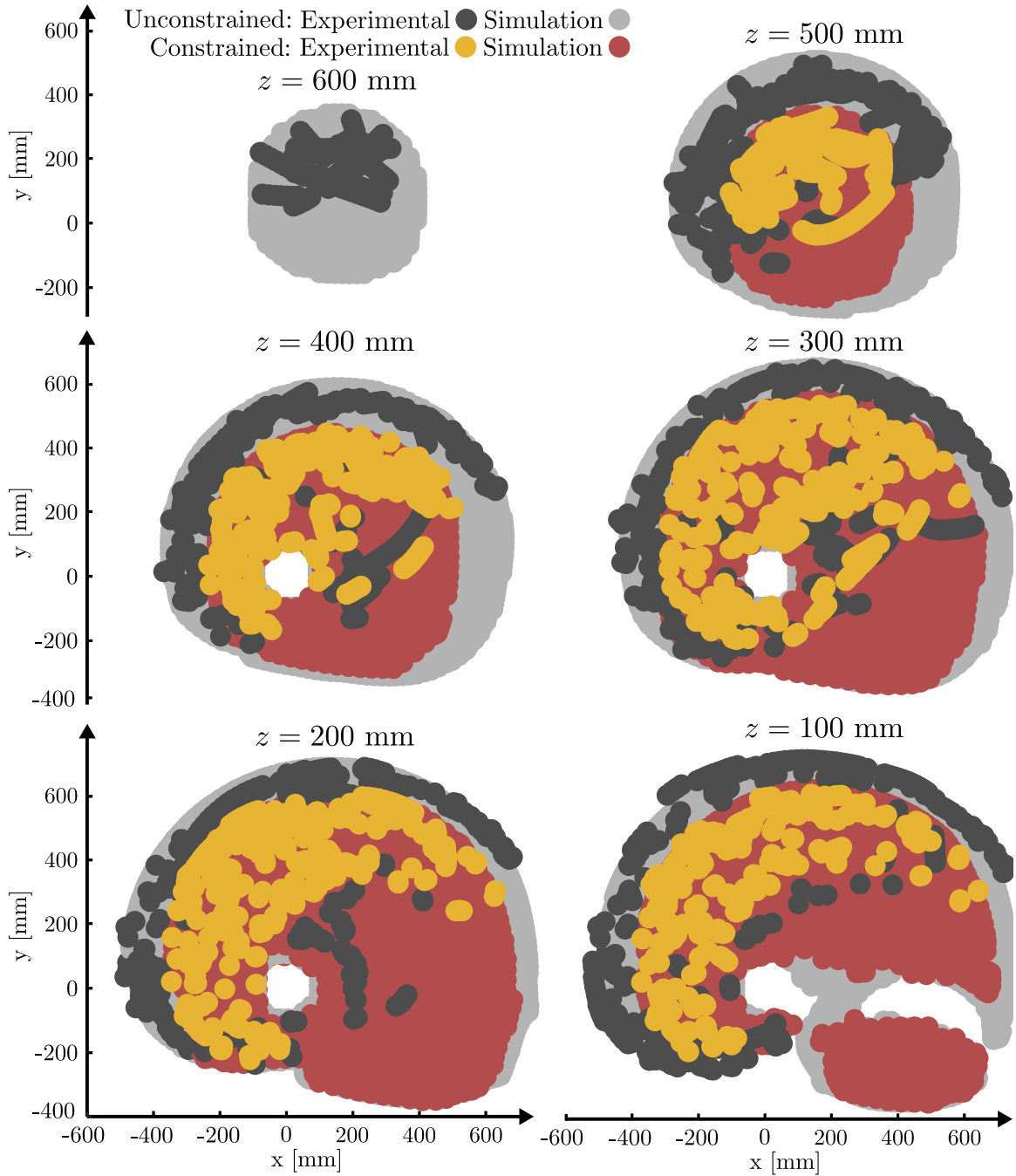


Figure 2.8: Experimental and simulated slices of the constrained and unconstrained workspaces along the z axis referenced from the sternoclavicular joint as in Fig. 2.6. For slices $z = 100$ mm to $z = 400$ mm, cutouts of the subject's neck and head are displayed.

constraints (hand roll = 0 rad) in Equation (2.4-2.6):

$$\psi(\mathbf{q}) = 0 \text{ rad} \quad (2.17)$$

$$x(\mathbf{q}) = 150 \text{ mm} \quad (2.18)$$

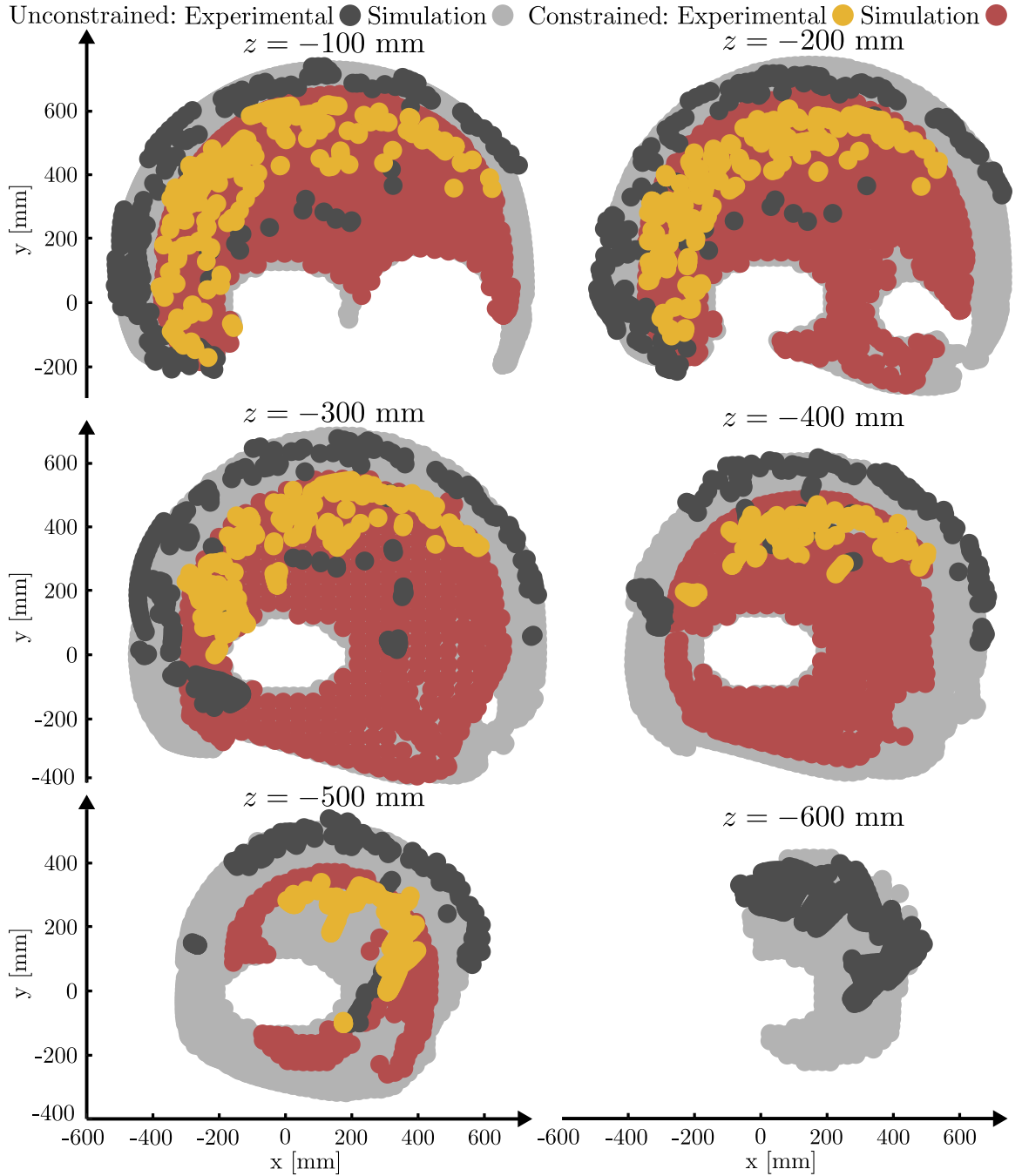


Figure 2.9: Experimental and simulated slices of the constrained and unconstrained workspaces along the z axis referenced from the sternoclavicular joint. For slices $z = -100$ mm to $z = -600$ mm, cutouts of the subject's torso and legs are demonstrated.

and, therefore, the Jacobian defined in Equation (2.12) becomes:

$$\mathbf{J}_c(\mathbf{v}) \in \mathbb{R}^{4 \times 9} = \begin{bmatrix} \frac{\partial y(\mathbf{v})}{\partial v_1} & \frac{\partial y(\mathbf{v})}{\partial v_2} & \cdots & \frac{\partial y(\mathbf{v})}{\partial v_9} \\ \frac{\partial z(\mathbf{v})}{\partial v_1} & \frac{\partial z(\mathbf{v})}{\partial v_2} & \cdots & \frac{\partial z(\mathbf{v})}{\partial v_9} \\ \frac{\partial \varphi(\mathbf{v})}{\partial v_1} & \frac{\partial \varphi(\mathbf{v})}{\partial v_2} & \cdots & \frac{\partial \varphi(\mathbf{v})}{\partial v_9} \\ \frac{\partial \gamma(\mathbf{v})}{\partial v_1} & \frac{\partial \gamma(\mathbf{v})}{\partial v_2} & \cdots & \frac{\partial \gamma(\mathbf{v})}{\partial v_9} \end{bmatrix} \quad (2.19)$$

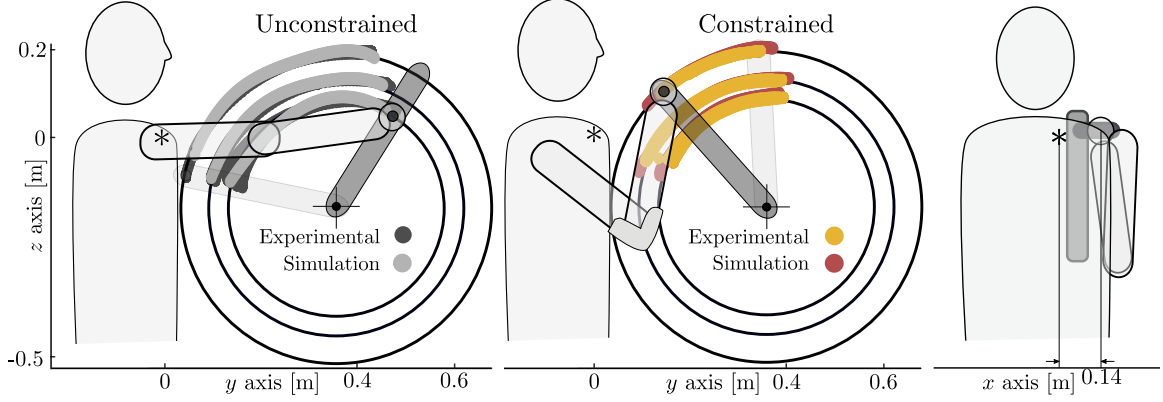


Figure 2.10: Results of experimental and simulated workspace evaluation of Scenario 2 at device radii $r = 270$ mm, 330 mm, and 375 mm. Device centred 360 mm in front of sternal notch (y) and 160 mm below sternal notch (z).

The simulated and measured results are shown in Fig. 2.10. It is apparent that the model accurately conveys the capabilities of the subject provided with both internal (or simulated internal θ_{6c}) and external constraints (palm fixed along the sagittal plane $x = 150$ mm). Taking this a step further, the behavior of each of the nine kinematic joints throughout the experiments were measured to provide insight on the role of each joint in constraint compensation. This is useful in the context of evaluating joint motions throughout a particular task. Fig. 2.11(a) demonstrates the effect of the movement along the sagittal plane on the unconstrained elbow joint and Fig. 2.11(b) demonstrates the constrained case. Note that only the internally constrained joint (θ_{6c}) and the constrained end-effector ($\theta_{7,8,9}$) are displayed.

2.4.5 Scenario 3 Experimental Results

Similar to Scenario 2, Fig. 2.3(c) demonstrates the third experimental scenario, with constrained translational motion to the $x - z$ (coronal) plane. The subject manipulated the cyclic device in one of three preset radii and a new set of constraints imposed on the subject with the palm constrained along a plane parallel to the coronal plane at $y = 400$ mm, as well as the roll of the wrist, similar to Scenario 2:

$$\psi(\mathbf{q}) = 0 \text{ rad} \quad (2.20)$$

$$y(\mathbf{q}) = 400 \text{ mm} \quad (2.21)$$

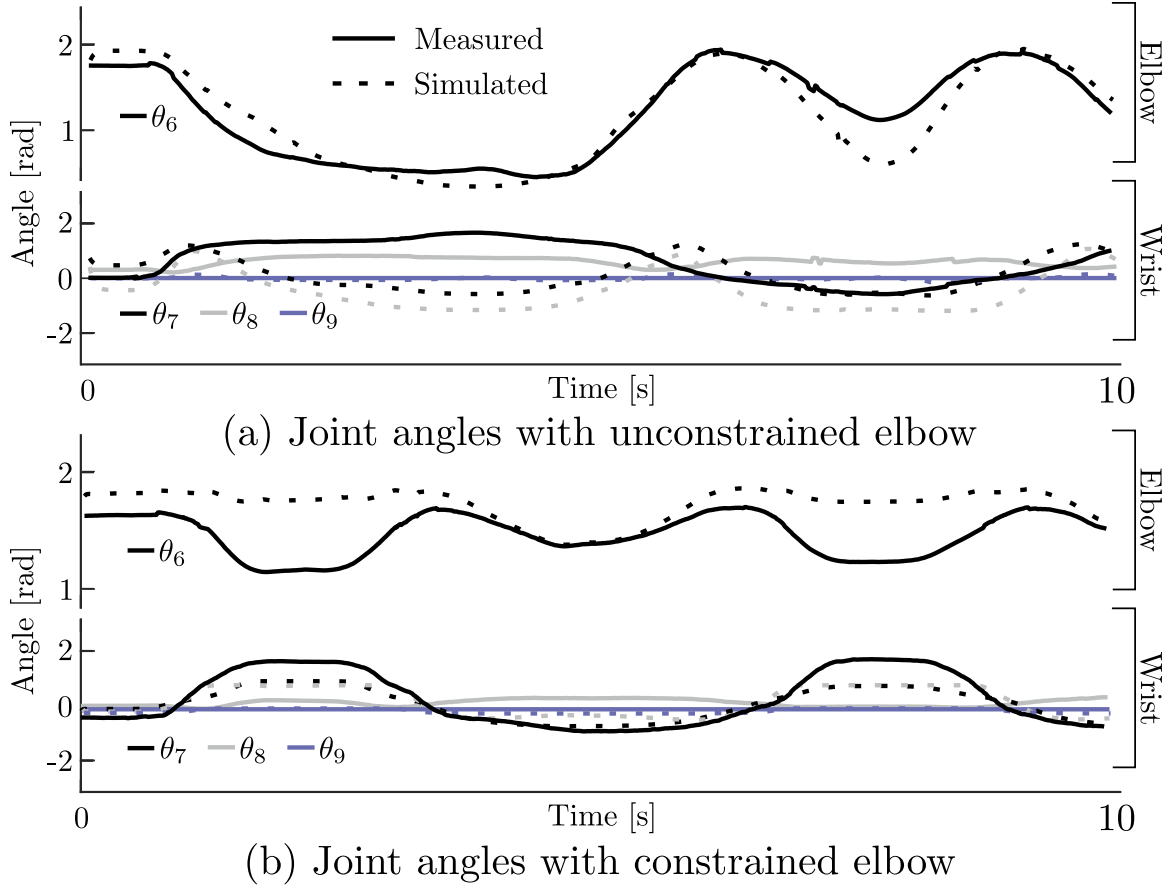


Figure 2.11: Joint trajectory results of Scenario 2. (a) No constraint on the subject's elbow. (b) Subject has donned an elbow brace constraining movement of the elbow. Dashed lines represent the simulation and solid lines represent experimentally obtained information on the joint angles.

which results in the following updated Jacobian:

$$\mathbf{J}_c(\mathbf{v}) \in \mathbb{R}^{4 \times 9} = \begin{bmatrix} \frac{\partial x(\mathbf{v})}{\partial v_1} & \frac{\partial x(\mathbf{v})}{\partial v_2} & \cdots & \frac{\partial x(\mathbf{v})}{\partial v_9} \\ \frac{\partial z(\mathbf{v})}{\partial v_1} & \frac{\partial z(\mathbf{v})}{\partial v_2} & \cdots & \frac{\partial z(\mathbf{v})}{\partial v_9} \\ \frac{\partial \varphi(\mathbf{v})}{\partial v_1} & \frac{\partial \varphi(\mathbf{v})}{\partial v_2} & \cdots & \frac{\partial \varphi(\mathbf{v})}{\partial v_9} \\ \frac{\partial \gamma(\mathbf{v})}{\partial v_1} & \frac{\partial \gamma(\mathbf{v})}{\partial v_2} & \cdots & \frac{\partial \gamma(\mathbf{v})}{\partial v_9} \end{bmatrix} \quad (2.22)$$

The results shown in Fig. 2.12 demonstrate that the model can also determine the feasible workspace while adhering to the constraints provided in this scenario. Additionally, this evaluation method determined the response of each of the nine joint angles with respect to the hand position and orientation. The goal of these experiments was to observe the correlation between the path used and the respective joint angles for a

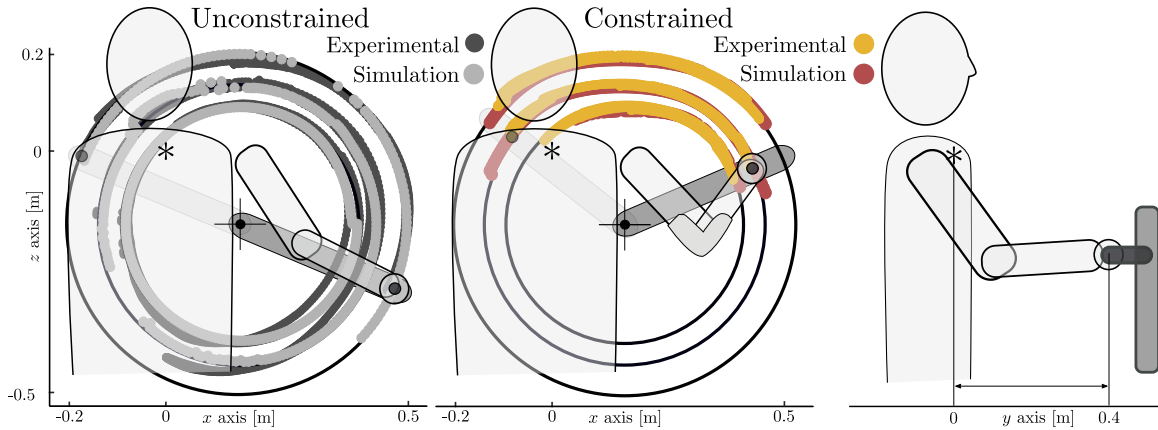
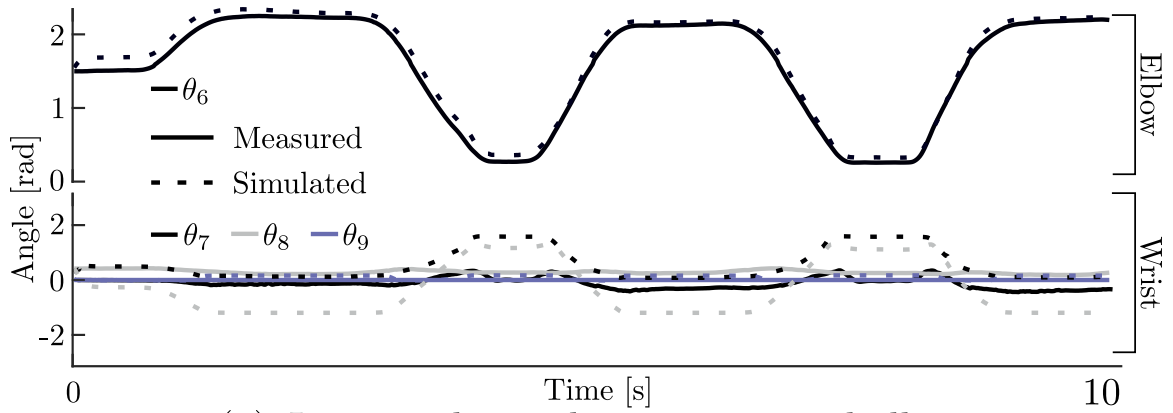


Figure 2.12: Results of experimental and simulated workspace evaluation of Scenario 3 at device radii $r = 270$ mm, 330 mm, and 375 mm. Device centred 160 mm in the x -axis with respect to the sternal notch and 160 mm below sternal notch (z). Device is situated parallel to the coronal plane of the user at $y = 400$ mm.

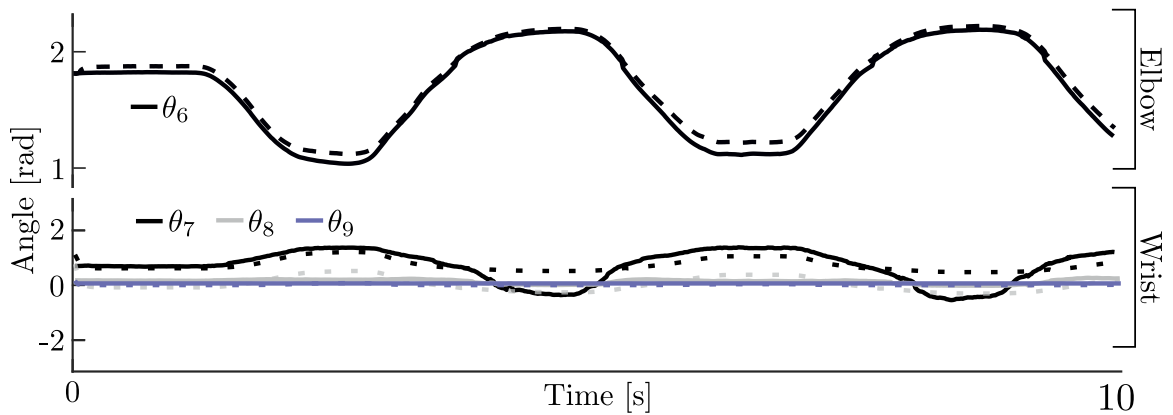
specified trajectory with the simulated model trajectory. Also, with the joint constraints, the subject compensates for the injury by emphasizing movements of the uninjured joints more so than the injured joint. For this cyclic motion task, Fig. 2.13 shows that the simulated model, even with an elementary cost function, accurately estimates the motion of the constrained and unconstrained joint θ_6 . This validates the use of the model in determining joint activation for a particular task, which in turn could be used to tailor rehabilitation tasks to a specific injury as per a professional clinical recommendation.

2.5 Conclusions

The 9-DOF kinematic model of the human upper limb complex derived in this chapter accurately demonstrates the workspace envelopes embodied by a constrained range of motion. The constrained differential inverse kinematic solution begins with mapping the limitations of each joint to a saturation function. Saturating joint velocities when joint angles approach their limits ensures that the inverse kinematic solution is bounded to the feasible range. Incorporating workspace evaluation using the kinematic model of the upper limb can open up several research avenues. It is well known that the central nervous system selects a pathway by minimizing a given cost function [108, 110]. In the current form, one can clearly see that the trajectory derived from the differential inverse kinematic model is a straight path, which assumes that individuals tend to select a path that minimizes metabolic energy costs [107, 108]. Nevertheless, this is not always the case and it is possible to modify the model in order to select alternative paths that minimize a combination of displacement,



(a) Joint angles with unconstrained elbow



(b) Joint angles with constrained elbow

Figure 2.13: Joint trajectory results of Scenario 3. (a) No constraint on the subject’s elbow. (b) Subject has donned an elbow brace constraining movement of the elbow. Dashed lines represent simulated data and solid lines represent experimentally obtained information on the joint angles.

velocity, and/or acceleration of specific joints between those points. In future research, this methodology can be combined with strength prediction methods, as a function of hand location and direction [111], to provide a more thorough analysis of the capabilities of the subject.

Chapter 3

Design of the Differentially-Clutched Series Elastic Actuator¹

3.1 Introduction

MUSCULOSKELETAL disorders (MSDs) do not discriminate and can develop into a chronic disability if left untreated. Since the symptoms associated with these disorders can vary widely, appropriate treatment must focus on the unique disorders and conditions of each individual [112]. This is particularly relevant for robots used in rehabilitation, where quantitative assessment of MSDs is important for evaluating potential effects of treatment [93], guiding the design of a robotic system that complies with the individual's unique needs and motion tolerances [113], and ensuring the individual's safety and comfort during robotic intervention [114]. In particular, a robot that is adaptable to the human limb segment lengths and ranges of motion is crucial. Furthermore, when designing robotic rehabilitation strategies, clinical standards must be considered in order to retain compatibility with traditional therapies while involving minimal robot programming.

The previous chapter demonstrated a method of determining the workspace of a patient, which is useful for generating the uniquely-tailored kinematic topology of a rehabilitation device. However, the actuation strategy of the rehabilitation device is pivotal in ensuring patient safety. The physical interaction between the human and a robotic device must take many forms in the context of rehabilitation. First, the device must be able to assist the patient if the patient is unable to complete a predetermined task. As the patient

¹© 2019 IEEE. Partially reprinted, with permission, from B. DeBoon, S. Nokleby, N. La Delfa, and C. Rossa, "Differentially-Clutched Series Elastic Actuator for Robot-Aided Musculoskeletal Rehabilitation," presented at the IEEE *International Conference on Robotics and Automation (ICRA)*, Montreal, Canada. pp. 1507–1513.

regains strength and/or range of motion, the rehabilitation device should be able to change operating modes, and resist the motion of the patient in order to strengthen the injured joint or joints. In addition to these aforementioned operating modes, the device must be compliant [24], that is, the device must encompass properties of a flexible or supple material to aid in manipulation as well as to reduce impact forces. In the context of active actuators, only backdrivable (the ability to be reversed by a human) motors can be considered compliant. The issue with using backdrivable motors is the low force bandwidth for suitable-sized electric motors. Therefore, there is a trade-off between compliance and force bandwidth in strictly active devices. This raises an interesting issue, as the conditions for an ideal rehabilitation device must satisfy the following:

1. The device must be compliant and safe to operate, i.e., the user must have the ability to move the device without external inputs,
2. The device must be able to provide adequate force/torque to the patient to administer meaningful assistance,
3. The device must be able to provide a large resistive force/torque to strengthen affected joints, and
4. The device must be able to measure or infer the force/torque of the end-effector.

The remainder of this chapter is dedicated to the development of an actuator that satisfies the above conditions. The differentially-clutched series elastic actuator (DC-SEA) is a novel hybrid actuator designed for safe human-machine interaction (HMI). The chapter is organized as follows: Section 3.2 introduces the novel differential clutch mechanism for elastic actuators. Section 3.3 demonstrates the proof-of-concept version of the multimodal series elastic actuator, as well as the strategies involved in satisfying the above list of conditions. Section 3.4 evaluates the governing equations for the operation of the DC-SEA, and Section 3.5 contains experimental results for a simple preliminary controller. An advanced controller for the multi-input actuator is proposed and evaluated in the next chapter of this thesis.

3.2 Differential Clutch

In this chapter, we propose the addition of a clutch to elastic actuators in the form of a differential clutch. The term differential clutch refers to an element encapsulating the abilities of a traditional clutch, with the added benefit of indirectly controlling the amount

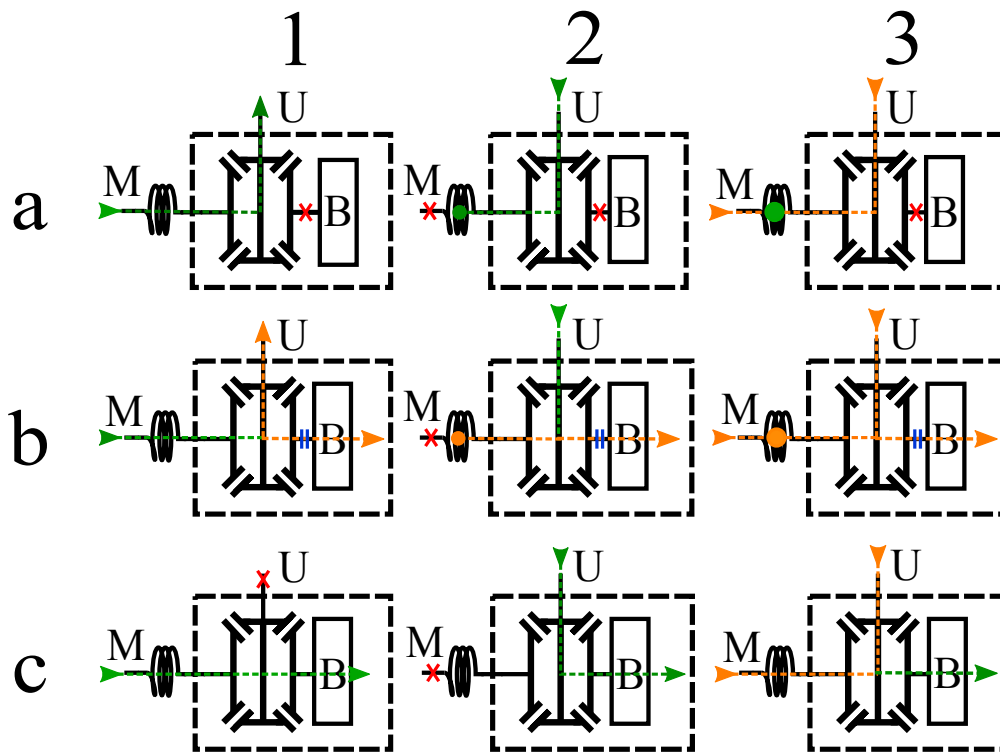


Figure 3.1: Differential Clutch. The dashed rectangle represents the component makeup of the differential clutch, the differential gearbox and a controllable brake. Note that the clutch includes the brake has only two externally connected members; Motor/Spring and User. Orange arrows represent a division of energy, green arrows represent the sum of the energy or the total energy in the clutch. Green or orange dots represent potential energy stored in the spring. Red crosses refer to locked shafts within the actuator, and blue parallel lines represent a braking effort on that shaft. Row a-c represent the three operating modes, and columns 1-3 represent test conditions. Row a.) represents the case under which the brake is fully engaged, and thus the clutch is engaged as well. Row b.) represents the partially engaged case, where some of the energy is dissipated by the braking effort. Row c.) represents the final case, where the brake is disengaged and thus the brake connected differential gear is free to rotate. Column 1.) represents the case where the motor is supplying kinetic energy and, therefore, is in active mode. Column 2.) represents the case in which the motor is inactive and the user is introducing rotational kinetic energy to the actuator. Column 3.) highlights the case in which both the motor and user are introducing rotational kinetic energy to the system and the brake is used to facilitate the amount of energy in the system. This column is considered as resistive mode.

of torque transferred from one body to another. The differential clutch is made up of a differential gearbox and a magnetic particle brake attached to one planetary gear. The structure and operation of the clutch is elaborated in Fig. 3.1. The advantage of adding a differential gear to an elastic actuator is the ability to serially couple and decouple the active/elastic elements [115] while guaranteeing compliance through the use of a spring connected to one of the differential gears [67]. The introduction of a clutch means that the energy stored in an elastic element can be instantaneously dissipated to zero deformation. In situations where a residual torque is desired, it may not be adequate to completely dissipate the energy stored in the spring and sequentially increase the deflection until the desired output torque is achieved. Consider a scenario in which a human operator and a robot are collaborating in lifting a large object. If a collision between the robot and a bystander is detected, it is not sufficient to simply release a clutch mechanism. This would cause the object to drop, potentially harming the workpiece, the human collaborator, or both. A torque is desired to maintain the movement without dropping the piece while reducing the energy to minimize damage to the bystander. Therefore, it is desirable to have continuous control over the amount of stored energy in the actuator. Controlling dissipation can be achieved through two methods: by actively controlling the motor side deformation of the elastic element and by passively dissipating the energy stored in the elastic element. The advantages of controlling the energy actively is that the motor is able to maintain a deflection and compensate for overdissipation [116], with the drawback of potential instability in the event of overcompensating for natural resonance in the spring [117]. Passively controlling the deflection ensures that the system remains stable, while quickly and efficiently dissipating stored energy in the actuator [53]. The main drawback of the inclusion of passive elements to the elastic actuator include increased mass and the issue around control of multi-input actuators.

Differential clutches have the advantage of allowing three separate bodies to rotate at different speeds. The use of a differential clutch decreases the total mass of the actuator as compared to the addition of multiple standard clutch systems, adds a mode of redundancy to improve safety, and reduces the amount of energy required to perform force control.

3.3 Proof-of-Concept

A model of the proof-of-concept differential gear system is shown in Fig. 3.2(a). The outer/larger gears are defined as planetary gears and the smaller internal gears are satellite gears. A DC motor is coupled to one of the two planetary gears of the differential through a torsion spring assembly. The other planetary gear of the differential is coupled

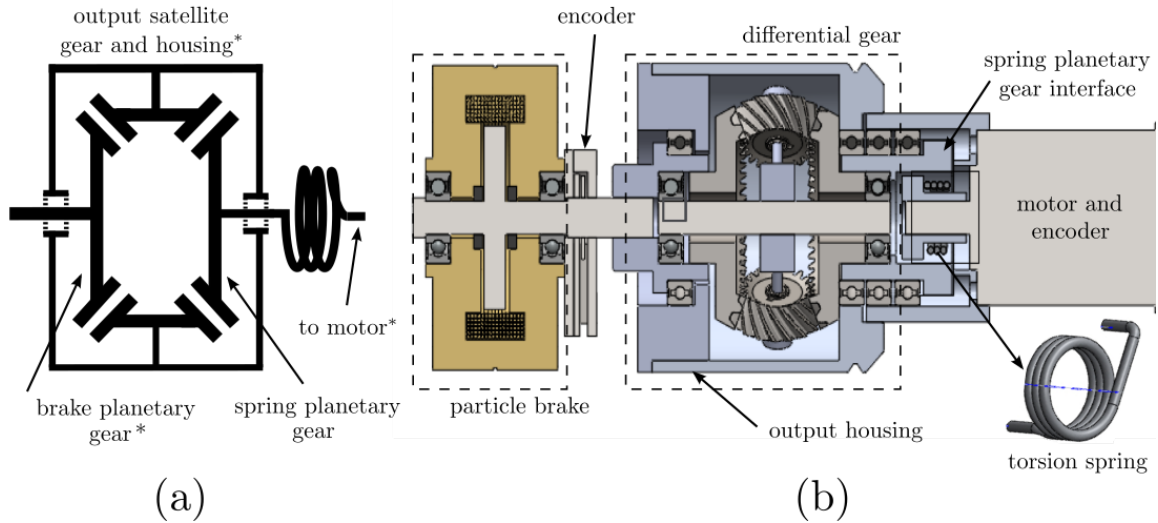


Figure 3.2: (a) Drawing of the differential gear system. (b) CAD model cross section of the DC-SEA. The asterisk indicates an encoder-measured body. See Fig. 3.3 for a schematic drawing of the operation of the actuator.

to a magnetic particle brake. There are three smaller satellite gears between the two planetary gears that are connected to the rotating output housing of the actuator as shown in Fig. 3.2(b). A spring assembly that mounts a series torsion spring between the motor and one of the planetary gears is described as the spring-planetary gear interface (see Fig. 3.2(b)). The output housing is rigidly connected to the satellite gears in the differential clutch, the housing itself acting as the output shaft. The output housing is coupled to an external encoder using a belt (not shown in Fig. 3.2). Two additional encoders with 2,048 pulses per revolution are used to measure the position of the brake and motor shafts.

The motor and encoder pair used in this actuator is a Cytron IG42E-24K with a 24:1 reduction gearbox with a nominal torque of 980 mNm with an encoder resolution of 480 pulses per revolution. The brake is a magnetic particle brake made by Placid Industries (B15-12-1) with a torque range of 34 mNm to 1,700 mNm.

The DC-SEA is able to achieve the following operating modes:

- **Free Motion** mode is designed to allow the user to rotate the shaft freely. This is done by disengaging the brake and motor. Provided that the gearbox in the DC motor has a large reduction, the motors off-state torque translates to a fixed surface connected to one side of the torsional spring. If the user rotates the output shaft, all energy introduced to the actuator will be split between the brake and the torsional spring. This mode is demonstrated in Fig.3.1(2c).
- **Elastic Mode** is when the brake is engaged and the motor is static, the device is in an

elastic state; as if the user is directly coupled to a grounded spring. The total energy stored in the spring can be controlled by adjusting the braking effort in the magnetic particle brake. This mode is demonstrated in Fig.3.1(2a).

- **Active/Resistive Mode** when both the motor and brake are engaged, the brake and differential act as a continuously variable-slip clutch between the motor-spring system and the end effector. The force transmitted to the end effector can be controlled by adjusting both the motor and braking effort in tandem. The motor can be used to compress the spring and engage the output shaft and both the motor and brake can decompress the spring to reduce the amount of stored energy, thus reducing the force applied to the end effector.

Each of these modes have applications in musculoskeletal rehabilitation. By controlling the commanded motor torque τ_{cm} and the commanded brake torque τ_{cb} , any of the above actuation modes can be achieved.

3.4 Equations of Motion

A schematic representation of the actuator dynamics is shown in Fig. 3.3. The sum of the torques about the motor shaft can be modelled by:

$$J_m \ddot{\theta}_m + b_m \dot{\theta}_m + k_s(\theta_m - \theta_s) = \tau_{cm} \quad (3.1)$$

where τ_{cm} is the torque applied by the motor, which can be related to an input voltage V_m through the equality $\tau_{cm} = K_m K_v V_m / R_m$, where R_m is the motor winding resistance, and K_m and K_v are the linear motor torque and back EMF constants, respectively. J_m is the moment of inertia about the motor shaft, and b_m is the damping coefficient of the motor. Throughout this chapter, $\dot{\theta}$ and $\ddot{\theta}$ refer to the first and second time derivative of angular position θ , respectively. Subscript m refers to any parameter associated with the motor shaft. In addition to (3.1), the torque equations for the user, spring, and brake bodies of the differential are, respectively:

$$\tau_s + J_s \ddot{\theta}_s + b_s \dot{\theta}_s + b_d(\dot{\theta}_s - \dot{\theta}_b) + k_s(\theta_s - \theta_m) = 0 \quad (3.2)$$

$$\tau_u + \tau_{app} + J_u \ddot{\theta}_u + b_u \dot{\theta}_u = 0 \quad (3.3)$$

$$\tau_b + J_b \ddot{\theta}_b + b_b \dot{\theta}_b + b_d(\dot{\theta}_b - \dot{\theta}_s) + \tau_{cb} = 0 \quad (3.4)$$

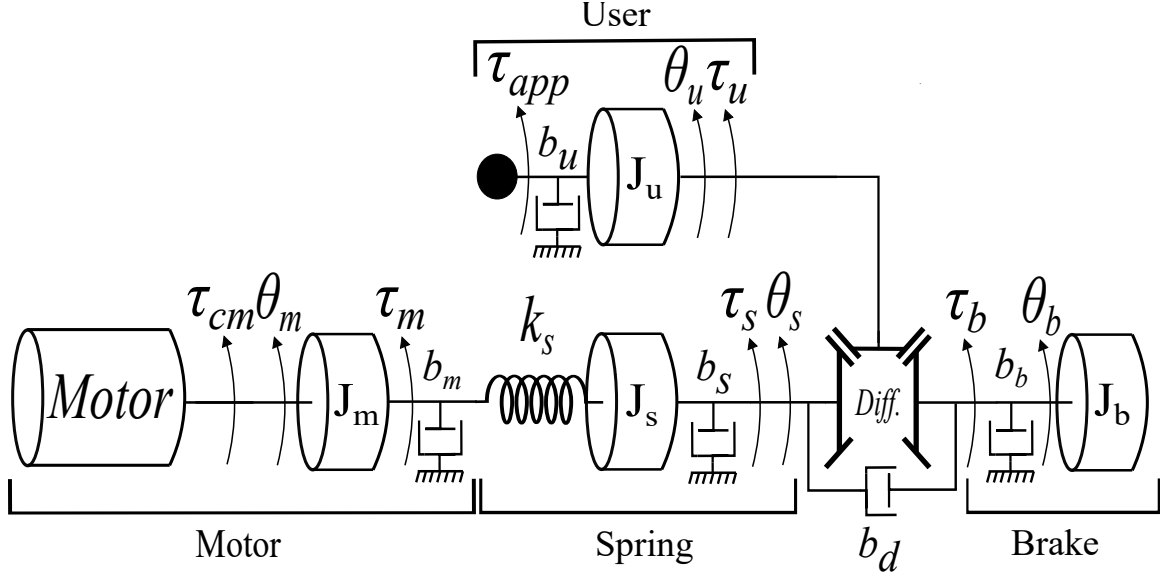


Figure 3.3: Dynamics of the differentially-clutched series elastic actuator. The user is connected to both the spring and magnetic particle brake through the differential gearbox. The motor is connected to the opposite end of the spring

where τ_s , τ_u , and τ_b are the torques of the spring, user, and brake bodies of the differential, respectively. Subscript u refers to parameters associated with the user differential body and subscript s and b relate to the spring and brake planetary gears in the differential, respectively. J_s , J_u , and J_b are the moments of inertia, b_s , b_u , and b_b are the viscous friction components, b_d is the viscous friction coefficient between the satellite and planetary gears in the differential, $\ddot{\theta}_s$, $\ddot{\theta}_u$, and $\ddot{\theta}_b$ are the angular accelerations, $\dot{\theta}_s$, $\dot{\theta}_u$, and $\dot{\theta}_b$ are the angular velocities, θ_s , θ_u , and θ_b are the angular positions about the planetary gear axis, k_s is the spring constant of the custom-made torsion spring, τ_{app} is the torque applied by the user, and τ_{cb} is the controlled braking torque of the magnetic particle brake. To model the actuator, the differential law of motion about $\dot{\theta}_s$ can be described as a function of the remaining velocity components: $\dot{\theta}_s = 2\dot{\theta}_u - \dot{\theta}_b$.

Considering the total power in the differential, coupled with efficiency coefficients η_u , η_s , and η_b to modulate for additional losses in the user-side and spring side differential gears, and the braking system, respectively, yields:

$$\eta_u \dot{\theta}_u \tau_u + \eta_s \dot{\theta}_s \tau_s + \eta_b \dot{\theta}_b \tau_b = 0 \quad (3.5)$$

Combining the torque balance in the differential $\tau_u + \tau_s + \tau_b = 0$ with Equation (3.5), and by postulating that the efficiency in the system is to be ideal, results in a set of split torque

equations $\tau_s = \tau_b = \frac{\tau_u}{2}$, which combined with Equations (3.2) to (3.4) yield:

$$(J_u + 4J_s)\ddot{\theta}_u - 2J_s\ddot{\theta}_b + (b_u + 4b_s + 4b_d)\dot{\theta}_u - (2b_s + 4b_d)\dot{\theta}_b - 2k_s\theta_m + 4k_s\theta_u - 2k_s\theta_b = \tau_{app} \quad (3.6)$$

and:

$$-2J_s\ddot{\theta}_u + (J_b + J_s)\ddot{\theta}_b - (2b_s + 4b_d)\dot{\theta}_u + (b_b + b_s + 4b_d)\dot{\theta}_b + k_s\theta_m - 2k_s\theta_u + k_s\theta_b = \tau_{cb} \quad (3.7)$$

Taking into consideration that J_u , J_m , and J_b are dominating inertial components and b_d , b_m , and b_b are the most prominent frictional components in the actuator, the remaining inertia, friction, and other dynamic losses can be neglected. The resulting equations of motion from Equations (3.1), (3.6), and (3.7) become:

$$J_m\ddot{\theta}_m + b_m\dot{\theta}_m + k_s\Delta\theta_s = \tau_{cm} \quad (3.8)$$

$$J_u\ddot{\theta}_u + 4b_d\dot{\theta}_u - 4b_d\dot{\theta}_b - 2k_s\Delta\theta_s = \tau_{app} \quad (3.9)$$

$$J_b\ddot{\theta}_b - 4b_d\dot{\theta}_u + (4b_d + b_b)\dot{\theta}_b + k_s\Delta\theta_s = \tau_{cb} \quad (3.10)$$

where $\Delta\theta_s = \theta_m - 2\theta_u + \theta_b$ is the deflection of the spring. Therefore, by controlling the deflection of the elastic element in the actuator, one can actively control the amount of torque delivered to the user, i.e., τ_{app} . The equations of motion can be manipulated further based on the operating mode of the multimodal actuator.

3.4.1 Free Motion

In this mode, θ_m is zero under the assumption that a motor with a large gear reduction is used in the actuator, where any reasonable amount of torque provided by the user will not cause the motor shaft to rotate. Thus, one can assume that when the motor is disengaged, its position remains constant. Due to the gearing in the differential, the angular position of the brake can be approximated to be twice that of the output shaft, i.e., $\theta_b \approx 2\theta_u$. The actuator inertia and viscous frictional components do cause a small deflection in the spring and, therefore, combining Equations (3.9) and (3.10) to produce τ_{app} as a function of θ_u :

$$\tau_{app} = (J_u + 4J_b)\ddot{\theta}_u + (4b_d + 4b_b)\dot{\theta}_u \quad (3.11)$$

showing that the torque experienced by the user stems from the inertia and viscous friction in the output housing and brake bodies of the differential.

3.4.2 Elastic Mode

When the motor is disengaged ($\theta_m = 0$) and the brake is fully engaged ($\theta_b = 0$), this mode fully engages the differential clutch and, therefore, nearly all energy introduced by the user is transferred to the spring. This can be shown in Equation (3.9) by:

$$\tau_{app} = J_u \ddot{\theta}_u + 4b_d \dot{\theta}_u + 4k_s \theta_u \quad (3.12)$$

3.4.3 Active and Resistive Mode

Active mode and resistive mode can be achieved by adjusting the motor torque τ_{cm} and braking torque τ_{cb} . When these modes are desired, τ_{cm} and τ_{cb} work in tandem to produce, reduce, or maintain the energy stored in the spring. The resultant torque felt by the user can be approximated to be twice the torque stored in the spring due to the differential gear ratio. The motor is used to compress the spring and engage the output shaft, where the brake provides a means of quickly and efficiently dissipating any unwanted energy introduced in the system. The equations of motion used for the actuator to follow a reference torque $\tau_{app} = \tau_{ref}$ is:

$$\tau_{ref} = J_u \ddot{\theta}_u + 4b_d \dot{\theta}_u - 4b_d \dot{\theta}_b - 2k_s \Delta\theta_s \quad (3.13)$$

where either:

$$k_s \Delta\theta_s = \begin{cases} \tau_{cm} - J_m \ddot{\theta}_m - b_m \dot{\theta}_m, & \text{if } k_s \Delta\theta_s < \tau_{ref}/2 \\ \tau_{cb} - J_b \ddot{\theta}_b + 4b_d \dot{\theta}_u - (4b_d + b_b) \dot{\theta}_b, & \text{otherwise} \end{cases} \quad (3.14)$$

The above can be used to reach the reference torque, provided that τ_{cm} and τ_{cb} are operating within the rated motor and brake torques, respectively. The first line in Equation (3.14) corresponds to the condition in which there is not sufficient torque in the spring. Since the brake is not able to provide any energy to the system, the commanded motor torque must be increased. The difference between active and resistive modes lies within the direction of the force provided to the user. Active or assistive mode applies a torque in the same direction as a particular angular positional goal, while resistive mode counteracts the motion of the user and attempts to hinder the user in reaching a particular goal. For active mode, the motor must be engaged as the brake has no way of providing energy to the user. When resistive mode is required, the bulk of the load is dissipated by the brake,

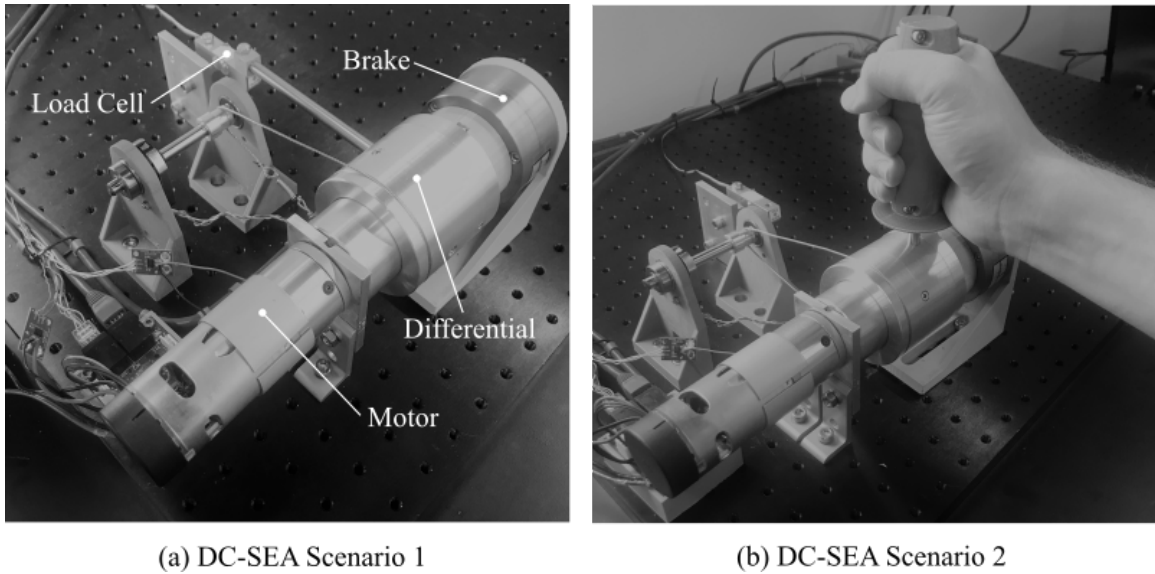


Figure 3.4: Experimental setup: (a) Scenario 1: Measuring torque from the load cell with static output housing. (b) Scenario 2: Measuring torque from the inferred spring deflection with variable user position.

increasing efficiency. By measuring the deflection in the spring, the required torques for both active and resistive modes can be achieved and maintained according to a professional therapist's recommendation.

3.5 Experimental Results

The prototype of the DC-SEA and the experimental setup used to validate the model are shown in Fig. 3.4. Two experimental scenarios were tested.

In **Scenario 1** (Fig. 3.4(a)), a handle is attached to the output housing which is then rigidly connected to a load cell to measure output torque. The load cell measurement point is located at the same height as the central axis with a perpendicular distance of 150 mm. The angular position of the output shaft is fixed to characterize the actuator and validate the model.

In **Scenario 2** (Fig. 3.4(b)), the user rotates the output shaft while the actuator attempts to maintain a reference output torque pattern, as will be shown, this is equivalent to maintaining a deflection in the spring.

The controller for the device was implemented through MATLAB and Simulink via a Humusoft MF634 data acquisition card (DAQ). The DAQ was able to take all digital and analog measurements from the rotary encoders, the load cell, and current sensors with a sampling frequency of 1000 Hz. The Simulink model calculated the error and then

converted the input into two pulse-width modulated signals passing from the DAQ to the motor and the brake through a standard H-bridge.

3.5.1 Characterization and Model Identification

The first experiment was ran in Scenario 1 to identify model parameters including stiffness of the spring. In this experiment, the motor was commanded to run at a constant velocity while the current of the brake was ramped from 0 A to 0.1 A and then back to 0 A following the temporal signal shown in Fig. 3.5(a). The measured and filtered output torque as a function of the brake current is shown in Fig. 3.5(b). The results obtained in Fig. 3.5(b) indicate a nonlinear relation between the output torque and the brake current. This is due to the magnetic saturation of the brake and its magnetic hysteresis. The resultant measured spring deflection from this experiment is shown in Fig. 3.5(c). Furthermore, it can be seen in Fig. 3.5(c) the stiffness of the custom-made spring is nonlinear and the effects of the magnetic hysteresis become more prominent. From this experiment, the stiffness of the spring in the linear range is estimated to be $k_s = 0.56$ Nm/rad.

The inertia in the different differential bodies was calculated analytically to be $J_u = 3.75$ kg·m², $J_b = 0.25$ kg·m², and $J_m = 0.20$ kg·m². The viscous friction was determined to be $b_d = 0.2$ Nm·s in the differential gears, $b_m = 0.1$ Nm·s in the motor, and $b_b = 0.1$ Nm·s in the brake.

3.5.2 Model Validation

This experiment, also run in Scenario 1, was used to show the accuracy of the model. In the experiment, the actuator was commanded to follow a square reference signal with a period of 8 seconds and a duty cycle of 50% with an amplitude of 1.5 Nm. In this experiment, the motor was open-loop controlled by providing a reference voltage and the current of the brake was used as the closed-loop control input. The spring used for this experiment had a constant of $k_s = 1.7$ Nm/rad. The parameters of the previous experiment, with the exception of the spring, were input into the model to estimate the required brake current to follow the desired output torque. A PID controller was used to regulate the brake current as shown in the block diagram in Fig. 3.6 (Scenario 1). The simulated and experimental results are shown in Fig. 3.7.

Fig. 3.7(a) shows the simulated and measured output torque response. The simulated output torque represents the torque estimated using the same model parameters and PID controller gains as the experiment. Also shown in Fig. 3.7(a), the output torque can be inferred from the spring by multiplying the measured spring deflection to the estimated

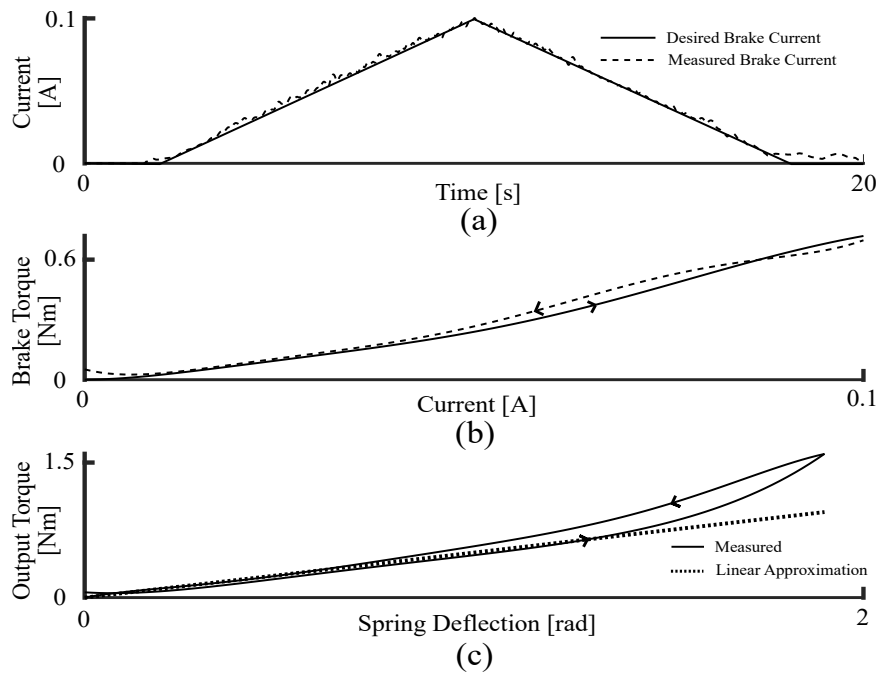


Figure 3.5: Experimental results in Scenario 1. The motor is commanded to run at a constant velocity while the current of the brake follows a curve shown in (a). The resultant braking torque as a function of the brake current is shown in (b). In (c), the actuator's output torque as a function of the measured spring deflection is shown, from which the spring constant can be estimated.

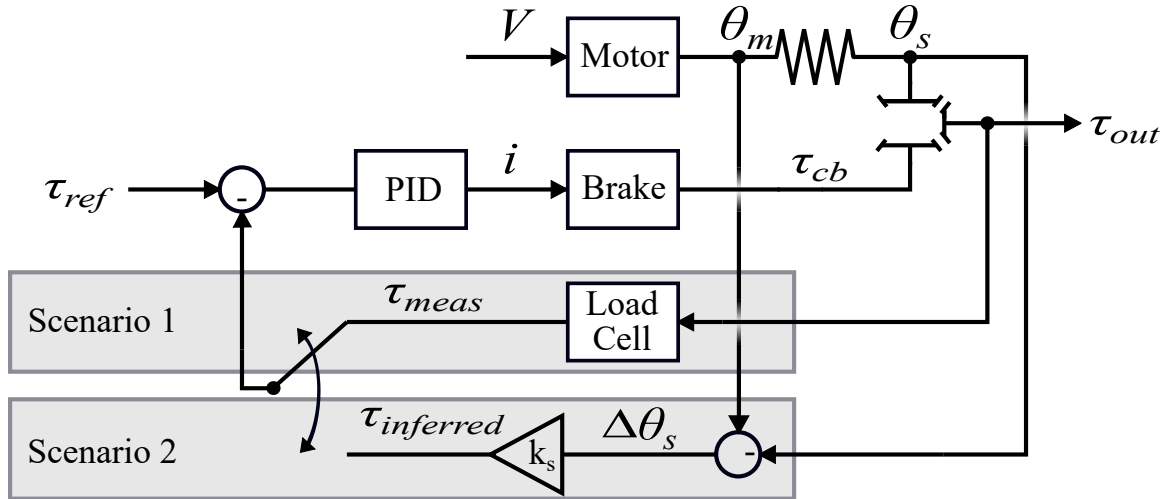


Figure 3.6: Block diagram of the control loops used to regulate the brake current in Scenarios 1 and 2. In Scenario 1, the output torque is directly obtained from the load cell measurements, whereas in Scenario 2, the output torque is inferred from the deflection in the spring.

spring constant from the previous experiment. Both the simulated and spring-inferred output torques show agreement with the measured output torque. The accuracy of the model can be confirmed by noticing that the simulated and measured brake current follow a trend as shown in Fig. 3.7(b). Fig. 3.7(c) shows the spring deflection measured from the experiment.

3.5.3 Torque Control Through Spring Deflection

From the previous experiments, it is confirmed that the output torque can be accurately represented by the deflection of the spring provided that the spring is operating within its linear range. Turning the focus to Scenario 2 (Fig. 3.4(b)), the objective now was to adhere to a specific reference torque as a user manipulated the output shaft.

A PID controller, as illustrated in Fig. 3.6, was implemented to maintain a specified output torque by controlling the deflection in the spring. Provided a reference torque τ_{ref} , the required spring deflection can be determined by: $\Delta\theta_s = \tau_{ref}/2k_s$ where $\tau_{ref} = 1$ Nm is the desired reference torque. The simulated and experimental results are shown in Fig. 3.8.

Fig. 3.8 (top) presents the measured angular position of the output shaft. Fig. 3.8 (bottom) illustrates the measured and simulated response of the actuator to a reference torque signal. As can be seen in the figure, the actuator was able to achieve the required spring deflection to maintain the reference output torque. The response shown in Fig. 3.8 (bottom) makes use of the spring deflection as a way to infer the output torque

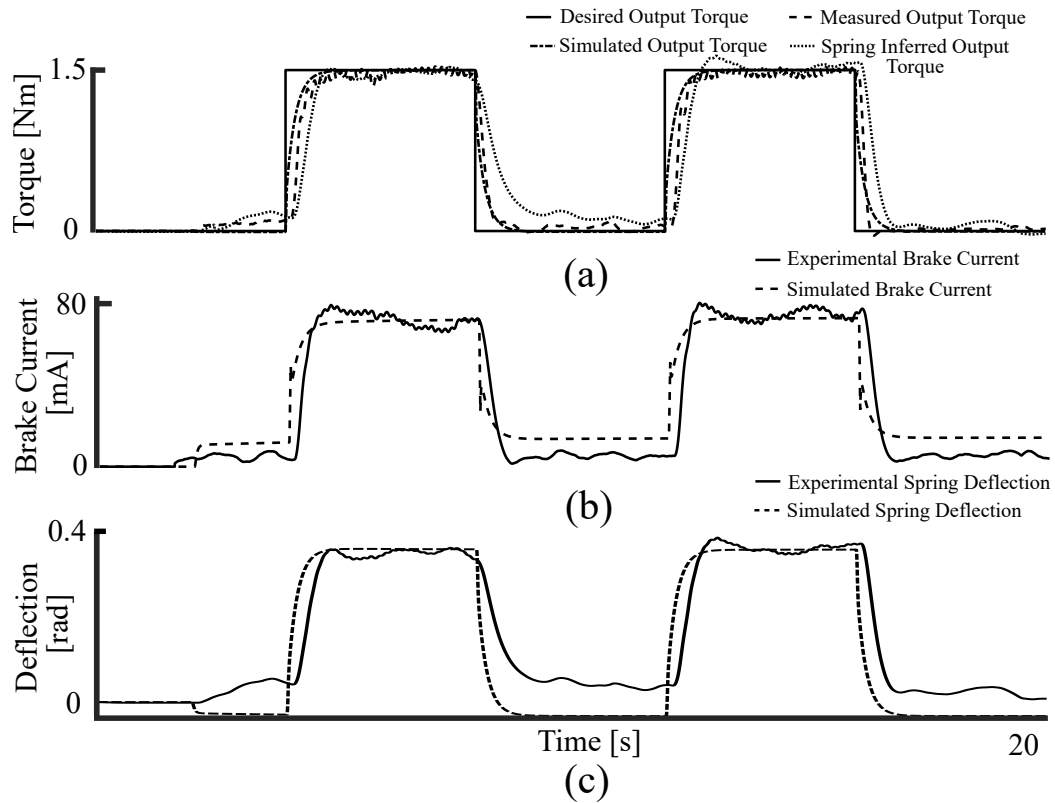


Figure 3.7: Experimental results in Scenario 1. (a) shows the actuator’s response to a reference torque along with the simulated results. (a) also shows the spring inferred output torque based on the spring constant and measured deflection. In (b), the simulated and measured brake current that is required to follow a reference torque is shown. (c) shows the measured and simulated deflection of the spring.

experienced by the user.

3.5.4 Discussion

The experiments showed the validity of the DC-SEA to provide reasonably accurate torque control. There are three methods to control the output torque. In the first method, the motor is open-loop controlled to introduce energy to the actuator while the output torque can be controlled by adjusting the current in the brake. When a motor with a high gear reduction is used, this provides a faster response and the output torque can be accurately inferred by measuring the compression in the torsion spring. Accurate characterization of the system is crucial since nonlinear effects in the spring constant, magnetic hysteresis of the brake, and viscous and static friction can strongly affect the accuracy of the model and hence that of the controller. The second method, which is not presented in this chapter, relies on fully engaging the brake and controlling the deflection of the spring through the

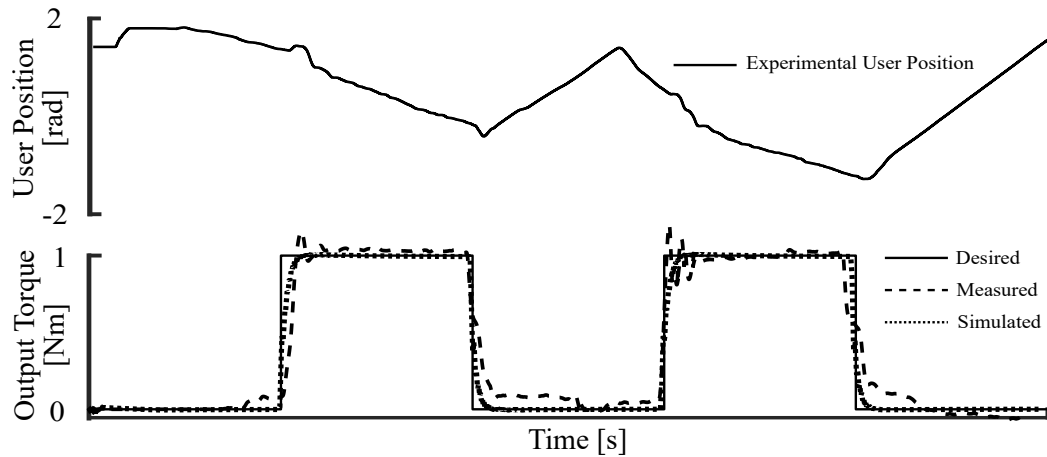


Figure 3.8: Experimental results in Scenario 2. The top figure illustrates the measured user position. The bottom figure shows the desired, measured, and simulated output torque obtained based on the deflection of the spring and estimated stiffness.

motor as in a conventional SEA. The third method makes use of closed-loop control of the motor and brake torques in tandem to provide optimal control performance in more complex reference torque patterns, such as a sudden directional change in an output torque. The proposed design allows for any of the three control methods to be used, offering a greater level of control over traditional SEAs.

The increased versatility of the actuator does come at a cost. The addition of a differential clutch increases the complexity of the mechanical design. Some notable disadvantages of the differential clutch include friction losses between the satellite and planetary gears, additional inertia, and potential backlash between the differential gear teeth.

3.6 Conclusions

The proposed actuator is designed as another step in the design of devices to be implemented in a home-based rehabilitation regime. Having access to rehabilitative devices at home, along with guidance from a professional clinician, could decrease recovery time and also allow therapists to take on a larger number of patients.

This chapter introduced a proof-of-concept differentially-clutched series elastic actuator (DC-SEA) to be used for musculoskeletal rehabilitation. The main goal of the DC-SEA is to encompass the performance requirements for differing phases of musculoskeletal rehabilitation while ensuring safety through hardware compliance. The concept consists of a brake connected to a motor-spring assembly through a differential clutch. The clutch

allows both devices and the output shaft to rotate at different speeds. The proposed design adds to the functionality of classical series elastic actuators and is able to reproduce the operation capabilities of a range of pre-existing elastic actuators.

A dynamic model of the proposed actuator was developed and tested in two different experimental scenarios. A simple torque control method was implemented to show that the output torque of the actuator can follow a specific reference dynamically by measuring the deflection of a spring. In future work, robust control methods will be explored to account for all nonlinearities caused by the spring, static friction, and the magnetic hysteresis in the particle brake.

This chapter demonstrated a rudimentary controller for a largely nonlinear plant. These nonlinearities consist of magnetic hysteresis, nonlinear deformation of the series spring, backlash in the both the differential gearbox and the motor gearbox, static friction, motor dead zones, and controller saturation. The single-input, single-output (SISO) nature of PID controllers have difficulty in effectively controlling the multivariable problem. Since a target deflection of the spring can be achieved through multiple approaches, and is a function of the operating mode, a more robust controller is required such that the device can handle both this issue around multiple solutions and the nonlinear nature of the plant. This is the subject of the next chapter.

Chapter 4

Active Disturbance Rejection Controller

4.1 Introduction

MULTIMODAL actuators combining different actuation sources or passive elements have been proven to be an effective way to improve force bandwidth and response time. This can allow physical decoupling between the motor and the operator, improving safety and allowing for active actuators with higher torque profiles to be used in close proximity to humans [1, 118]. The issue around control of such multi-input devices is generally mitigated through emphasis on the application. This means that the desired operating mode of the actuator is predetermined and added controller redundancies are selected prior to or during phased motion [76, 119]. However, in a series elastic actuator, for instance, it can be complex to control the amount of energy stored in the elastic element using a combination of two or more actuators, but it has been proven that stability can be achieved in multi-input plants [91].

There have been a number of multi-input controllers introduced throughout the literature in the form of multivariable PID controllers [120, 121], sliding-mode controllers [122, 123], internal neural model controllers [124], impedance controllers [125], and disturbance observers [89]. Multi-input disturbance observers provide an interesting approach to compensate for unmodelled dynamics while maintaining simplicity and low computational resources as it does not require training or additional learning [126]. A disturbance observer can be used to handle multi-input systems through decentralized proportional combiner control laws [127, 128] or through control laws based around mismatched disturbances woven into Hurwitz-stable error functions [129]. An example of a controller that uses disturbance observers in internal feedback loops are active disturbance rejection controllers (ADRC). Active disturbance rejection controllers are error-based and have the advantage of not requiring an exact model of the plant to achieve convergence.

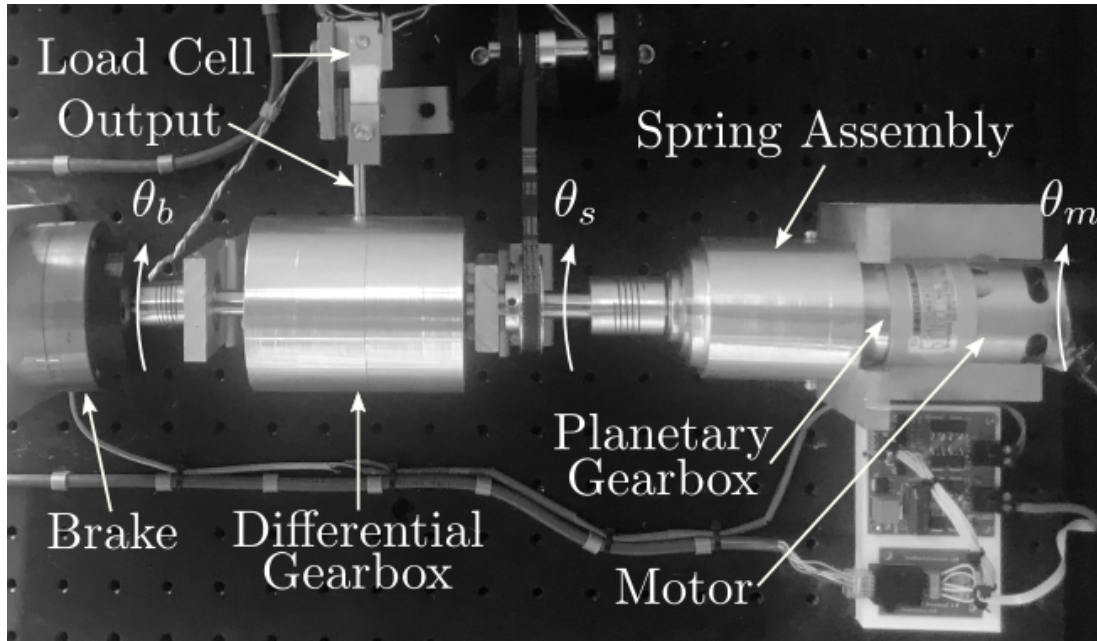


Figure 4.1: Image of the multi-input elastic actuator showing the two inputs (motor and brake) as well as the differential clutch mechanism from [71].

This makes ADRC ideal for elastic actuator control, as it is able to compensate for some nonlinearities as well as unmodelled disturbances. This is taken one step further in the context of HMI, as the operator's input is considered part of the total disturbance to the system, generating a unique approach to safely control the output torque.

This chapter introduces a backlash compensating active disturbance rejection controller for multi-input series elastic actuators. Generally, multi-input elastic actuators are designed for physical human-machine interaction to ensure the safety of an operator [71]. To provide the best estimate of the output torque experienced by the operator, the angular deflection of a torsional elastic element must be determined with high precision. To this end, even slight nonlinearities in the system can cause vast differences in output measurements and the predicted value. This is more apparent in designs encapsulating elastic elements with high elastic coefficients, as subtle changes to the measured deflection relate to large changes in predicted output torque. Deviances from Hooke's law in the measured deflection of an elastic element can be caused by a number of nonlinearities. Potential nonlinearities include elastomer hysteresis [130], nonlinear mechanical spring design [131], clutches [68], static friction, dead zones [132], input saturation [133], and mechanical backlash [84].

4.2 MIMO Series Elastic Actuator Modelling

As described in Chapter 1 of this thesis, advanced elastic actuators make use of two or more controllable parameters in order to improve performance. To this end, an actuator can be designed to encompass many possible operating modalities through strategic use of the controllable elements [47]. In order to validate the control approach for MIMO-SEAs proposed in this chapter, consider the differentially-clutched SEA introduced in [71], in Chapter 3. The differential gearbox of the actuator was updated to provide access to the spring-side differential body's angular position. This was done to obtain a more accurate measurement of the true spring deflection than from positional inference as done in Chapter 3 (i.e., to measure the angular displacement of the spring shaft θ_s directly instead of inferring $\theta_s = 2\theta_u - \theta_b$). The spring deflection is measured through the difference in encoder measurements between the motor-mounted encoder and the spring-side shaft. An image of the updated device is shown in Fig. 4.1.

To restate the governing equations from Chapter 3, the device dynamics can be summarized by the following set of differential equations [71]:

$$\ddot{\theta}_m = -\frac{k_s}{J_m}\theta_m - \frac{b_m}{J_m}\dot{\theta}_m + \frac{k_s}{J_m}\theta_s + \frac{\tau_{cm}}{J_m} \quad (4.1)$$

$$J_s\ddot{\theta}_s + b_s\dot{\theta}_s + b_d(\dot{\theta}_s - \dot{\theta}_b) + k_s(\theta_s - \theta_m) = \tau_s \quad (4.2)$$

$$J_b\ddot{\theta}_b + b_b\dot{\theta}_b + b_d(\dot{\theta}_b - \dot{\theta}_s) + \tau_{cb} = \tau_b \quad (4.3)$$

$$J_u\ddot{\theta}_u + b_u\dot{\theta}_u + k_u\theta_u = \tau_u \quad (4.4)$$

and for an open differential layout where torque is split evenly between the planetary gears, the following governing equations hold:

$$\frac{\tau_u}{2} = \tau_b = \tau_s \quad (4.5)$$

$$\theta_u = \frac{\theta_b + \theta_s}{2} \quad (4.6)$$

by combining Equations (4.2), (4.4), (4.5), and (4.6), as well as Equations (4.3), (4.4), (4.5), and (4.6), the following two differential equations are obtained:

$$\ddot{\theta}_b = \frac{J_u\ddot{\theta}_s + (4b_d + b_u)\dot{\theta}_s + k_u\theta_s - (4b_d + 4b_b - b_u)\dot{\theta}_b + k_u\theta_b - 4\tau_{cb}}{4J_b - J_u} \quad (4.7)$$

$$\ddot{\theta}_s = \frac{J_u\ddot{\theta}_b + (4b_d + b_u)\dot{\theta}_b + k_u\theta_b - (4b_d + 4b_b - b_u)\dot{\theta}_s + (k_u + 4k_s)\theta_s - 4k_s\theta_m}{4J_s - J_u} \quad (4.8)$$

Substituting Equation (4.8) into Equation (4.7) obtains:

$$\begin{aligned} \ddot{\theta}_b = & \frac{J_u k_s}{J} \theta_m + \frac{J_s k_u}{J} \theta_b + \frac{J_u(2b_d + b_b) - J_s(4b_d + 4b_b - b_u)}{J} \dot{\theta}_b + \frac{J_s k_u - J_u k_s}{J} \theta_s \\ & + \frac{J_s(4b_d + b_u) - J_u(b_s + 2b_d)}{J} \dot{\theta}_s + \frac{J_u - 4J_s}{J} \tau_{cb} \end{aligned} \quad (4.9)$$

where $J = 4J_s J_b - J_u J_s - J_u J_b$. Similarly, by inserting Equation (4.7) into Equation (4.8) obtains:

$$\begin{aligned} \ddot{\theta}_s = & \frac{(4J_b - J_u)k_s}{J} \theta_m + \frac{J_b k_u}{J} \theta_b + \frac{J_b(4b_d + b_u) - J_u(2b_d + b_b)}{J} \dot{\theta}_b + \frac{J_b k_u - 4J_b k_s + J_u k_s}{J} \theta_s \\ & + \frac{J_u(b_s + 2b_d) + J_b(b_u - 4b_s - 4b_b)}{J} \dot{\theta}_s - \frac{J_u}{J} \tau_{cb} \end{aligned} \quad (4.10)$$

where τ_{cm} is the motor torque, which can be related to the input motor voltage V_m of the device through $\tau_{cm} = f_m(V_m/R_a)$, where f_m is a potentially nonlinear input relationship, typically represented by $\tau_{cm} = f_m(V_m/R_a) \cong (K_m K_v V_m)/R_a$. K_m is the motor torque constant, K_v is the motor back EMF constant, and R_a is the winding resistance of the motor. The brake torque τ_{cb} can be modelled as $\tau_{cb} = f_b(V_b/R_b)$ where V_b is the voltage input of the brake and R_b is the winding resistance. This function in a natural state is nonlinear due to magnetic hysteresis of the particle brake, however, in this chapter it will be linearly approximated to be proportional to the input current through a gain K_h . The disturbance observer of the controller is able to compensate for the additional nonlinearities introduced by magnetic hysteresis.

Equations (4.1), (4.9), and (4.10) can be used to generate the multi-input state space model of the actuator for a state vector $\Theta = [\theta_m \ \dot{\theta}_m \ \theta_b \ \dot{\theta}_b \ \theta_s \ \dot{\theta}_s]^T$ as:

$$\dot{\Theta} = \mathbf{A}\Theta + \mathbf{B}\mathbf{V} \quad (4.11)$$

where the state input matrices are:

$$\dot{\Theta} = \begin{bmatrix} \dot{\theta}_m & \ddot{\theta}_m & \dot{\theta}_b & \ddot{\theta}_b & \dot{\theta}_s & \ddot{\theta}_s \end{bmatrix}^\top$$

$$\mathbf{A} = \begin{bmatrix} 0 & 1 & 0 & 0 & 0 & 0 \\ -\frac{k_s}{J_m} & -\frac{b_m}{J_m} & 0 & 0 & \frac{k_s}{J_m} & 0 \\ 0 & 0 & 0 & 1 & 0 & 0 \\ \frac{J_u k_s}{J} & 0 & \frac{J_s k_u}{J} & a_{44} & \frac{J_s k_u - J_u k_s}{J} & a_{46} \\ 0 & 0 & 0 & 0 & 0 & 1 \\ \frac{(4J_b - J_u)k_s}{J} & 0 & \frac{J_b k_u}{J} & a_{46} & \frac{J_b k_u - 4J_b k_s + J_u k_s}{J} & a_{66} \end{bmatrix}$$

$$\mathbf{B} = \begin{bmatrix} 0 & \frac{K_m K_v}{J_m R_a} & 0 & 0 & 0 & 0 \\ 0 & 0 & 0 & \frac{K_h (J_u - 4J_s)}{R_b J} & 0 & -\frac{K_h J_u}{R_b J} \end{bmatrix}^\top, \quad \mathbf{V} = \begin{bmatrix} V_m \\ V_b \end{bmatrix}$$

where:

$$a_{44} = \frac{J_u(2b_d + b_b) - J_s(4b_d + 4b_b - b_u)}{J} \quad (4.12)$$

$$a_{46} = \frac{J_s(4b_d + b_u) - J_u(b_s + 2b_d)}{J} \quad (4.13)$$

$$a_{64} = \frac{J_b(4b_d + b_u) - J_u(2b_d + b_b)}{J} \quad (4.14)$$

$$a_{66} = \frac{J_u(b_s + 2b_d) + J_b(b_u - 4b_s - 4b_b)}{J} \quad (4.15)$$

with $\mathbf{V} = [V_m \ V_b]^\top$ as the input vector. When the actuator rotates, the output torque can be calculated based on the relative compression of both sides of the elastic element $\Delta\theta_s$, its stiffness constant $k_s(\Delta\theta_s)$, and all dynamic losses as:

$$\tau_{out} = 2J_s\ddot{\theta}_s + 2b_s\dot{\theta}_s + 2b_d(\dot{\theta}_s - \dot{\theta}_b) + 2k_s(\theta_s - \theta_m) + \frac{J_u}{2}(\ddot{\theta}_s + \ddot{\theta}_b) + \frac{b_u}{2}(\dot{\theta}_s + \dot{\theta}_b) \quad (4.16)$$

By neglecting the minimal inertia in the spring-side and user-side differential bodies, the governing equation for the application of the output torque as a function of the spring constant k_s becomes:

$$\tau_{out} = \left(\frac{b_u}{2} - 2b_d\right)\dot{\theta}_b + \left(\frac{b_u}{2} + 2b_d + 2b_s\right)\dot{\theta}_s - 2k_s\Delta\theta_s \quad (4.17)$$

where $\Delta\theta_s = \theta_m - \theta_s - \hat{\theta}_{bk}$, and $\hat{\theta}_{bk}$ is the backlash angle affecting the spring deflection $\Delta\theta_s$. The estimation of the backlash angle $\hat{\theta}_{bk}$ is described in the next section.

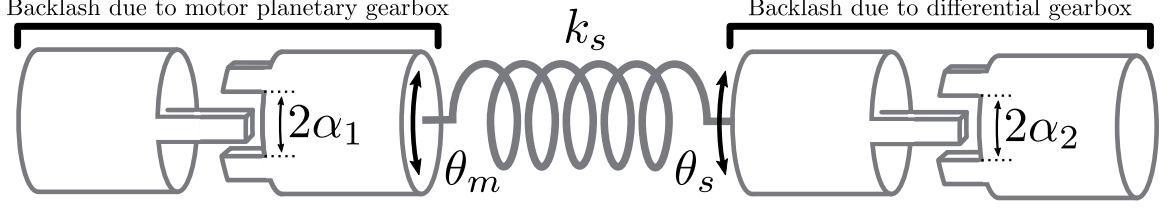


Figure 4.2: Backlash on either side of the elastic element in a SEA. The left side represents backlash due to a planetary gearbox in a traditional DC motor, and the right side represents a secondary gearbox in series with the spring transmission. The backlash angle is: $\hat{\theta}_{bk} \in [-(\alpha_1 + \alpha_2), (\alpha_1 + \alpha_2)]$.

4.3 Backlash Estimation and Compensation

The total measured deflection of the elastic element is composed of two primary components that need to be differentiated from one another. The first is the physical deflection in the spring and the second deals with mechanical backlash, θ_{bk} , which is the positional error due to backlash of the planetary reduction in the motor and the differential gearbox. Thankfully, this can be compensated for based on the actuator dynamic model. This is particularly useful in scenarios in which the nonlinear backlash effect occurs on both sides of the elastic element in the actuator.

Fig. 4.2 demonstrates the possible sources of mechanical backlash on either side of the elastic element. From the figure, the sum of the backlash from either side of the spring can be defined as $\theta_{bk} = 2\alpha_1 + 2\alpha_2$, where α_1 pertains to the backlash between the motor shaft and the output of the planetary gearbox connected to the spring and α_2 represents the backlash in the differential gearbox. The elastic properties of the actuator can be used to provide an insightful estimation of the true deflection of the spring. However, this requires the backlash on either side of the elastic actuator to be measured a priori. If there is compression or expansion in the spring, the elasticity will force the backlash to one of two edges of the transmission system assuming that the spring has a sufficient elastic coefficient, which is generally the case for SEA that deal with power transmission. With this information, estimates can be made on where the true position of the spring shaft is within the range of the backlash. If deflection in the spring occurs, there exists a torque experienced at the output and, therefore, backlash can be estimated using Nordin's exact model [83] as follows:

$$\hat{\theta}_{bk} = \begin{cases} \max\left(0, \dot{\theta}_m - \dot{\theta}_s + \frac{k_s}{b_m}(\theta_m - \theta_s - \theta_{bk})\right) & \text{if } \tau_s < 0 \\ \dot{\theta}_m - \dot{\theta}_s + \frac{k_s}{b_m}(\theta_m - \theta_s - \theta_{bk}) & \text{if } \tau_s = 0 \\ \min\left(0, \dot{\theta}_m - \dot{\theta}_s + \frac{k_s}{b_m}(\theta_m - \theta_s - \theta_{bk})\right) & \text{otherwise} \end{cases} \quad (4.18)$$

where τ_s is the spring torque. Estimating backlash grants a metric to control the torque based on measurements of spring deflection. However, since the deflection angle is used to compute torque, the condition for $\tau_s > 0$ rad is only certain when $\theta_m - \theta_s > \theta_{bk}$, or conversely, $\tau_s < 0 \iff (\theta_m - \theta_s) < \theta_{bk}$. Alternatively, the conditions can be met when the estimated backlash angle has reached the limits $\hat{\theta}_{bk} = -(\alpha_1 + \alpha_2) \implies \tau_s < 0$ or $\hat{\theta}_{bk} = (\alpha_1 + \alpha_2) \implies \tau_s > 0$.

4.4 Multi-Input Active Disturbance Rejection Torque Controller

The objective of ADRC is to provide accurate torque outputs based strictly on measurements of the deflection of the spring. With the estimate of the backlash angle, a reasonable estimate of the true deflection angle can be extracted from the encoder readings on either side of the spring. Backlash can then be compensated for and the updated reference can be used to compute error in the controller. Active disturbance rejection control (ADRC) will be used for this purpose, as ADRC is an error-based control method that can be used to compensate for backlash via a transient profile generator, i.e., a time-optimal solution reference trajectory designed for non-ideal systems. The output of the controller can be distributed to multiple inputs, which is the case for the actuator described by Equation (4.11). Convergence of nonlinear ADRC for multi-input systems is demonstrated in [134].

4.4.1 Reference and Transient Output Torque Profiles

One problem controllers face is related to the transient profile of the reference. From classical control systems, a Heaviside step function is usually implemented as the reference. This introduces issues in controllers that are sensitive to high derivative components, as the Heaviside step has an infinite derivative at the time of the step. However, the step function cannot be physically recreated in any practical system and, therefore, careful consideration of the transient profile should be taken to better represent real systems. In the context of torque control for the elastic actuator, the transient profile is an updated reference that is a function of the proportional and time varying error, a smoothing factor h_0 , and acceleration (aggressiveness) rate r_0 . The discrete values of the proportional τ_{ref} and derivative $\dot{\tau}_{ref}$

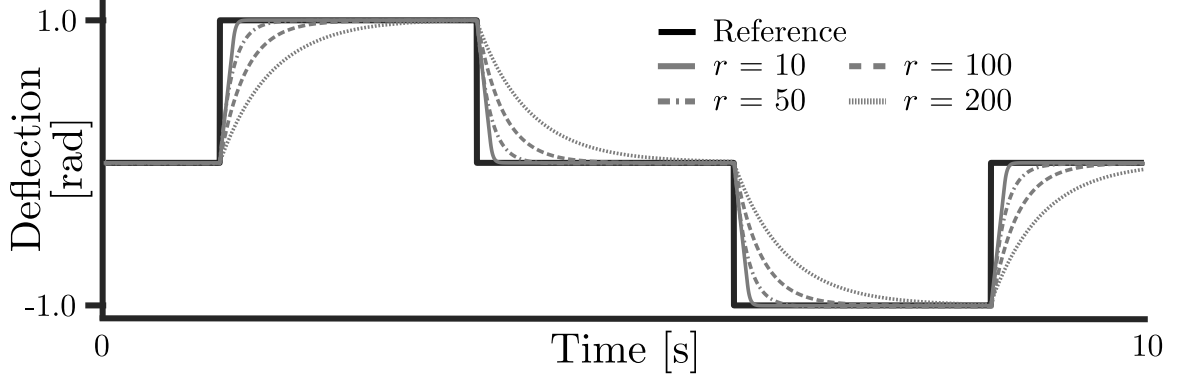


Figure 4.3: Transient profiles generated with various acceleration rates $r = 10, 50, 100, 200$ for a reference deflection signal. The transient profile for desired spring deflection provides an achievable alternative reference signal compared to the infinite derivative reference square profile.

reference trajectory inclusive of the estimated backlash angle $\hat{\theta}_{bk}$ can be calculated as:

$$\tau_{ref}(k) = \tau_{ref}(k-1) + h \dot{\tau}_{ref}(k-1) \quad (4.19)$$

$$\dot{\tau}_{ref}(k) = \dot{\tau}_{ref}(k-1) + h \text{fhan}(\tau_{ref}(k) - \tau_{inf}(k), e_2(k-1), r_0, h_0) \quad (4.20)$$

$$= \dot{\tau}_{ref}(k-1) + h \text{fhan}(\tau_{ref}(k) - k_s(\theta_m(k) - \theta_s(k) - \hat{\theta}_{bk}(k)), e_2(k-1), r_0, h_0) \quad (4.21)$$

where τ_{ref} is the reference torque, $\hat{\tau}_{inf}$ is the observed inferred output torque measured from the deflection of the elastic element, and $\hat{\theta}_{bk}$ is defined in Equation (4.18). k refers to the current measurement in a discrete system and $(k-1)$ refers to the previous sample. Two error variables, denoted $e_1 = \tau_{ref}(k) - \tau_{inf}(k)$ and $e_2 = \dot{\tau}_{ref}(k-1) - \dot{\tau}_{inf}(k-1)$ refer to proportional and time-varying error functions, respectively. These errors can be inserted into the *fhan* function from [135] to produce a *desired transient profile* as shown in Fig. 4.3. The *fhan* function can be described as:

$$\text{fhan}(e_1, e_2, r_0, h_0) = -r_0 \left[\left(\frac{a}{h_0 r_0^2} - \text{sign}(a) \right) s_a + \text{sign}(a) \right] \quad (4.22)$$

where:

$$\begin{aligned}
s_a &= \text{sign}(a + h_0 r_0^2)/2 - \text{sign}(a - h_0 r_0^2)/2 \\
s_y &= \text{sign}(e_1 + h_0 e_2 + h_0 r_0^2) - \text{sign}(e_1 + h_0 e_2 - h_0 r_0^2)/2 \\
a_2 &= h_0 e_2 + \text{sign}(e_1 + h_0 e_2)(a_1 - h_0 r_0^2)/2 \\
a_1 &= \sqrt{h_0 r_0^2 (h_0 r_0^2 + 8|e_1 + h_0 e_2|)} \\
a &= (h_0 e_2 + e_1 + h_0 e_2 - a_2)s_y + a_2
\end{aligned}$$

The above *ghan* function creates a time-optimal approximation used to generate the reference transient profiles demonstrated in Fig. 4.3. The figure demonstrates four transient profiles with differing acceleration rates r_0 to a proposed reference spring deflection. Note that a larger acceleration rate r_0 translates to a more conservative reference profile. The acceleration rate should be chosen based on the dynamics of the plant and the feasible range of the control inputs. For instance, a DC motor with a large inertial load and relatively low input current capabilities would have difficulty following the reference $r_0 = 10$ from Fig. 4.3. Therefore, the profile generated by $r_0 = 100$ might be a more realistic and achievable reference by the plant, minimizing total tracking error. The *ghan* function also contains a precision coefficient h_0 , which is a tunable parameter closely related to the sampling period of the controller. In summary, the reference functions obtained from *ghan* produce a realistic alternative to transients in physical systems, as an input reference such as a Heaviside step function has an infinite derivative at the transient point which is impossible to recreate.

4.4.2 Nonlinear Weighted Feedback Combiner

In addition to the transient profile generator, the nonlinear feedback combiner provides a means of determining the contribution of a proportional and time-varying error in the generation of the control input. Fig. 4.4 demonstrates how the true reference is reformed into a proportional and time-varying reference through the transient profile generator. The proportional and time-varying error are then calculated by subtracting the observed output state and its derivative. The result is then passed through the feedback combiner, which operates on these error functions. The nonlinear feedback combiner can take many forms. In fact, if proportional gains are chosen (linear feedback combination), the result is an observed PD controller:

$$u_p = k_1(\tau_{ref} - \hat{\tau}_{inf}) + k_2(\dot{\tau}_{ref} - \dot{\hat{\tau}}_{inf}) \quad (4.23)$$

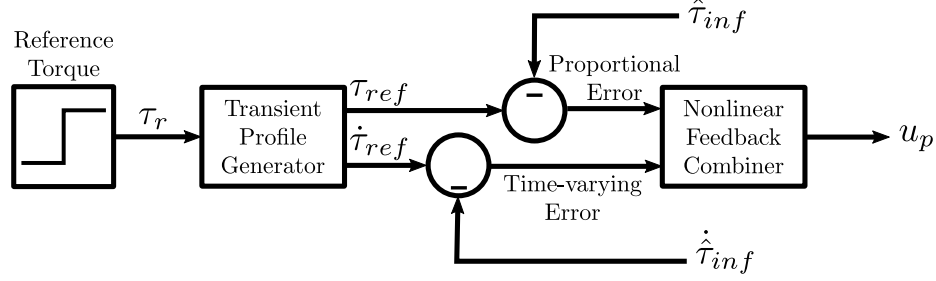


Figure 4.4: Nonlinear weighted feedback combiner layout. The feedback combiner takes into consideration the proportional and time-varying error functions between the transient profile generator and the observed states and proposes a control input u_p .

where u_p is the proposed control input and k_1 and k_2 are the proportional and derivative control gains, respectively. Potential nonlinear operators are suggested by Han in [135], where the proposed control input could be:

$$u_p = k_1 \text{fal}(\tau_{ref} - \hat{\tau}_{inf}, \gamma_1, h) + k_2 \text{fal}(\dot{\tau}_{ref} - \dot{\hat{\tau}}_{inf}, \gamma_2, h) \quad (4.24)$$

where $0 < \gamma_1 < 1 < \gamma_2$ are tuning parameters and the *fal* function is a nonlinear function designed to improve convergence time. The *fal* function defined in [135] is as follows:

$$\text{fal}(e, \gamma, h) = \begin{cases} \frac{e}{h^{1-\gamma}}, & |e| \leq h \\ |e|^\gamma \text{sign}(e), & |e| \geq h \end{cases} \quad (4.25)$$

The goal of the nonlinear feedback combiner is to converge at a faster rate than a PID controller. It is similar to producing time-varying PD gain. Since a static proportional and derivative gain can guarantee convergence for a reasonable range [136], tuning the values of γ_1 and γ_2 can maintain this guarantee with the advantage of faster convergence times.

4.4.3 Extended State Disturbance Observer

Consider the MISO time varying system described in Section 4.2 with six measured states variables defined by the vector $\Theta \in \mathbb{R}^{6 \times 1}$, $i = 1, 2, 3$ as $\Theta = [x_1^1 \ x_2^1 \ x_1^2 \ x_2^2 \ x_1^3 \ x_2^3]^T = [\theta_m \ \dot{\theta}_m \ \theta_s \ \dot{\theta}_s \ \theta_b \ \dot{\theta}_b]^T$. A block diagram of a simplified controller with a single extended state disturbance observer is shown in Fig. 4.5. For the DC-SEA, a system with three independent states θ_m , θ_s , and θ_b as well as their first time derivatives are measurable. Therefore, a total of three system equations for the ADR controller can be utilized. Each of the three second-order subsystems from Equations (4.1), (4.9), and (4.10), i.e., ($i = 1, 2, 3$), and their respective nonlinearities can be described using the following set of equations

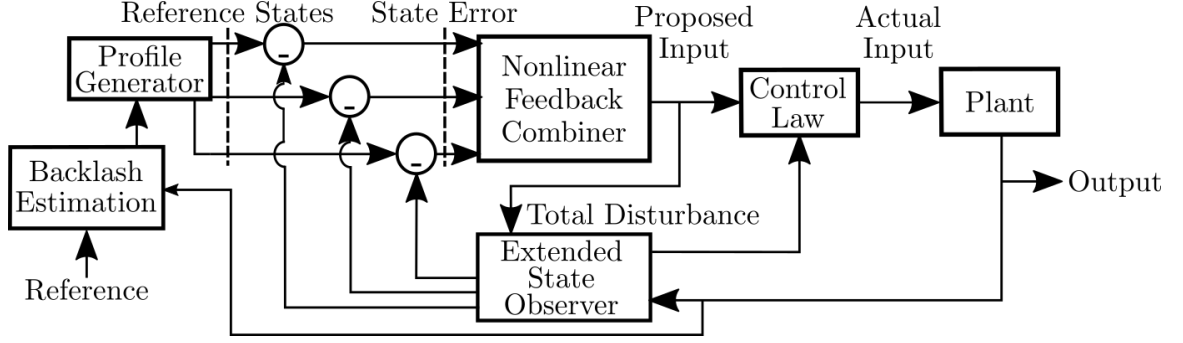


Figure 4.5: Block diagram of a simplified version of the controller. The profile generator adjusts the input at unrealistic instantaneous reference shifting to improve differential tracking error; the nonlinear feedback combiner aggregates the proportional and differential error in the states and proposes an input to the plant. The extended state observer provides a means of estimating and compensating unmodeled disturbances by creating a new state that encapsulates all disturbances in the system.

based on [137]:

$$\begin{cases} \dot{x}_1^i = f_1^i(t, x_1^1, x_2^1, x_1^2, x_2^2, x_1^3, x_2^3, D^i(t)) \\ \dot{x}_2^i = f_2^i(t, x_1^1, x_2^1, x_1^2, x_2^2, x_1^3, x_2^3, D^i(t)) + b^i(t, x_1^1, x_2^1, x_1^2, x_2^2, x_1^3, x_2^3)u \\ y^i = x_1^i \end{cases} \quad (4.26)$$

where f_1^i, f_2^i , and b are imperfect or nonlinear functions describing the subsystem and any external disturbances $D(t)$ experienced by the subsystem, $u^i(t)$ is the control input of the subsystem, and $y^i(t)$ is the output, an angular displacement for the multi-input plant described in Section 4.2. The two local total disturbance terms can be estimated and combined by equating $\bar{x}_1^i = y^i$ and $\bar{x}_2^i = f_1^i(t, x_1^1, x_2^1, x_1^2, x_2^2, x_1^3, x_2^3, D^i(t))$, which provides the following generalized description of the subsystem:

$$\begin{cases} \dot{\bar{x}}_1^i = \bar{x}_2^i \\ \dot{\bar{x}}_2^i = \frac{\partial \bar{x}_2^i}{\partial t} + \frac{\partial \bar{x}_2^i}{\partial x_1^1} \frac{\partial x_1^1}{\partial t} + \frac{\partial \bar{x}_2^i}{\partial x_2^1} \frac{\partial x_2^1}{\partial t} + \frac{\partial \bar{x}_2^i}{\partial x_1^2} \frac{\partial x_1^2}{\partial t} + \frac{\partial \bar{x}_2^i}{\partial x_2^2} \frac{\partial x_2^2}{\partial t} + \frac{\partial \bar{x}_2^i}{\partial x_1^3} \frac{\partial x_1^3}{\partial t} + \frac{\partial \bar{x}_2^i}{\partial x_2^3} \frac{\partial x_2^3}{\partial t} + \frac{\partial \bar{x}_2^i}{\partial D^i} \frac{\partial D^i}{\partial t} \\ \quad - \frac{\partial \bar{x}_2^i}{\partial x_2^i} \frac{\partial x_2^i}{\partial t} + \frac{\partial \bar{x}_2^i}{\partial x_2^i} f_2^i(t, x_1^1, x_2^1, x_1^2, x_2^2, x_1^3, x_2^3, D^i(t)) + \frac{\partial \bar{x}_2^i}{\partial x_2^i} b^i(t, x_1^1, x_2^1, x_1^2, x_2^2, x_1^3, x_2^3)u^i(t) \\ y^i = \bar{x}_1^i \end{cases} \quad (4.27)$$

A linear approximation $\bar{b}^i(t)$ for the nonlinear term b^i allows the subsystem to be extended by a new state representing the sum of disturbance as \bar{x}_3^i . This disturbance and its unknown

first time-derivative $\dot{\bar{x}}_3^i$ are defined by:

$$\begin{cases} \dot{\bar{x}}_2^i = \bar{x}_3^i + \bar{b}^i(t)u^i(t) \\ \dot{\bar{x}}_3^i = f_3^i(t, x_1^1, x_2^1, x_1^2, x_2^2, x_1^3, x_2^3) \end{cases} \quad (4.28)$$

where the total disturbance of the subsystem can be combined to produce:

$$\begin{aligned} \dot{\bar{x}}_3^i = & \frac{\partial \bar{x}_2^i}{\partial t} + \frac{\partial \bar{x}_2^i}{\partial x_1^1} \frac{\partial x_1^1}{\partial t} + \frac{\partial \bar{x}_2^i}{\partial x_2^1} \frac{\partial x_2^1}{\partial t} + \frac{\partial \bar{x}_2^i}{\partial x_1^2} \frac{\partial x_1^2}{\partial t} + \frac{\partial \bar{x}_2^i}{\partial x_2^2} \frac{\partial x_2^2}{\partial t} + \frac{\partial \bar{x}_2^i}{\partial x_1^3} \frac{\partial x_1^3}{\partial t} + \frac{\partial \bar{x}_2^i}{\partial x_2^3} \frac{\partial x_2^3}{\partial t} \\ & + \frac{\partial \bar{x}_2^i}{\partial D^i} \frac{\partial D^i}{\partial t} - \frac{\partial \bar{x}_2^i}{\partial x_2^i} \frac{\partial x_2^i}{\partial t} + \frac{\partial \bar{x}_2^i}{\partial x_2^i} f_2^i(t, x_1^1, x_2^1, x_1^2, x_2^2, x_1^3, x_2^3, D^i(t)) \\ & + \left(\frac{\partial \bar{x}_2^i}{\partial x_2^i} b^i(t, x_1^1, x_2^1, x_1^2, x_2^2, x_1^3, x_2^3) - \bar{b}^i(t) \right) u^i(t) \end{aligned} \quad (4.29)$$

The controller utilizes three extended state observers (ESO) to measure the angular displacement and velocity of each of the subsystems. The ESO can be used to evaluate discrepancies in expected values and, therefore, estimate disturbances in each of the subsystems. The state extension of the ESO provides a means of evaluating nonlinearities around the spring deflection, magnetic hysteresis, static friction, and other unmodelled disturbances. Each of the three extended state observers can be defined as:

$$\begin{cases} \dot{\hat{x}}_1^i = \hat{x}_2^i - \beta_{01}^i g_1^i(\theta_m, \theta_b, \theta_s, \theta_{bk}, \hat{y}^i(t)) \\ \dot{\hat{x}}_2^i = \hat{x}_3^i - \beta_{02}^i g_2^i(\theta_m, \theta_b, \theta_s, \theta_{bk}, \hat{y}^i(t)) + \bar{b}^i(t)u \\ \dot{\hat{x}}_3^i = -\beta_{03}^i g_3^i(\theta_m, \theta_b, \theta_s, \theta_{bk}, \hat{y}^i(t)) \\ \hat{y}^i = \hat{x}_1^i \end{cases} \quad (4.30)$$

where β_{0j}^i $j = 1, 2, 3$ are the observer gains for a dual integral plant state i and $g_j(\theta_m, \theta_b, \theta_s, \theta_{bk}, \hat{y}^i(t))$ $j = 1, 2, 3$ are chosen error functions (potentially nonlinear) considering the actuator backlash in Equation (4.18). This allows the ADR control input contribution from each extended state disturbance observer $u^i(t)$ to be written as:

$$u^i(t) = -\frac{\hat{x}_3^i(t) - u_p^i}{\bar{b}^i} \quad (4.31)$$

where u_p^i is the proposed control input from the nonlinear feedback weighted combiner from Equation (4.24). An extension of the set of observers applied to the DC-SEA in this section are included in the Appendix of this thesis.

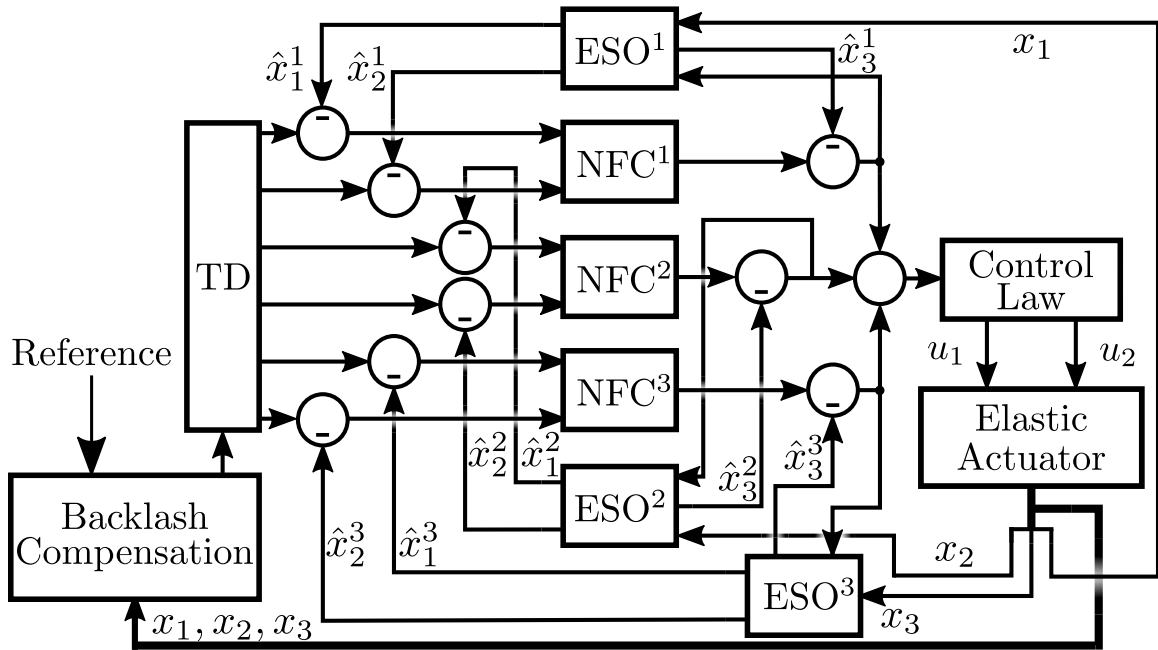


Figure 4.6: Overall updated nonlinear backlash compensated ADRC scheme for a multi-input SEA. Three nonlinear feedback combiners (NFC) and three extended state observers (ESO) are utilized to adapt to perturbations in the spring deflection. The reference is first input into the backlash compensator, where an updated profile is implemented through the transient profile generator. The estimated states from the ESO are then combined into NFC and finally distributed through the control law.

4.4.4 Control Law

There are two primary methods of handling the MIMO system for inferred torque control. The first way of controlling the actuator, similar to a traditional series elastic actuator, is by fully engaging the brake and exclusively using the motor to control the spring deflection. This can reduce the number of controllable inputs to one and, therefore, reduce the number of feasible solutions to obtaining a reference deflection. In this case, the control input is simply:

$$V_m = u_0 = - \frac{fhan(\tau_{ref} - \hat{\tau}_{inf}, c(\dot{\tau}_{ref} - \dot{\hat{\tau}}_{inf}), h_1, r_1) - \hat{x}_3}{\bar{b}} \Bigg|_{\tau_{cb} > \tau_{out} + \tau_s} \quad (4.32)$$

where c is a fine tuning parameter related to the differential error and \hat{x}_3 is the total disturbance estimated by the motor angular position observer. In plants containing multiple inputs working in tandem to achieve a common goal, there exist multiple solutions in the ability to produce a reference torque and, therefore, a multi-input controller must be used.

A second method makes use of both controllable inputs in a distributive manner. Since the contribution of the input can be tuned, the proposed input of the rejection controller can be distributed between the motor voltage V_m and brake voltage V_b . The two control inputs are:

$$u_0 = f_1(k_s \Delta \theta_s) V_m^{max} + f_2(k_s \Delta \theta_s) V_b^{max} \quad (4.33)$$

$$= - \sum_{i=1}^q \frac{p_q^i (fhan(e_1^i, c^i e_2^i, h_1^i, r_1^i) - \hat{x}_3^i)}{\bar{b}^i} \quad (4.34)$$

where e_1^i and e_2^i are the proportional and time-varying error functions, respectively, for each of the three disturbance observers. The proposed input distribution can converge provided that:

$$\forall k_s \Delta \theta_s < \tau_{ref} \exists [f_1(k_s \Delta \theta_s) > 0] \wedge [f_2(k_s \Delta \theta_s) > 0] \ni \Delta \dot{\theta}_s \geq 0 \quad (4.35)$$

and:

$$\begin{aligned} \forall k_s \Delta \theta_s > \tau_{ref} \exists [f_1(k_s \Delta \theta_s) < 0 \wedge f_2(k_s \Delta \theta_s) > 0] \\ \vee [f_1(k_s \Delta \theta_s) = 0 \wedge f_2(k_s \Delta \theta_s) = u_0/V_b] \ni \Delta \dot{\theta}_s \leq 0 \end{aligned} \quad (4.36)$$

with $f_1 \in [-1, 1]$, $f_2 \in [0, 1]$ being linear distributing functions dependent on the current state of the spring deflection and the reference torque. q refers to the number of inputs and i represents the number of outputs from feedback combiners. For the DCSEA, p_q^i , $q = 1, 2$

Table 4.1: Active Disturbance Rejection Tuned Parameters

Gain	T_s	h_0	r_0	c	b_0	β_{01}	β_{02}	β_{03}
Value	0.002	0.002	50	1	0.1	1	167	7813

is a tuning parameter to produce meaningful distribution of the inputs where $q = 1$ relates to motor voltage input and $q = 2$ relates to brake voltage input. An overall diagram of the multi-input controller is displayed in Fig. 4.6. Note the three distinct extended state observers and nonlinear feedback combiners for states θ_m , θ_b , and θ_s .

4.5 Experimental Results

The importance of backlash compensation in elastic actuators becomes more apparent in an experimental setting. Fig. 4.7 compares three controllers when the multi-input actuator behaves as a single-input device. Note that measured deflection in each of the three compared control schemes are similar, however, each produces different torque profiles at the output, rendering different results for the same measured parameters. To this end, the brake is continuously engaged and, therefore, the device acts as a traditional SEA. The evaluated SISO controllers are:

- Single-input controller 1: An active disturbance rejection controller (ADRC) without backlash compensation;
- Single-input controller 2: A backlash-compensated active disturbance rejection controller;
- Single-input controller 3: A proportional-integral-derivative (PID) controller as a basis of comparison.

The tuned parameters for all ADR controllers used are provided in Table 4.1. The actuator was connected to a static load cell and a reference deflection (pseudo-torque control) was controlled in square pulses of ± 1 rad. Fig. 4.7(a) demonstrates the performance of the three controllers to a specified reference deflection.

All three controllers are able to effectively control the measured deflection, however, the torques experienced at the output can vary due to the effects of backlash. If backlash is not considered, which is the case for PID and classical ADRC, raw encoder inputs about the deflection are taken to be the true deflection angle of the spring causing deviations in the expected output torque ($\Delta\theta_s = \theta_m - \theta_s - \theta_{bk}$). With backlash compensation, an updated

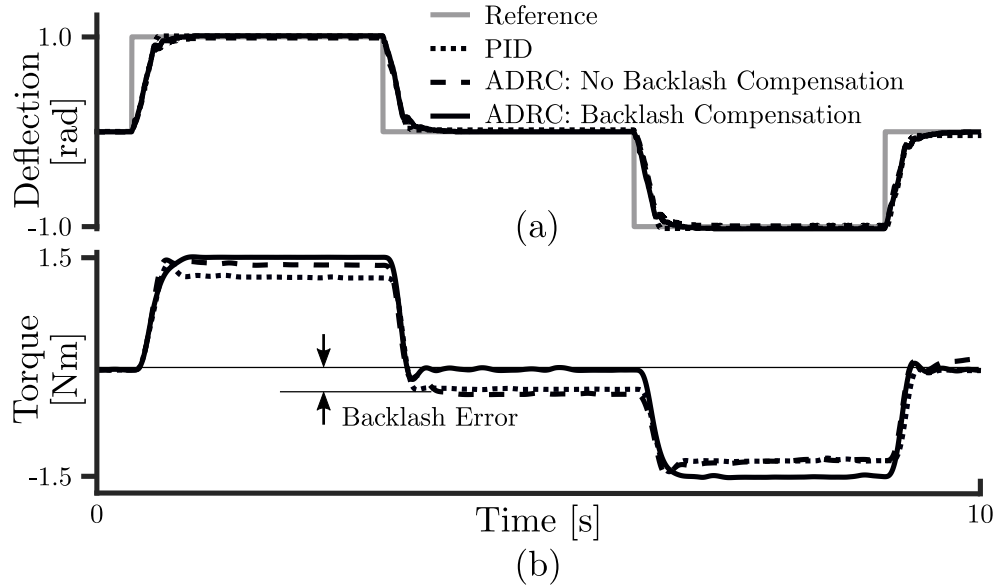


Figure 4.7: Results of single-input deflection control with PID, classical ADRC, and backlash compensated ADRC.

estimation of the true deflection can be inferred through the addition of the estimated backlash angle ($\Delta\theta_s = (\theta_m - \theta_s - \theta_{bk}) + \hat{\theta}_{bk}$).

The next experiments were conducted using the multi-input control law Equation (4.34), separating control effort between the brake and motor. The distributive method was applied providing the following evaluated controllers:

- Multi-input controller 1: An active disturbance rejection controller (ADRC) without backlash compensation;
- Multi-input controller 2: A backlash-compensated active disturbance rejection controller;
- Multi-input controller 3: PID controller single output distributed as $V_b = 0.7u_0$ and $V_m = 0.3u_0$.

Fig. 4.8(a) demonstrates a similar experiment utilizing both inputs of the series elastic actuator. The raw measured deflection of the backlash compensated ADRC does not follow the reference trajectory as closely as the classical controllers to compensate for uncertainties in the actuator backlash. This provides an output torque with better symmetry that is not dependent on the initial conditions (θ_{bk} at $t = 0$). The effects of backlash compensation are most apparent at low torques and in the transition from positive to negative reference deflections. Fig. 4.9(a) demonstrates a scenario in which the desired spring deflection continuously transitions from 1 rad to -1 rad. Similar to previous

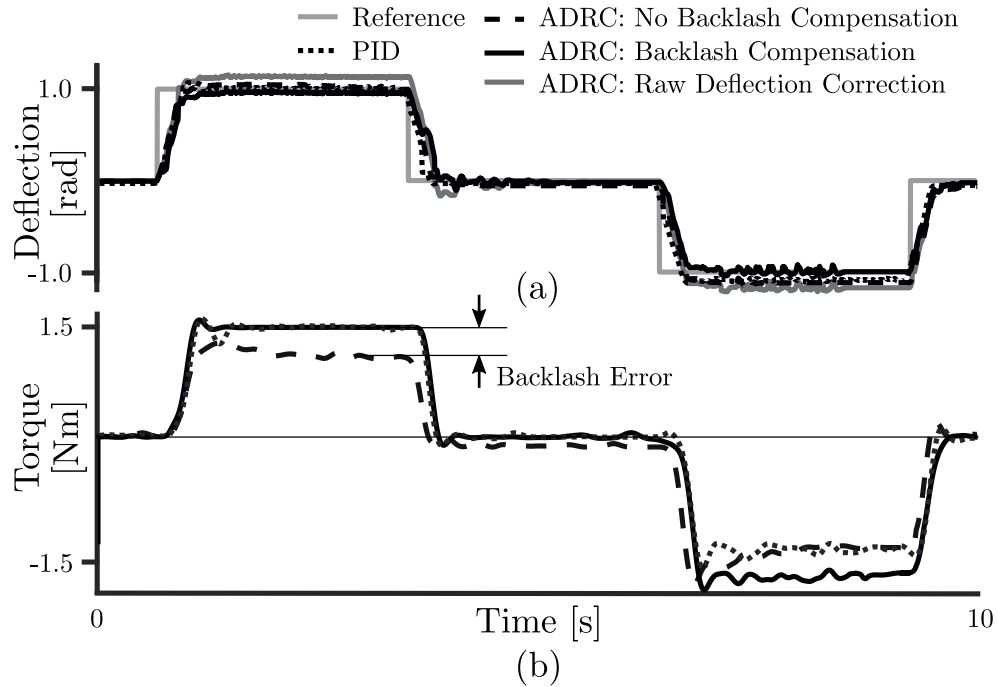


Figure 4.8: Results of multi-input control on the spring deflection to reference square pulses. The backlash compensated ADRC has an updated reference deflection profile to compensate for nonlinearities in the spring.

experiments, each of the three compared controllers were able to maintain the desired deflection, however, only the backlash compensated controller generates an estimate of the backlash angle $\hat{\theta}_{bk}$ as shown in Fig. 4.9(b). Fig. 4.9(c) demonstrates the measured output torque for all three controllers and compares the output torque to an ideal linear spring. As shown, the controllers without backlash compensation were influenced heavily by the nonlinearity in the spring and the zero-torque deadzone caused by actuator backlash. In the controller with backlash compensation, the output torque relates closer to the ideal linear spring and has a minimal deadzone. Total error from an ideal linear proportional output for each controller is displayed in Fig. 4.9(d).

4.6 Conclusions

SEAs encapsulate the ability to effectively infer the output torque in a cost-effective manner and to this end, torque estimation and resolution are important metrics to evaluate the performance. Active disturbance rejection is an attractive control method for elastic actuators as it is able to handle nonlinear effects as well as other unmodelled disturbances. SEAs tend to be largely nonlinear and, therefore, ADRC provides the advantages of using an error-based control method without having a perfect model of the plant.

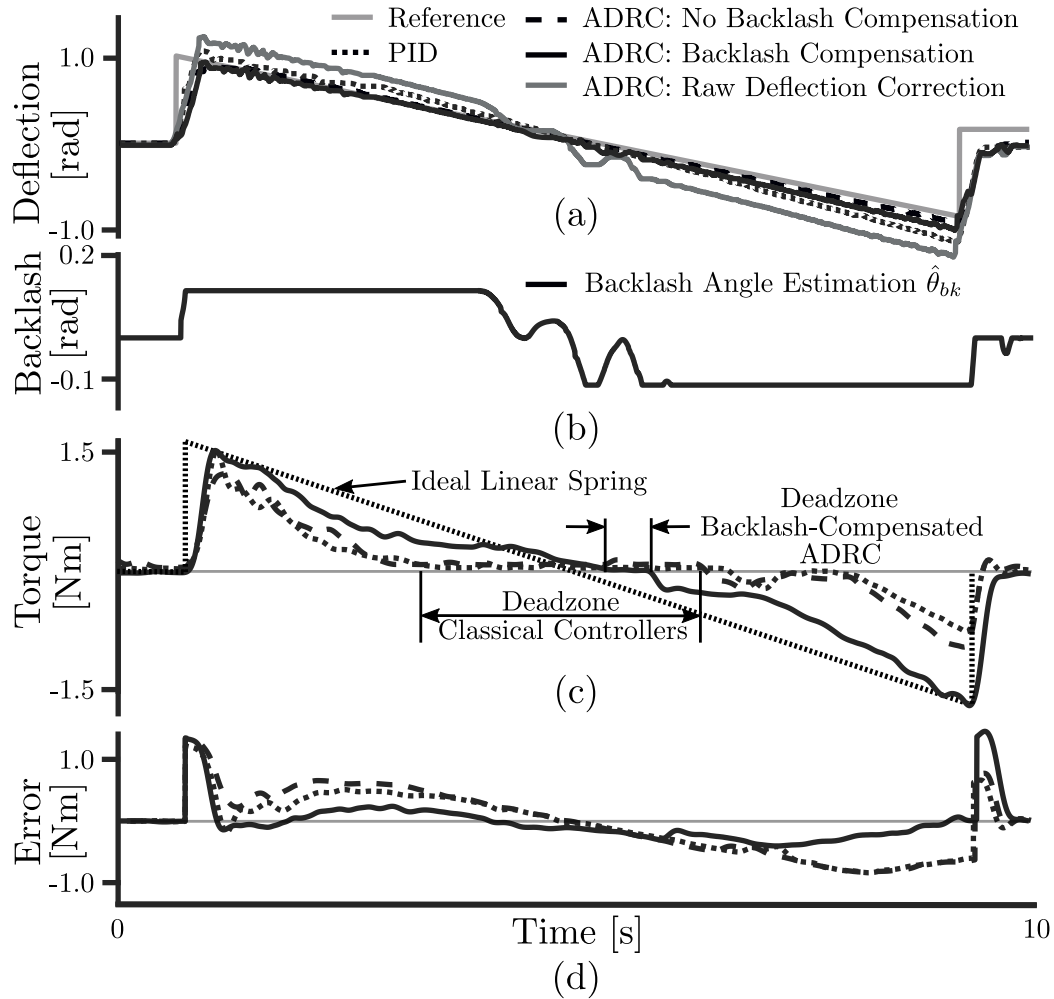


Figure 4.9: Demonstration of nonlinearities in spring through multi-input sawtooth deflection control. (a) shows the deflection control using PID, classical ADRC, as well as backlash-compensated ADRC. The backlash-compensated ADRC demonstrates the corrected true deflection angle ($\theta_m - \theta_s$) as well as the raw measured angle ($\theta_m - \theta_s - \hat{\theta}_{bk}$). (b) shows the estimated backlash angle $\hat{\theta}_{bk}$. (c) Demonstrates the measured output torque compared to an ideal linear spring and a system with no backlash. Zero-torque deadzones are also highlighted as an effect of actuator nonlinearities. (d) shows the error between the measured torques for each controller and an ideal spring.

However, the nonlinearities around deflection of the spring can cause unwanted behavior of the device since spring deflection is often the controlled parameter in elastic actuators. There is no way to determine the exact output torque of series elastic actuators without the use of external sensing devices and, therefore, an ideal elastic actuator would have a linear relationship between the measured/estimated spring deflection and the output torque. To this end, mechanical backlash can have adverse effects on the performance of a series elastic actuator if it is desirable to operate the actuator without a force/torque sensor.

The proposed unified backlash-compensated multi-input active disturbance rejection controller is a robust method to reduce the effect of nonlinearities caused by mechanical backlash and spring deflection on the output torque. The updated reference deflection profile allows the output torque to follow a desired trajectory with less error caused from directional changes or at low torques, improving the overall torque bandwidth of the actuator. Accounting for backlash in the actuator also ensures the true deflection in the spring is as accurate and symmetric as possible. Compensating for this nonlinearity is easily implementable and produced consistent results as compared to classical error-based control methods. Proper deflection control in human-machine interaction is important to maintain safety and minimize uncertainty when a device interacts with an operator, while providing a cost-effective alternative to inferring the output torque experienced by the user. To this end, there are a number of different gains mentioned in this chapter that are able to be tuned to create an optimal controller for the DC-SEA. However, the gains are generally associated with nonlinear functions, where the impact of adjustment of these gains cannot be solved analytically. This is especially true for multi-input actuators, as there are multiple solutions to achieve a common goal. To mitigate this issue, a multiobjective optimization strategy should be implemented to determine a set of gains that produce desirable responses to the actuator. The following chapter introduces a stochastic multiobjective optimizer tailored to solving the issue of robust control of the complex actuator.

Chapter 5

Multi-Objective Controller Optimization

5.1 Introduction

ROBUST controllers are often model-based. This adds an element of complexity to the controller design and requires significantly more background knowledge about a plant to create the model. In many cases creating the model is not feasible or, if time is of the essence, resource consuming. This is where active disturbance rejection flourishes, since ADRC is error based and the exact mathematical model need not be known. ADRC is a viable substitute for PID where a more robust controller is necessary [138–141]. PID controllers have three tuning parameters, each with well defined properties. ADRC, however, can have upwards of eight tuning parameters for each controlled state. Therefore, tuning the controller may be challenging and rely completely on the control objective for a given application.

Single-objective genetic algorithms (GAs) have been used to optimize an ADRC for an unmanned underwater vehicle [142] and for an aircraft [143]. Other optimization strategies, such as particle swarm optimization and their variants, have been used in the design of ADRC force controllers [144], temperature controllers [145], and rocket position controllers [146]. In other applications, ant colony optimization [147] and a chaotic cloud cloning selection algorithm [148] were also used. All of these methods used single objective optimization algorithms to optimize for a single control objective. Optimizing a controller, however, is often not a single objective task. An ADRC gain can result in conflicting performance parameters such as rise time, settling time, overshoot, control effort, and tracking error. In the majority of design problems these objectives need to be considered and balanced.

A better approach to automate the tuning of an ADRC should incorporate a multi-objective optimizer. Standard algorithms used to solve multi-objective problems include nondominated sorting genetic algorithms (NSGA-II) and strength pareto evolutionary algorithms (SPEA2). However, in problems with an increased number of objectives, the performance of these algorithms begins to deteriorate [149, 150]. For this reason, other solvers capable of solving many-objective problems must be used.

The problem encountered by all GA-based solvers can be traced back to the dominance of points in multi-objective problems. A solution that performs better than another in at least one objective is said to be dominant, provided that the solution does not perform worse on any other objective. As the number of objectives increases, the number of non-dominated solutions also increase. That is, each solution becomes uniquely optimal and, therefore, the algorithm cannot progress. With enough objectives, all points in the solution become non-dominated by any other solution. To address this issue, researchers have suggested use of reference point domination [151]. In NSGA-III, reference-point dominance is used to improve the diversity of the solutions along the Pareto front [152]. The algorithm forces the solutions to distribute along the searchspace, which can guarantee that solutions will be found relatively fast [153]. This concept was further developed in [154], where another algorithm, θ -NSGA-III, used the same reference points in NSGA-III to push solutions closer to the Pareto front. This method was then combined with preference incorporation approaches in [155] to create a new algorithm, the RPD-NSGA-II. This algorithm further improved convergence and diversity of the solutions while outperforming both of its predecessors. Since the RPD-NSGA-II algorithm was the most efficient of existing multi-objective solvers, it was selected to tackle the multi-objective problem presented in tuning the variables present in an ADRC in this chapter.

5.2 Reference Point Dominance-Based Nondominated Sorting Genetic Algorithm

Optimization of a high dimensional problem with multiple goals becomes much more complicated than a standard single-objective case. In this regard, it often occurs where intermediate steps to achieve a particular goal contradict one another. Therefore, it is necessary to create a compromise between a problem with two or more objectives. Consider a simplified motor with an inertial load, such as the one shown in Fig. 5.1. A system such as this one can be optimized for a proportional error controller gain k_p around multiple objectives. For the purpose of demonstration, consider two objectives that are not

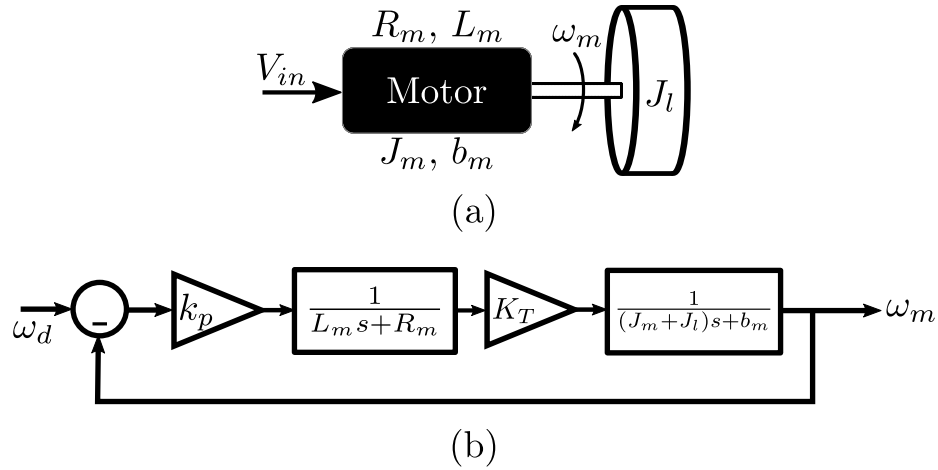


Figure 5.1: Simple motor system with inertial load. (a) is a figure representing the system, and (b) demonstrates the closed loop block diagram with proportional speed control gain k_p .

independent of one another: the minimization of control effort and rise time. In this case, rise time is a direct function of control effort and a larger control effort (applied voltage) would cause the system to achieve a larger magnitude of acceleration. If the control effort is to be minimized, the system would experience minimal acceleration and, therefore, have an extended rise time. Since the two objectives are in opposition, there might not be a single solution to determine the best outcome of the system. In fact, a set of optimal solutions create a *pareto front*. That is, a set of solutions that are not dominated by any other solution. Fig. 5.2 demonstrates this phenomenon, where the solutions connected with a dotted line represent the location of entirely nondominated solutions (pareto front). The dominated solutions in the figure have one or more solutions with a more optimal value for at least one of the objectives. This is represented in the figure by shaded regions, where the dominating solution lies on the bottom left corner of the regions and any other solution that is within this region is, therefore, dominated for the dual minimization objectives. In problems with multiple objectives, issues may arise around the diversity of solutions around complex pareto fronts [156, 157].

5.2.1 Convergence and Diversity

In multi-objective optimization, the goal is to obtain a set of potential solutions with satisfactory performance on all fronts. After the optimization process has run its course, the solution is chosen based on what the designer decides are the most important objectives. If there is significant emphasis on specific objectives, an aggregation method could be implemented a priori and bias solutions closer to the emphasized objective. However, for

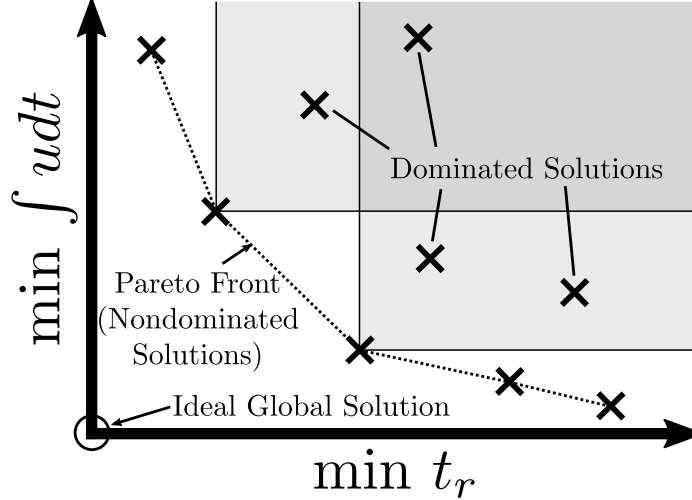


Figure 5.2: Pareto front definition

complex systems it can be hard to distinguish which objectives are the most significant and putting too much emphasis on specific objectives can have adverse effects on the quality of solutions after the optimizer has terminated. The evaluated RPD-NSGA-II algorithm from [155] aims to address this issue by placing emphasis on the diversity of the population in the evolutionary algorithm. The goal of the RPD-NSGA-II is to have a combination of convergence and diversity, which are not independent of one another. The stochastic nature of evolutionary algorithms helps improve diversity in search for optimal solutions, the non-RPD-dominated sorting and selection of the multiple pareto fronts allows for convergence around the objectives.

5.2.2 Reference Points and Distance Measures

The diversity guarantee of the RPD-NSGA-II algorithm is attributed to the reference points generated at the beginning of the process. The reference points are generated using a method proposed in [158], where a set of evenly distributed points on a normalized hyperplane as shown in Fig. 5.3(a). Once the values of fitness for each objective are obtained, each range of fitness values are normalized by the maximum and minimum values, obtaining the solution set as marked by the green points in Fig. 5.3(b). The potential solutions are then associated with the nearest reference point vector from the ideal point (origin for minimization problems) along the normalized hyperplane. Consider the set of solutions in Fig. 5.3(b) that are nearing the plane $f_2 = 0$. A two-dimensional visualization is displayed in Fig. 5.3(c), where each of the solutions are attributed to a reference point. In this example, solution a is associated with reference point r_2 and solutions b and c are

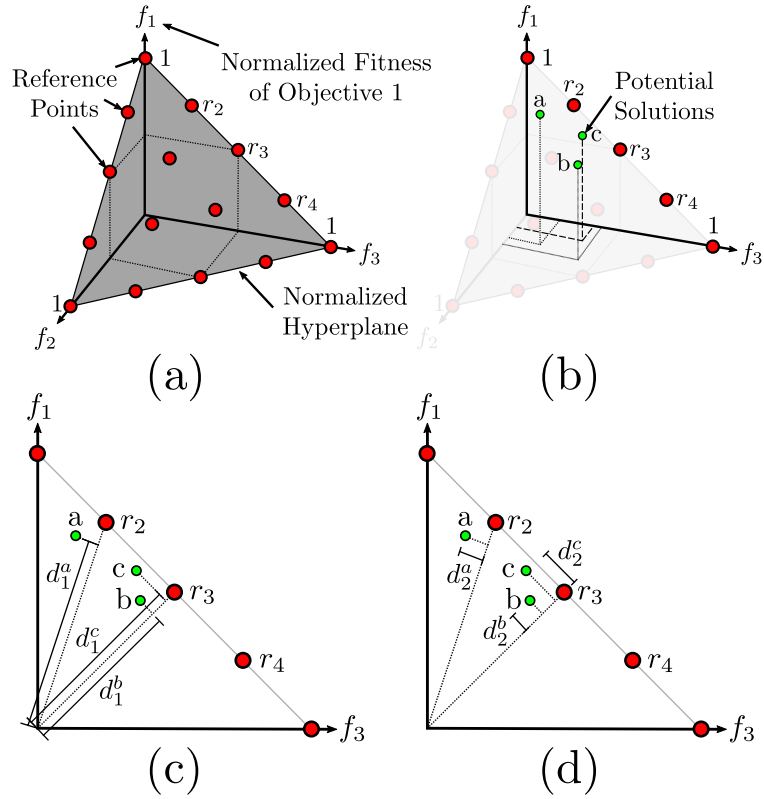


Figure 5.3: RPD-NSGA-II reference points and distance measures

associated with reference point r_3 . Once all of the solutions have been associated with their respective closest reference point, each solution is assigned two distance measures, d_1 and d_2 , used to aid in the non-RPD-dominated sorting process. Distance measure d_1 refers to the magnitude of the distance between the origin (for minimization problems) and the normal drawn from the reference vector to the potential solution, as in Fig. 5.3(c). This distance relates to convergence of the solutions, as a smaller magnitude of d_1 means better overall fitness of a solution. Distance measure d_2 refers to the magnitude of the normal as in Fig. 5.3(d). This distance is used to help encourage diversity in the selection process for the next generation, as reference points with solution crowding will begin to reduce emphasis on some of the solutions to favour diversity.

5.2.3 RP-Dominance and Non-RPD-Dominated Sorting

The two distance measurements are used to evaluate a solution's dominance over other solutions, therefore, generating an alternative to determining pareto fronts apart from pareto-dominance. A potential solution $\mathbf{x}_1 = [x_1, x_2, \dots, x_m]$ with the multi-objective fitness value taking the form $\mathbf{F}(\mathbf{x}_1) = [f_1(\mathbf{x}_1), f_2(\mathbf{x}_1), \dots, f_n(\mathbf{x}_1)]$ is said to pareto dominate another

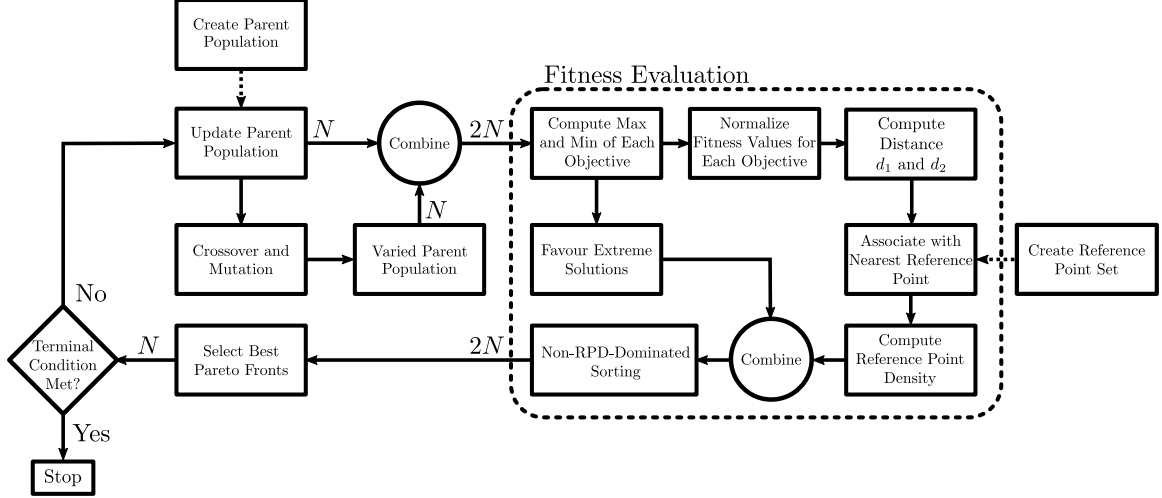


Figure 5.4: RPD-NSGA-II Algorithm

solution $\mathbf{x}_2 = [x_1, x_2, \dots, x_m]$ | $\mathbf{F}(\mathbf{x}_2) = [f_1(\mathbf{x}_2), f_2(\mathbf{x}_2), \dots, f_n(\mathbf{x}_2)]$ if $f_j(\mathbf{x}_1) \leq f_j(\mathbf{x}_2) \forall j = 1, 2, \dots, n$ and for at least one $j = 1, 2, \dots, n$, | $f_j(\mathbf{x}_1) < f_j(\mathbf{x}_2)$. For the RPD-NSGA-II algorithm, dominance of a solution over another is taken a step further. A solution \mathbf{x}_1 is said to RP-dominate another solution \mathbf{x}_2 if \mathbf{x}_1 pareto dominates \mathbf{x}_2 or if \mathbf{x}_1 and \mathbf{x}_2 are pareto equivalent and any of the following are true [155]:

- Both solutions are associated with the same reference point, but the value of d_1 for \mathbf{x}_1 is less than the value of d_1 for \mathbf{x}_2 ; or
- Both solutions are associated with different reference points, but the value of d_1 for \mathbf{x}_1 is less than the value of d_1 for \mathbf{x}_2 and there are less solutions associated with the same reference point as \mathbf{x}_1 than that of \mathbf{x}_2 . This operation is known as computing the reference point density.

Therefore, the entire population can be evaluated and placed into various dominating ranks. The ranks are an extension of pareto-dominance, with emphasis on diversity due to the second condition above. This methodology is referred to as non-RPD-dominated sorting [155]. Once the entire population has been sorted, the top 50% of solutions among the best performing RP-dominated pareto fronts progress to the next generation of the optimization loop as the parent population. If the termination condition of the optimization process is not achieved, the newly recreated parent population is varied using standard stochastic genetic algorithm operators (crossover and mutation) and is re-evaluated for its fitness and distance measures. The total algorithm with all components is displayed in Fig. 5.4.

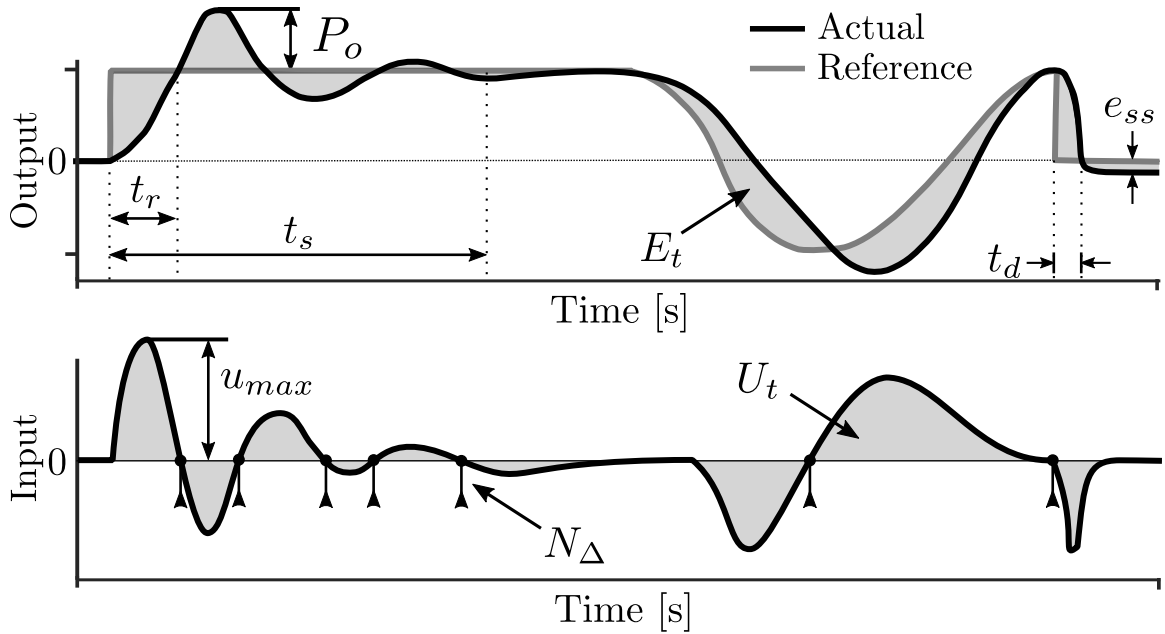


Figure 5.5: The top figure demonstrates the response of a system $f(t)$ to a reference $r(t)$. The bottom figure represents the control output $u(t)$ for this device. The figure demonstrates common controller objectives such as tracking error E_t , control effort U_t , percent overshoot P_o , rise time t_r , settling time t_s , maximum input U_{max} , steady-state error e_{ss} , disengagement time t_d , and number of input direction changes N_{Δ} .

5.3 Performance Objectives for ADRC

In the context of control, there are a number of competing objectives for any given problem. Depending on the design, the plant, and other physical limitations of controller implementation, the most optimal solution for a given problem may not be immediately obvious. In most applications, there are many parameters that hold significant weight over others and conditions that must be taken into consideration. The optimized objectives in this chapter pertain to the following:

1. **Tracking Error (E_t):** Refers to the integral of the error over all time. This is displayed as the sum of the shaded region in Fig. 5.5. Ideally, $E_t = 0$, which refers to perfect tracking between the reference $r(t)$ and the actual output $f(t)$. i.e.,

$$E_t = \int_0^t |\text{reference} - \text{actual}| dt = \int_0^t |r(t) - f(t)| dt \quad (5.1)$$

2. **Control Effort (U_t):** Refers to the integral of the controller output $u(t)$ over all time. U_t relates to the efficiency of a system, which is particularly useful in continuous or

high power applications. U_t is defined as:

$$U_t = \int_0^t |u(t)| dt \quad (5.2)$$

3. **Percent Overshoot (P_o):** Refers to the percentage of the maximum output value that exceeds the reference. This is particularly useful in applications where the output $f(t)$ is nearing rated hardware limits, or where the output has nonlinear components. P_o is defined as:

$$P_o = \frac{\max f(t) - r(t)}{r(t)} \times 100\% \quad (5.3)$$

4. **Rise Time (t_r):** Rise time refers to the time it takes for the system to reach a value that is 95% of the reference value from the time of transience. This is useful for high speed switching applications. t_r is defined by:

$$t_r = \min(t) \mid f(t) \geq 0.95 \times r(t) \quad (5.4)$$

5. **Settling Time (t_s):** Refers to the time it takes for the system to permanently settle within $\pm 5\%$ of the reference value measured from the time of transience. The settling time t_s is defined as:

$$t_s = \max(t) \text{ where } |(f(t) - r(t))| \geq 0.05 * r(t) \quad (5.5)$$

6. **Maximum Input (u_{max}):** Refers to the maximum value of the controller output during the entire control process. This objective is useful in applications where the source is limited, nearing saturation, or there are tight tolerances around the applied input to the plant. u_{max} is defined as:

$$u_{max} = \max(u(t)) \quad (5.6)$$

7. **Steady-State Error (e_{ss}):** Steady-state error refers to the resulting error between the final value of the reference and the settled output state when $t \rightarrow \infty$ in reference trajectories with a finite number of transient events. This is particularly useful in high precision applications where there are tight tolerances on the final state of the output. The steady-state error e_{ss} is defined as:

$$e_{ss} = r(\infty) - f(\infty) \quad (5.7)$$

8. **Disengagement Time** (t_d): Disengagement time is the time it takes a system to release energy or reverse back to an initial state. It is measured from the time disengagement is initiated, t_{oi} , to the time when the system is within 5% of the reference value at the time disengagement was initiated. This is important in applications regarding physical interaction with humans, as a source of collision mitigation. t_d is defined as:

$$t_d = \min(t) \mid f(t) \leq 0.05 \times r(t_{oi}) \quad (5.8)$$

9. **Number of Input Direction Changes** N_Δ : Refers to the number of instances the control effort changes direction throughout the simulation. High switching applications become difficult to physically implement and can damage sensitive plants. N_Δ is defined as:

$$N_\Delta = \sum \left| \frac{\text{sign}(u(t)) - \text{sign}(u(t-1))}{2} \right| \quad (5.9)$$

Each of the above objectives are minimization functions, where the minimum value of each objective translates to better performance. A graphical representation of each of the above objective functions are displayed in Fig. 5.5.

5.3.1 ADRC Tunable Parameters

Due to the large number of tunable parameters in the disturbance rejection controller, it becomes difficult to evaluate the contribution of each parameter on the performance of the device. The number of parameters to be optimized depends on the order and dimension of the problem. For each independent variable (inclusive of all time derivatives), there is one observer to estimate the states and one total disturbance term for the subsystem. The extended state observer for an n -th order plant (or subsystem) can be represented as follows:

$$\begin{cases} \hat{\dot{x}}_1 = \hat{x}_2 - \beta_{01}g_1(x_1 - \hat{y}(t)) \\ \hat{\dot{x}}_2 = \hat{x}_3 - \beta_{02}g_2(x_1 - \hat{y}(t)) \\ \vdots \\ \hat{\dot{x}}_n = \hat{x}_{n+1} - \beta_{0(n)}g_n(x_1 - \hat{y}(t)) + \bar{b}(t)u \\ \hat{\dot{x}}_{n+1} = -\beta_{0(n+1)}g_{n+1}(x_1 - \hat{y}(t)) \\ \hat{y} = \hat{x}_1 \end{cases} \quad (5.10)$$

This system has $(n + 1)$ proportional observer gains $\beta_{0(1,2,..(n+1))}$ and depending on the function $g_{1,2,..,(n+1)}$, potentially more. Han proposed using nonlinear *fal* functions for the observer error functions [135], each of which is defined by Equation (4.25) and have a tuning parameter of their own, that is γ . The proposed method suggests using n nonlinear functions per observer. Therefore, the total number of tuning parameters *per* observer is $(2n)$ for nonlinear extended state observers and $(n + 1)$ for linear extended state observers.

Similarly, there are a varying number of tunable parameters dependent on the type of feedback combiner chosen and the number of unique states. For example, a simple linear proportional-derivative controller has n gains for an n -th order plant. That means, for a second-order plant there are two gains, usually denoted k_p and k_d . If the nonlinear feedback combiner is chosen to be a weighted *fal* function as in Equation (4.24), the number of tunable parameters *per* feedback combiner is $(2n)$. The total dimension is multiplied by the number of extended state observers n_{obs} .

For MIMO systems, from Equation (4.34), there are an additional number of tunable gains equal to the number of inputs multiplied by the number of extended observers $n_{in} \times n_{obs}$. Multi-input systems also have multiple transient profile generators similar to the profile generator in Section 4.4.1. Each *fhan* function, defined by Equation (4.22) in the transient profile generator has two controllable parameters, r_0 and h_0 . Therefore, the number of tunable parameters from the transient profile generators is twice the number of extended observers $2n_{obs}$. The total number of tunable gains are is displayed by Table 5.1, where the definitions of each of the tunable gain is defined in the Appendix of this thesis.

Table 5.1: Number of Optimizable Gains in an ADRC

		Feedback Combiner		
		PD	<i>fal</i>	<i>fhan</i>
ESO	Linear	$n_{obs}(n_{in} + 2n + 3)$	$n_{obs}(n_{in} + 3n + 3)$	$n_{obs}(n_{in} + n + 6)$
	Nonlinear	$n_{obs}(n_{in} + 3n + 2)$	$n_{obs}(n_{in} + 4n + 2)$	$n_{obs}(n_{in} + 2n + 5)$

5.4 Optimizer Validation

Before diving into a difficult multi-input, high dimensional problem, a simplified plant was used to evaluate the validity of the optimizer. The plant is a classical inverted pendulum on a cart. A simplified drawing of the system is shown in Fig. 5.6. For the inverted pendulum plant there are two extended state observers $n_{obs} = 2$: one that monitors the position of the cart and the other that monitors the angular position of the pendulum. Each linear extended state observer has three observer gains, β_{01} , β_{02} , and β_{03} , and

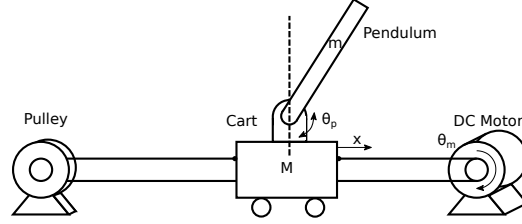


Figure 5.6: Simplified setup of an inverted pendulum on a cart.

Table 5.2: Optimizer Boundary Conditions

Variable	Range
Aggr. Control Loop	$1 \times 10^{-5} < h_{1p}, h_{1c} < 1 \times 10^{-1}$
Acceleration Limit	$1 \times 10^{-3} < r_p, r_c < 1 \times 10^2$
Damping Coefficient	$0.5 < c_p, c_c < 1.5$
Observer Gains	$0.5 < \beta_{01p}, \beta_{01c} < 2$
	$1 \times 10^{-8} < \beta_{0(2,3)p}, \beta_{0(2,3)c} < 1 \times 10^{-3}$

used nonlinear error feedback combiners, fal , each containing an acceleration limit of the tracking differentiator, r_1 , and the damping coefficient, c_1 . Lastly, h_{1p} and h_{1c} are parameters for the pendulum and cart, respectively, that determine the aggressiveness of their control loops [135]. The ranges for the variables was determined by centralizing the gains within a range commonly used throughout the literature. Based on the suggested estimates of the gains, the ranges were provided such that the search space would be large without compromising the basis of operation for the extended state observers and the nonlinear time-optimal tracking functions. As previously discussed, the gains will be adjusted to optimize performance for several objectives, namely: tracking error of the cart, tracking error of the pendulum, controller effort, rise time, percent overshoot, settling time, and steady-state error as shown in Fig. 5.5. Repeated sampling was performed to account for the stochastic nature of the algorithm. Each sample was performed with 1,000 generations. The crossover and mutation variation parameters were set to 20, as per recommendations from [159]. Boundary conditions were applied to the parameters to prevent infeasible solutions. The conditions are presented in Table 5.2. Taking all of the total controller tunable parameters into consideration, the gains that are to be optimized for the inverted pendulum are the observer gains β_{0i} , $i = 1, 2, 3$ and the discrete feedback combiner gains c , h , and r . Throughout the literature on active disturbance rejection control, the choices of the aforementioned gains are more subjective than analytical. The proposed gains from [135] are at most a good starting point for an optimization process.

In order to simulate a rather challenging environment, the inverted pendulum was

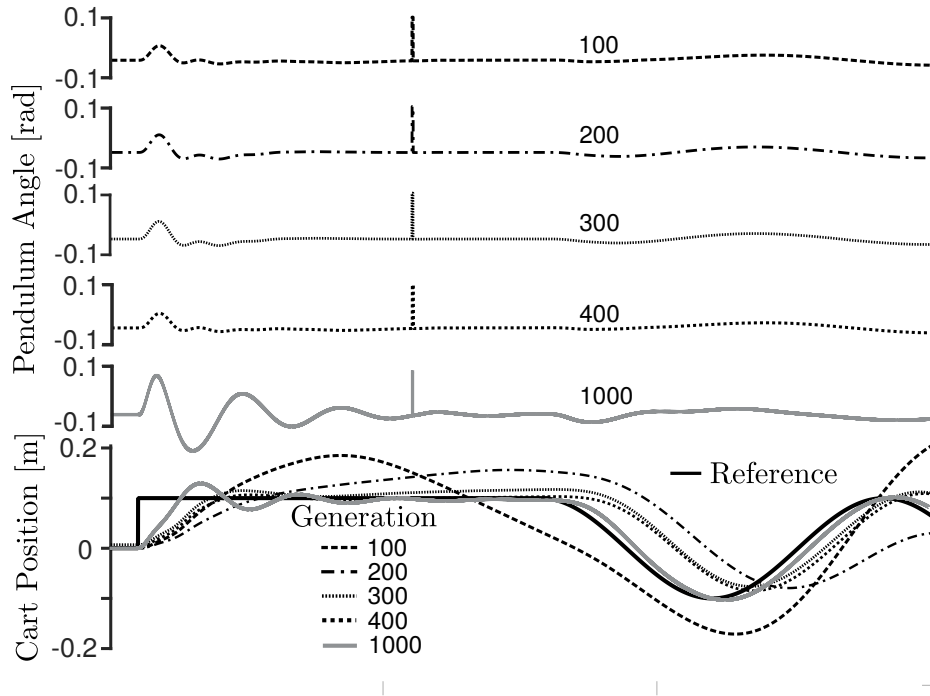


Figure 5.7: Simulated optimization results with emphasis on tracking error

commanded to respond to a change in desired cart position, starting with a step input from 0 m to 0.1 m, and then following a sine wave with angular frequency 1 rad/s as $0.1 \sin(t)$. Apart from the change in cart position, a disturbance was added to the system to try and bring the pendulum out of equilibrium. An impulse of 0.087 radians ($\approx 5^\circ$) applied to the pendulum angle was introduced to the system at 5.5 seconds to show that the rejection controller is able to handle this disturbance. As discussed in the introduction, the optimizer used for this task is the RPD-NSGA-II from [155]. The reference normalized hyperplane was set to have 10 divisions between fitness values. From this hyperplane, each normalized candidate fitness vector was given a convergence distance d_1 to its nearest reference point using the diversity metric d_2 . The density of each reference point was then computed and used to truncate the final reference-point dominated front to be passed to the next generation. The crossover scheme used in this optimization process was a simulated binary crossover (SBX) which is evaluated in more depth in [160] and [161]. The mutation variation was done with polynomial mutation similar to that described in [159] and the variation process was inherited from [162].

5.4.1 Validation Results

To verify the results of the optimizer and simulation, a set of the tuned gains biased toward tracking error were implemented on a physical inverted pendulum system. The resulting

Table 5.3: Optimized Gains for the Inverted Pendulum

Gain	β_{01}^i	β_{02}^i	β_{03}^i	r_1^i	h_1^i	c_1^i
Pendulum	1.1362	0.4993	0.4152	52.8565	0.9969	0.9878
Cart	1.1465	0.6491	0.4744	43.9430	0.3683	1.0543

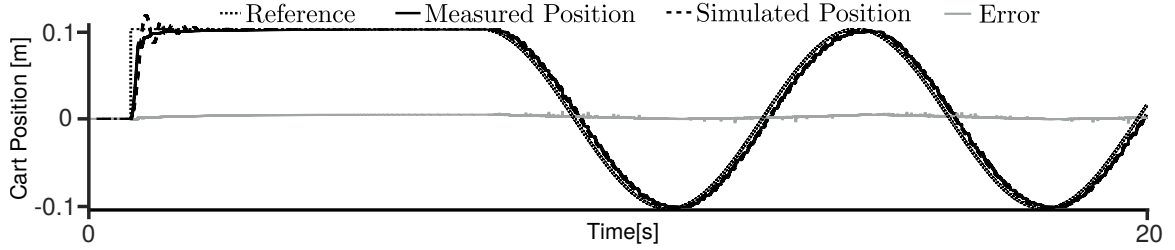


Figure 5.8: Experimental results. The inverted pendulum model validation for the cart position with the pendulum detached.

gains from the optimizer are displayed in Table 5.3. The angle of the pendulum bar and the rotation of the motor shaft were measured using AMT102-V quadrature encoders. Fig. 5.7 demonstrates the performance of the optimized parameters at various generations by selecting members of the population that dominate on the tracking error front. Fig. 5.8 demonstrates the experimentally validated cart performance results with the ADRC gain values found with the optimizer. The RPD-NSGA-II algorithm was able to compute the parameter values to achieve the desired performance on the inverted pendulum system.

5.5 Multiobjective Optimization of the Differentially-Clutched Series Elastic Actuator Controller

Once the optimizer was validated, it was applied to the multi-input DC-SEA. A similar reference profile to that shown in Fig. 5.5 was selected in an attempt to reproduce a desired spring deflection. The reference profile was selected to be challenging for the controller, as well as provide the necessary metrics to compute meaningful values for each objective in Section 5.3. The goal was to achieve a desired spring deflection in the actuator, translating to a similar output torque profile. The controller was chosen to have two extended state observers, one for controlling the contributions to the output deflection based on the motor's angular displacement and one for controlling the output deflection based on the angular displacement of the magnetic particle brake. Two observers were chosen due to the constrained condition of the actuator to measure the output torque using a load cell and, therefore, due to this constraint, $\theta_u = 0 \implies \theta_b = -\theta_s$, diminishing the need for a third

extended state observer. The feedback combiner chosen was of the nonlinear type, utilizing the *fhan* function from Equation 4.22 in Chapter 4. Therefore, from Table 5.1, there are a total of 22 tunable parameters in this case, the gains are displayed in Table 5.4.

Table 5.4: Optimized Gains for the DC-SEA

Motor Subsystem	α_1^1	α_2^1	β_{01}^1	β_{02}^1	β_{03}^1	p_1^1	p_2^1	r_0^1	h_0^1	r_1^1	h_1^1
Brake Subsystem	α_1^2	α_2^2	β_{01}^2	β_{02}^2	β_{03}^2	p_1^2	p_2^2	r_0^2	h_0^2	r_1^2	h_1^2

5.5.1 Simulation Results

The simulation consisted of the mathematical state-space model of the DC-SEA plant from Section 4.2. For every generation of the optimizer, the entire merged population (parent population and varied population, see Fig. 5.4) was simulated and the fitness values for each objective was determined. At times, the simulator would exit in error due to issues around singularities and, therefore, the population member causing the error was given a large fitness value to bias against the solution when selection occurred. The optimizer was chosen to have the crossover and mutation variation parameters set to 35, with a population of 300, over a total of 500 generations. To ensure the results provided meaningful control of the plant, a bias was placed on the tracking error. This provided much more desirable results, where the fitness values for increasing generations are displayed in Table 5.5. However, some objectives did experience some issues, which will be highlighted later. A general overview on the performance of the simulations is displayed in the Appendix.

5.6 Experimental Results

Once the optimization algorithm had run its course, the resulting final population set was evaluated experimentally with the differentially-clutched series elastic actuator. For each objective, the solution that provided the minimum was selected and the gains determined from the optimizer were physically implemented. Each of the following subsections displays the performance of the optimizer for that particular objective.

5.6.1 Tracking Error

In the context of control systems, tracking error is by far the most desirable parameters for a controller's ability. In the context of the DC-SEA, minimal tracking error refers to the closeness of the desired torque to a reference torque indicated by a clinician for suitable

Table 5.5: Objective Performance Over 500 Generations

Gen.	E_t	U_t	P_o	t_r	t_s	u_{max}	e_{ss}	t_d	N_{Δ}
10	0.9473	0.0259	31.9130	0.1580	0.5640	0.0893	0.0061	0.0040	5
20	0.8659	0.0251	35.7546	0.1540	0.5580	0.0891	0.0023	0.0040	5
30	0.8646	0.0245	26.0960	0.1540	0.5580	0.0899	0.0008	0.0100	5
40	0.8643	0.0236	25.8270	0.1540	0.5580	0.0916	0.0012	0.0060	5
50	0.8637	0.0224	22.4342	0.1540	0.5560	0.0882	0.0003	0.0760	5
100	0.8637	0.0219	15.5938	0.1620	0.5560	0.0784	0.0002	0.1420	5
150	0.8634	0.0220	17.8958	0.1240	0.5560	0.0786	0.0003	0.1140	5
200	0.8632	0.0236	15.3149	0.1600	0.5560	0.0897	0.0003	0.1420	5
250	0.8632	0.0249	25.5363	0.1240	0.5560	0.1004	0.0008	0.0080	3
300	0.8607	0.0270	25.7025	0.1340	0.5580	0.1030	0.0018	0.0040	3
350	0.8588	0.0288	10.9756	0.1240	0.8820	0.1220	0.0036	0.0040	0
400	0.8569	0.0256	1.2602	0.1240	1.2220	0.1742	0.0117	0.0060	0
450	0.8567	0.0238	4.5807	0.1260	0.5560	0.0974	0.0007	0.0220	0
500	0.8557	0.0225	0.0378	0.1260	0.5540	0.0904	0.0010	0.0460	0

rehabilitation. The strict adherence of a desired output state to a reference profile is the goal of all control systems and, therefore, this objective was biased in evaluating fitness in the optimizer. The results for tracking error in both the simulation and the experiment for the optimized gains determined in Table 5.6 are displayed in Fig. 5.9. From the experiments, one can discern that the DC-SEA was able to maintain reasonable tracking of the deflection in the spring. The small perturbation around 12 seconds is the point in which the backlash angle changed directions and, therefore, caused a brief spike in error. Generally speaking, the performance of the controller is well matched with the results obtained in simulation, and certainly performs favourable for reference tracking.

Table 5.6: Optimized Gains for Tracking Error

Gain	α_1^i	α_2^i	β_{01}^i	β_{02}^i	β_{03}^i	p_1^i	p_2^i	r_0^i	h_0^i	r_1^i	h_1^i
Motor ESO	0.50	0.18	1.62	22.48	47.59	0.86	0.03	42.94	1.01	42.61	0.95
Brake ESO	0.47	0.14	1.56	17.84	41.18	0.40	0.97	38.19	0.98	32.36	0.95

5.6.2 Control Effort

The ability of a plant to track a desired trajectory while minimizing the controller effort is ideal, as the controller effort can relate to the efficiency of a controller to reach its goal. Control effort is a significant objective in the DC-SEA, as it pertains to higher efficiency in the devices to be used for in-home rehabilitation. The gains determined by

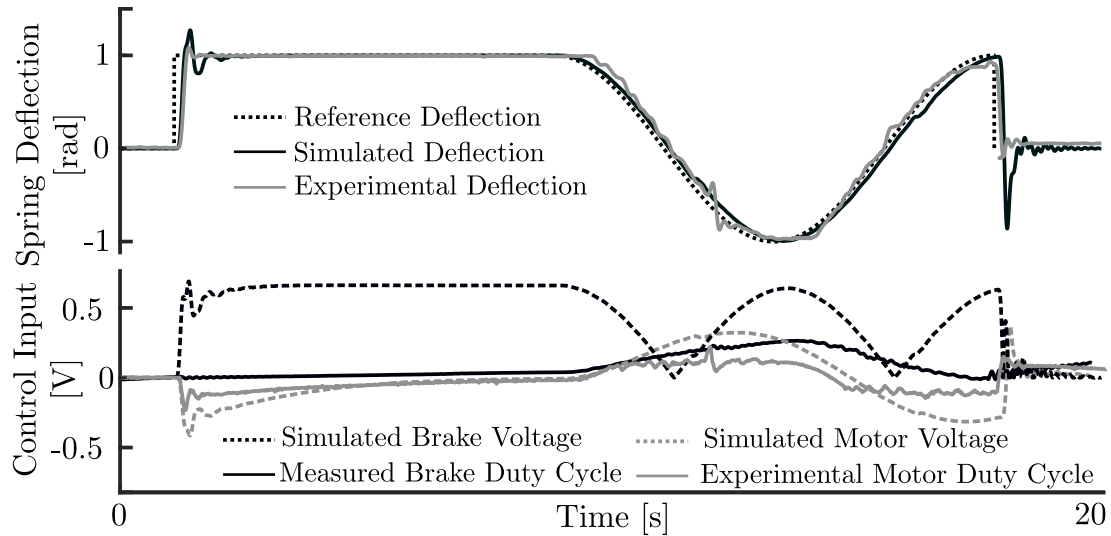


Figure 5.9: Experimental results. The best result obtained from using the controller gains determined by the optimizer biased towards the tracking error objective.

the optimizer with a minimum value for control effort fitness were implemented and the results are displayed for the optimized gains highlighted in Table 5.7 in Fig. 5.10.

Table 5.7: Optimized Gains for Controller Effort

Gain	α_1^i	α_2^i	β_{01}^i	β_{02}^i	β_{03}^i	p_1^i	p_2^i	r_0^i	h_0^i	r_1^i	h_1^i
Motor ESO	0.46	0.18	1.75	26.16	40.39	0.85	0.14	39.07	0.87	44.16	0.98
Brake ESO	0.36	0.16	1.51	20.16	37.50	0.30	0.69	35.36	0.75	43.57	0.85

5.6.3 Percent Overshoot

Minimizing percent overshoot for systems quickly reaching the reference is important for plants that require a fast and accurate response to transient states. In plants where precision is absolutely necessary and given strict conditions on how much error the plant is able to have after reaching the specified reference, percent overshoot is of utmost importance. This is applicable in devices aimed toward robot-assisted rehabilitation, as a large percent overshoot could result in patient overexertion. The results for percent overshoot in both the simulation and the experiment for the gains highlighted in Table 5.8 are displayed in Fig. 5.11.

5.6.4 Rise Time

Rise time refers to the time it takes for a plant to reach the reference after a transient state. In this case, the optimized controller was determined to have a completely different set of

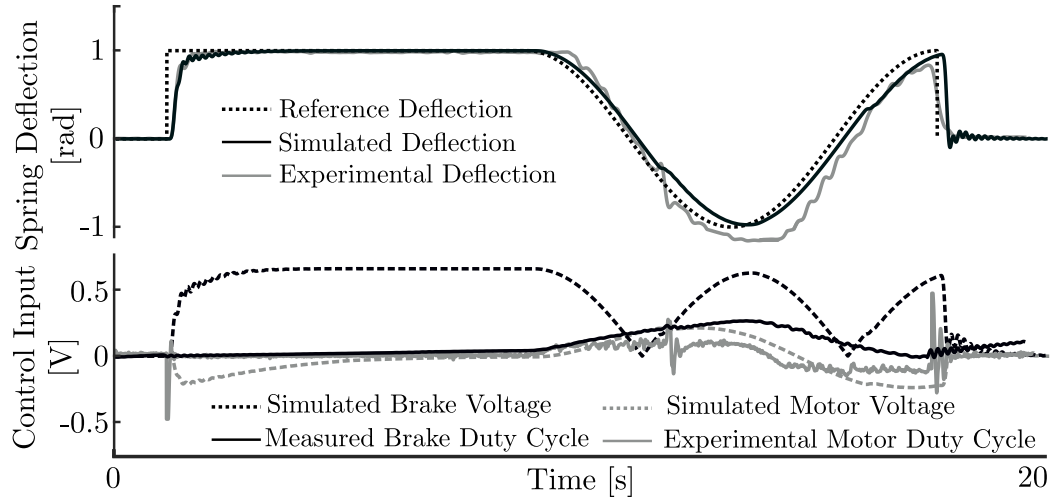


Figure 5.10: Experimental results. The best result obtained from using the controller gains determined by the optimizer biased towards minimizing control effort.

Table 5.8: Optimized Gains for Percent Overshoot

Gain	α_1^i	α_2^i	β_{01}^i	β_{02}^i	β_{03}^i	p_1^i	p_2^i	r_0^i	h_0^i	r_1^i	h_1^i
Motor ESO	0.50	0.16	1.46	25.02	38.65	0.14	0.69	38.67	0.92	38.76	0.96
Brake ESO	0.46	0.14	1.34	22.95	35.45	0.14	0.64	35.47	0.85	35.55	0.89

gains as compared to other controller gains in this section. Even though tracking error of the plant was biased, the final population of the 500th generation contained members with unstable controllers, however, this instability does ensure the output rises as quickly to the reference as possible. This is a good example on the importance of defining objectives and biasing the outcome based on the more important objectives. If there were no bias on any objective, the unstable controller shown in Fig. 5.12 would be a feasible solution and would become selected for variation into future generations. For the most part, this can have adverse effects on the progression of the controller gains, as it contradicts most of the other objectives. The discovered gains are displayed in Table 5.9. For obvious reasons, the controller was not implemented experimentally.

Table 5.9: Optimized Gains for Rise Time

Gain	α_1^i	α_2^i	β_{01}^i	β_{02}^i	β_{03}^i	p_1^i	p_2^i	r_0^i	h_0^i	r_1^i	h_1^i
Motor ESO	0.19	0.49	1.38	24.59	81.02	0.77	0.33	32.03	0.08	43.23	0.28
Brake ESO	0.15	0.48	1.24	22.99	64.82	0.17	0.63	30.57	0.08	41.65	0.27

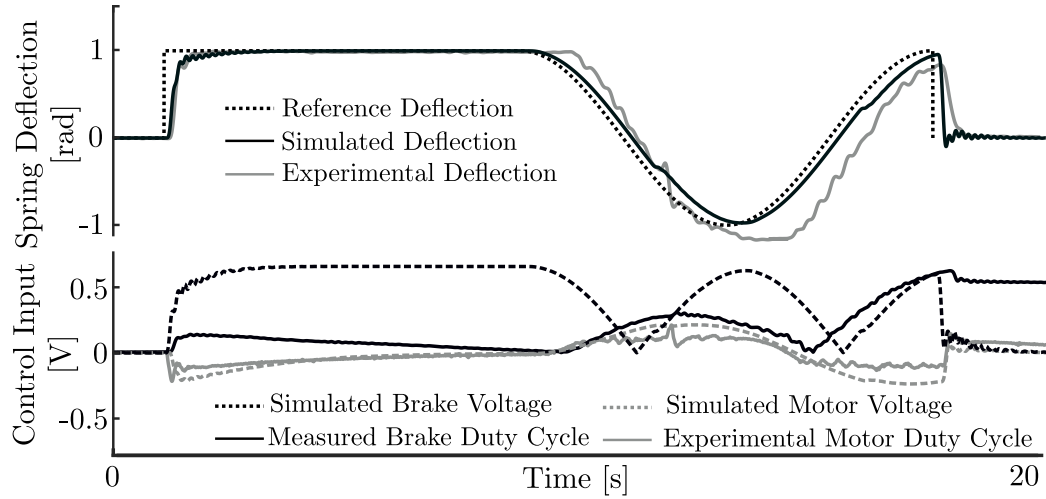


Figure 5.11: Experimental results. The best result obtained from using the controller gains determined by the optimizer biased towards minimizing percent overshoot.

Table 5.10: Optimized Gains for Settling Time

Gain	α_1^i	α_2^i	β_{01}^i	β_{02}^i	β_{03}^i	p_1^i	p_2^i	r_0^i	h_0^i	r_1^i	h_1^i
Motor ESO	0.48	0.19	1.67	25.24	46.31	0.74	0.23	42.40	1.02	41.47	0.96
Brake ESO	0.41	0.18	1.31	21.31	42.25	0.21	0.84	41.60	0.96	40.19	0.92

5.6.5 Settling Time

Settling time refers to the minimum time it takes for the output to reach and remain within 5% of the reference. The settling time can be a good metric to determine stability in response to a transient state. Settling time is a good metric for elastic actuators, as the spring element can add unwanted oscillation. Therefore, the settling time can be used to determine a controller that combats this oscillation. The results for the settling time in both the simulation and the experiment for the gains highlighted in Table 5.10 are displayed in Fig. 5.13.

5.6.6 Maximum Input

Maximum input is important for devices to be used in close proximity to humans. If the value of the control output is kept to a minimum, the power sources can be selected to be within safe ranges to humans. In this case, the minimum objective for u_{max} was the same as that for U_t . Which is intuitive as both are trying to minimize the input. The results for the maximum input value in both the simulation and the experiment for the gains highlighted in Table 5.11 are displayed in Fig. 5.14.

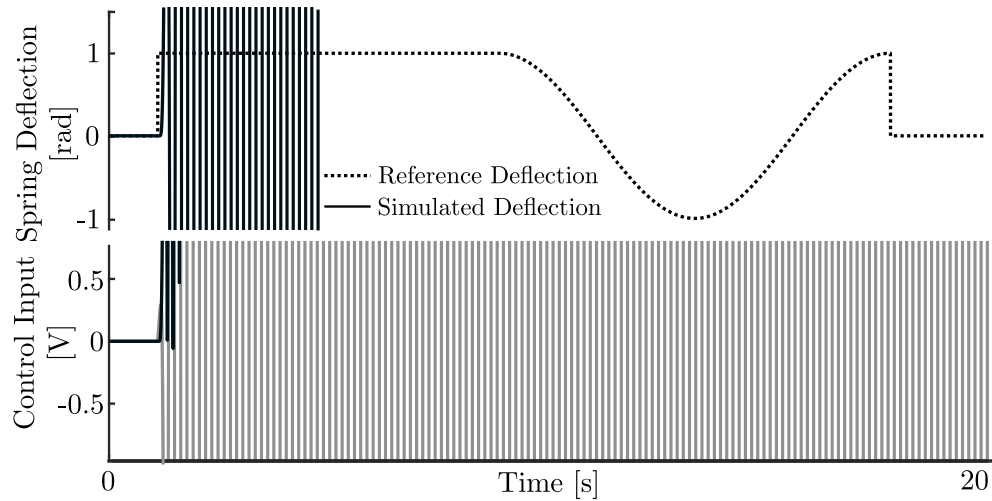


Figure 5.12: Experimental results. The best result obtained from using the controller gains determined by the optimizer biased towards minimizing rise time.

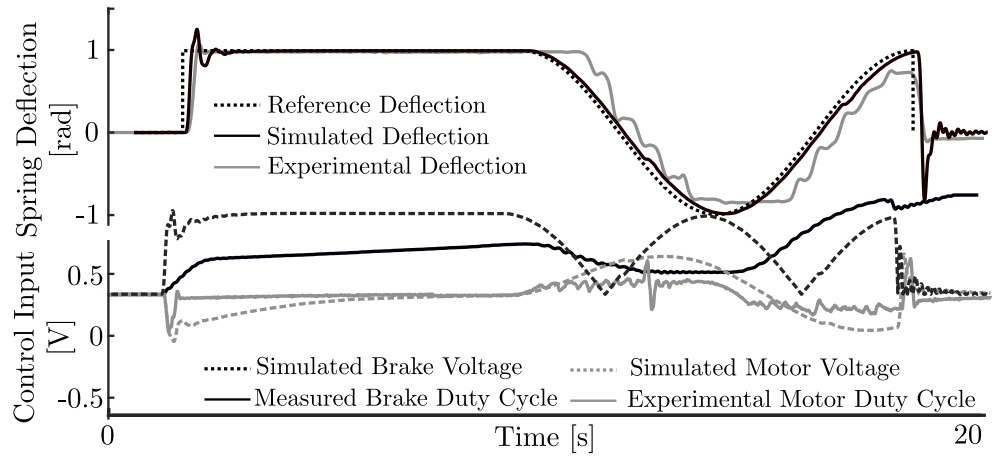


Figure 5.13: The best result obtained from using the controller gains determined by the optimizer biased towards minimizing the settling time of the spring deflection.

5.6.7 Steady-State Error

Minimizing steady-state error is important in the DS-SEA where precision in proper torque control is more desirable than the time it takes to reach the reference, allowing for smooth, well-defined motions. The condition for steady-state error was measured after the initial transient stage between zero and eight seconds. The optimized steady-state error was only considered for the static reference and not for the sinusoidal reference. The results of the steady-state error for the gains discovered in Table 5.11 are displayed in Fig. 5.14.

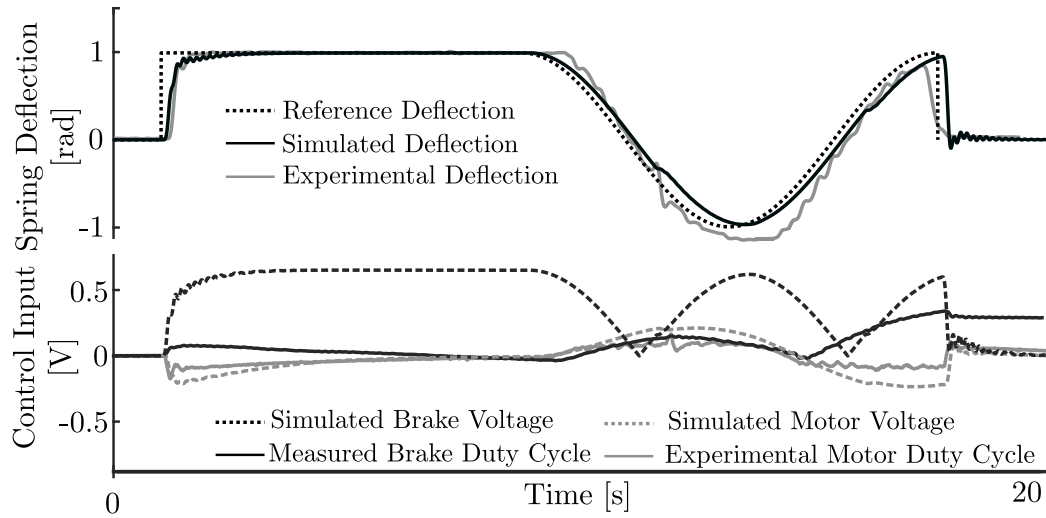


Figure 5.14: Experimental results. The best result obtained from using the controller gains determined by the optimizer biased towards minimizing the maximum value of the input.

Table 5.11: Optimized Gains for Maximum Input Value

Gain	α_1^i	α_2^i	β_{01}^i	β_{02}^i	β_{03}^i	p_1^i	p_2^i	r_0^i	h_0^i	r_1^i	h_1^i
Motor ESO	0.46	0.18	1.75	26.16	40.39	0.85	0.14	39.07	0.87	44.16	0.98
Brake ESO	0.36	0.16	1.51	20.16	37.50	0.30	0.69	35.36	0.75	43.57	0.85

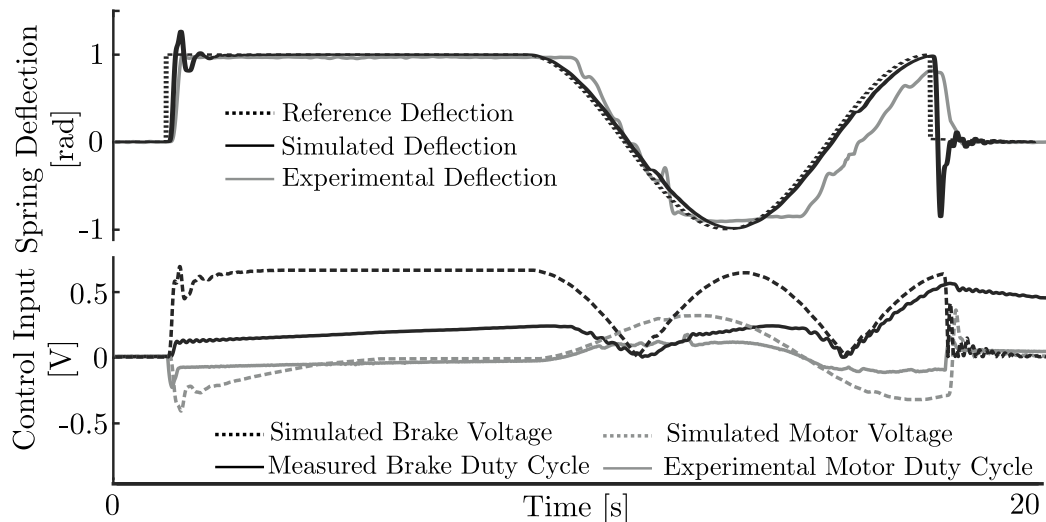


Figure 5.15: Experimental results. The best result obtained from using the controller gains determined by the optimizer biased towards minimizing steady-state error.

5.6.8 Time to Disengagement

Time to disengagement is an important damage mitigation strategy. In the context of human-machine collaboration, the time it takes to diminish stored energy in a plant to zero is important in the event of a collision. Quickly reducing the amount of energy in

Table 5.12: Optimized Gains for Steady-State Error

Gain	α_1^i	α_2^i	β_{01}^i	β_{02}^i	β_{03}^i	p_1^i	p_2^i	r_0^i	h_0^i	r_1^i	h_1^i
Motor ESO	0.48	0.18	1.68	24.84	40.25	0.96	0.37	40.62	0.79	45.54	0.96
Brake ESO	0.37	0.15	1.65	23.38	36.70	0.33	0.99	40.18	0.75	38.15	0.785

the actuator can ensure there is no holding torque and minimizes the amount of energy transferred to the output. The results of the controller minimizing time to disengagement using the gains in Table 5.13 in both the simulation and the experiment are displayed in Fig. 5.16.

Table 5.13: Optimized Gains for Disengagement Time

Gain	α_1^i	α_2^i	β_{01}^i	β_{02}^i	β_{03}^i	p_1^i	p_2^i	r_0^i	h_0^i	r_1^i	h_1^i
Motor ESO	0.09	0.37	1.51	47.34	49.20	0.80	0.18	29.82	1.65	71.74	0.61
Brake ESO	0.08	0.34	1.23	45.10	40.75	0.07	0.85	25.16	1.33	70.29	0.47

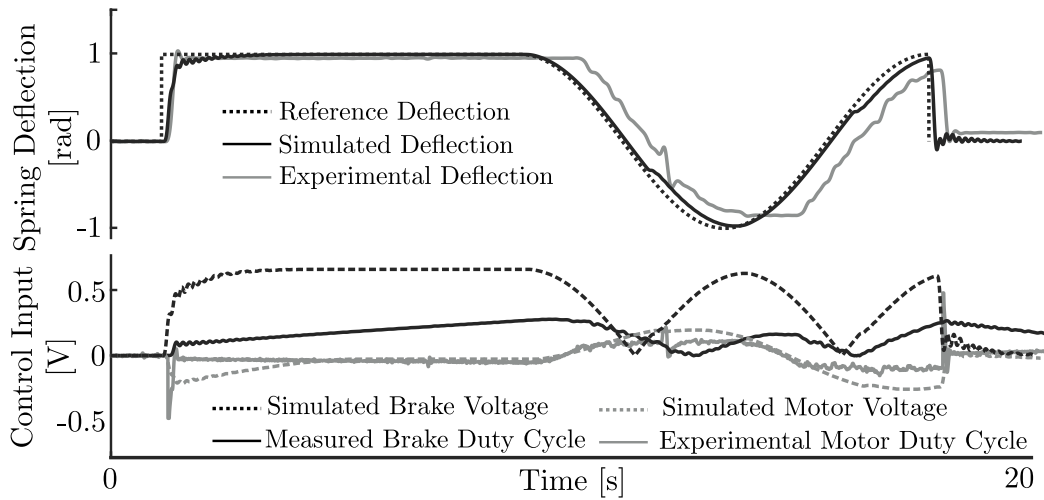


Figure 5.16: Experimental results. The best result obtained from using the controller gains determined by the optimizer biased towards minimizing disengagement time.

5.6.9 Number of Input Crossings

This objective was inserted into the algorithm as a method to reduce the number of high-switching solutions from the population. As displayed in the best solutions for rise time, high switching applications are not only difficult to implement physically, but they can also be hard on the plant by accelerating wear. This type of bang-bang control is undesirable and, therefore, this objective was put in place to persuade the solution set against high-switching applications. Therefore, this objective was given low preference and the fitness

value was a function of the number of input direction changes, therefore, naturally unbiasing high switching solutions. The results for the number of input crossings for the gains displayed in Table 5.14 in both the simulation and the experiment is demonstrated in Fig. 5.17.

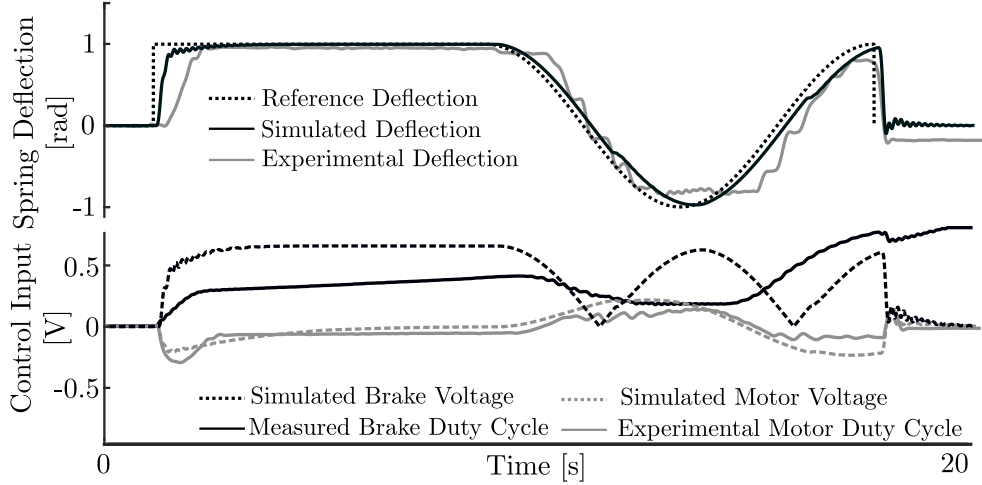


Figure 5.17: Experimental results for the best result obtained from the optimizer minimizing the number of input direction changes.

Table 5.14: Optimized Gains for Number of Input Crossings

Gain	α_1^i	α_2^i	β_{01}^i	β_{02}^i	β_{03}^i	p_1^i	p_2^i	r_0^i	h_0^i	r_1^i	h_1^i
Motor ESO	0.19	0.49	1.38	24.59	81.02	0.77	0.33	32.03	0.08	43.23	0.28
Brake ESO	0.42	0.17	1.57	21.82	36.97	0.33	0.68	37.19	0.81	35.88	0.84

5.6.10 Multiobjective Results

The optimizer has demonstrated validity in optimizing various single objective cases, however, one has the option to choose a solution that best represents their unique application from the population set at the end of the optimization. Consider five members of the resulting population and their respective fitness values for each objective as shown in Table 5.15:

If the device was to be used in the context of human-machine interaction, specifically robot-assisted rehabilitation, there may be a number of deterrents when selecting the appropriate control strategy. For example, there may be a very specific torque goal in mind to ensure that the patient does not experience overexertion or perhaps the device is destined to be mobile and, therefore, battery operated. In this case, the most significant objectives to optimize are the tracking error, control effort, and percent overshoot. If these were the

Table 5.15: Multiobjective Fitness Values for 5 Members

Member	E_t	U_t	P_o	t_r	t_s	u_{max}	e_{ss}	t_d	N_Δ
1	0.8678	0.0281	30.8697	0.1740	0.8920	0.1045	0.0076	0.1480	5
2	0.9615	0.1370	0.581	0.1680	1.2220	0.2141	0.0659	0.1440	7
3	1.1783	0.0259	1.237	0.7940	1.0140	0.0942	0.0092	0.1860	5
4	8.3227	0.6353	122.8093	0.1500	6.5020	0.4812	236.4768	0.1320	65
5	0.9098	0.0307	34.0216	0.1700	0.8820	0.1204	0.0068	0.1460	5

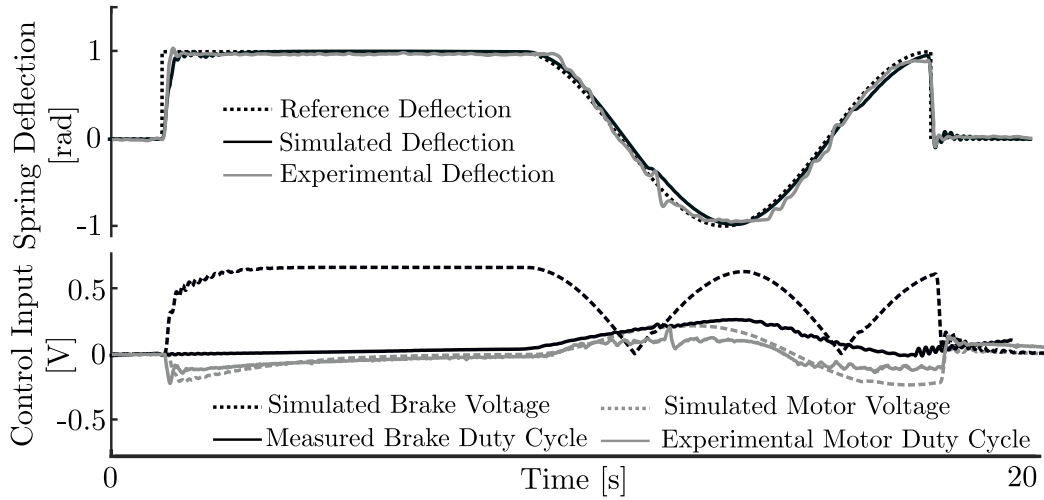


Figure 5.18: Experimental results for the multiobjective rehabilitation application, as selected by the designer.

specifications for the controller design, the three candidate solutions could be Members 1, 2, 3, and 5 of the population from Table 5.15, as each of them have reasonable values for minimizing the three objectives in question. Member 4 may be discarded, as it is dominated by every other solution with respect to the significant objectives. Furthermore, Members 1 and 5 have a percent overshoot that could be considered unreasonably high for the design specifications and, therefore, could be discarded as well. The remaining members, 2 and 3, have relatively similar values for the tracking error E_t and the percent overshoot P_o , but vary significantly in control effort U_t . The designer may also choose to select the gains optimized from Member 3 as it has the lowest control effort, compromising slightly on tracking error and percent overshoot compared to Member 2. The results of Member 2 with optimized gains from Table 5.16 from the final population set is demonstrated in Fig. 5.18. This example demonstrates the importance of multiobjective optimization in the process of selecting controller gains for specific applications, where the designer can view the trade-offs between various solutions. The ability to gauge the overall performance of a controller provides a means of tailoring the controller based on the specifications of the application.

Table 5.16: Optimized Gains for Multiobjective Problem

Gain	α_1^i	α_2^i	β_{01}^i	β_{02}^i	β_{03}^i	p_1^i	p_2^i	r_0^i	h_0^i	r_1^i	h_1^i
Motor ESO	0.30	0.02	1.59	25.98	40.23	0.73	0.21	38.91	0.71	44.00	0.82
Brake ESO	0.36	0.16	1.48	22.32	38.30	0.12	0.81	36.83	0.69	42.01	0.93

5.7 Conclusions

The most difficult portion of active disturbance rejection control is the tuning of the system parameters. Presented in this chapter was the implementation of the RPD-NSGA-II from [155] to optimize the parameters required for ADRC on a multi-input SEA. By using a multi-objective optimization technique coupled with a simulation, the parameters required to achieve the desired performance for a physical system were determined. The RPD-NSGA-II routine proved capable of handling this multi-objective optimization problem to provide the end user with a set of dominating solutions such that the designer is able to choose gain values based on the objectives most suitable for their applications. In order to choose gains that are favourable to multiple objectives, the designer could evaluate the set of fitness values for each member of the resulting population and determine how they want to bias their controller. The relative trade-offs between the objectives becomes apparent and, therefore, the designer can select the set of gains that is best suited for their applications. There are a wide number of applications for an ADRC optimization method. Since active disturbance rejection control is a favourable alternative to PID, the controller can be used in a multitude of plants ranging from robotic actuators used in medical devices to autonomous vehicles and industrial automation.

Chapter 6

Conclusions and Recommendations for Future Work

6.1 Conclusions

As part of a larger goal in developing devices to be used in home-based musculoskeletal rehabilitation, this thesis provided a foundation for the design of the actuation method for such devices through the introduction of the differentially-clutched series elastic actuator. Intelligent rehabilitation devices offer the outstanding advantage of convenience to traditional clinic-based rehabilitation methods. This thesis proposed the novel series elastic actuator as a new method for actuators to be used in applications regarding physical human-machine interaction. Beginning with the design of the actuator, a multimodal topology was invented to accommodate the multiple phases of rehabilitation. The actuator was then fabricated in-house and experimentally validated for a basic controller. Once the actuator was proven to be viable, a multi-input robust controller bearing the form of an active disturbance rejection controller was derived, implemented, and experimentally validated. The robust controller for the DC-SEA was then optimized for various desirable control objectives in elastic actuators, providing a metric for designers to choose performance metrics that are tailored to their specific applications. Therefore, this thesis covers all aspects of designing actuators to be used in robot-assisted rehabilitation.

In order to create a device tailored for musculoskeletal rehabilitation, the first step was to evaluate the patient. By starting with the evaluation of the constrained and unconstrained workspaces of individuals experiencing upper-limb musculoskeletal disorders, one can begin to determine the optimal structure of a device to be used with the actuator proposed; creating a unified device intended for safe human-machine interaction. Each

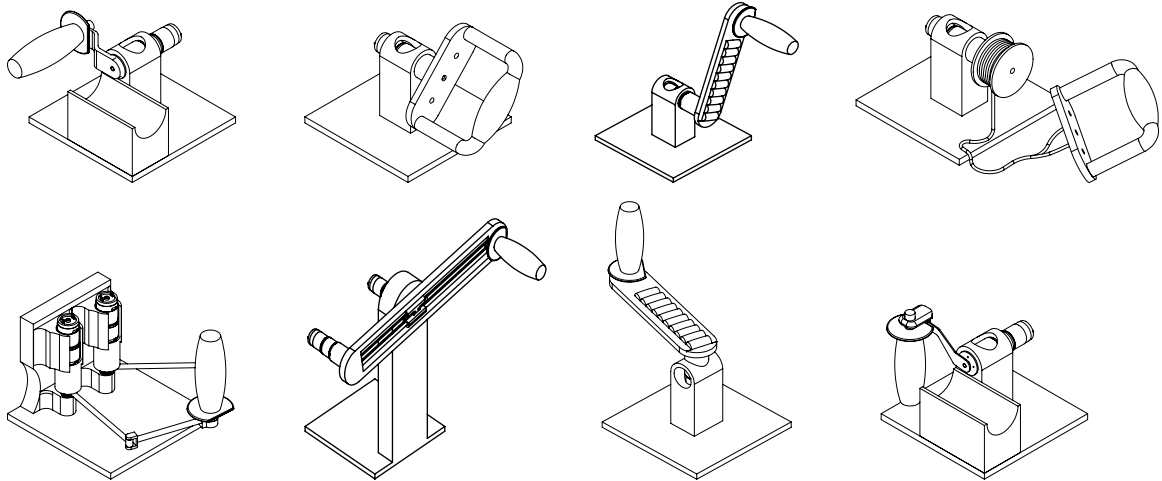


Figure 6.1: Conceptual devices for upper-limb rehabilitation

individual experiencing an MSD is unique and, therefore, it is difficult to create devices that can encapsulate the scope of all upper-limb disorders. Luckily, recent advances in 3D printing technology have provided the opportunity to create inexpensive, fully customizable mechanical systems formed to each patient's specific needs. These devices typically have one or more actuation methods including, but not limited to, electric motors, pneumatic actuators, hydraulic actuators, controllable brakes, and clutches. Fig 6.1 demonstrates a set of conceptual devices that could be used for upper-limb rehabilitation and powered by a single modular actuator such as the one presented in this thesis. In addition to the actuation method, the devices must encompass the ability to be as safe as possible to reduce the chance of injuring the patient through a combination of hardware and software solutions. On one hand, hardware solutions come in the form of series elasticity [47, 71, 163, 164], compliant and/or flexible material [165–167], and push button killswitches. These solutions are physically implemented and cannot be changed without adapting the hardware. On the other hand, software solutions make use of sensors such as cameras, infrared sensors, motion sensors, laser rangefinders, and force/torque sensors to determine whether or not a human is operating near a robot [168, 169]. There are a number of challenges associated with these devices, most of which stem from the design of the devices themselves.

The next step in the design of devices to be used in home-based rehabilitation draws from a common issue regarding safety in human-machine interaction as a whole. Safety in robotic and assistive systems, especially those tailored to physical interactions with humans, require careful attention to every detail about how energy is delivered to the patient, as well as provide information about the magnitude of applied torques, as well as the range of motion and speed. Safety must be held pinnacle in every step of the design

process, from choosing the actuation methods to the material used in the kinematic chain. In this regard, the basis and the most important component of devices to be used for HMI stems from the actuator. The actuator controls the motion of the device, as well as the forces experienced by the operator. Actuators designed for the purpose of rehabilitation should encompass the ability to perform the various stages of rehabilitation exercises. It must also provide active assistance when a patient is unable to complete a required movement on their own and passive resistance to strengthen joints as the patient progresses throughout their rehabilitation regime. In addition to these requirements, the ideal actuator should encapsulate a means of providing feedback to use in robust controllers. The differentially-clutched series elastic actuator proposed in this thesis is a novel actuator specifically designed for this branch of applications.

Chapter 3 introduced a proof-of-concept differentially-clutched series elastic actuator. This multimodal actuator was developed to facilitate the three stages of musculoskeletal rehabilitation, while ensuring that the energy in the system can always be controlled, independent of the current states of the actuator. The differentially-clutched series elastic actuator is a unified approach to resourcefully encapsulate multiple actuator goals with a single device. The elastic actuator containing the differential gearbox, magnetic particle brake, geared DC motor, and the concentric torsion spring can be used in a variety of topologies for differing applications without mechanical intervention. The actuator is safe and stable, making it suitable for applications in human-machine interaction.

A simple PID controller to the elastic actuator was initially implemented to validate the relationship between the measured spring deflection and torque experienced at the output shaft. It was found that the output torque was proportional to the spring deflection with sufficient accuracy, resulting in the ability to perform deflection control as a substitution for torque control. The addition of the elastic element provided a method of measuring the torque experienced by the user; a process that would otherwise would require an expensive torque sensor.

One issue that is introduced in hybrid devices comes in the form of nonlinearities. Nonlinearities involved in the DC-SEA came in multiple forms, through magnetic hysteresis to gear backlash. Therefore, mitigation strategies were required to accurately perform deflection control of the multi-input actuator. Two nonlinear controllers were proposed in Chapter 4 to handle them. Since elastic actuators depend on accurate angular displacement measurements, a backlash estimation algorithm was implemented and experimentally validated along with an active disturbance rejection controller. Active disturbance rejection controllers have been gaining traction as an alternative to PID controllers as they provide a means of compensating for nonlinearities. ADRC combine

deviances from a proportional linearization to a total disturbance term using extended state observers. In this thesis, both single-input and multi-input backlash-compensated ADRCs were developed and proven to outperform classical controllers for a reference torque profile. They are ideal for use in human-machine collaboration, as the interactions with a human are not predictable. Furthermore, ADRC is error based and, therefore, the exact model of the plant does not necessarily need to be known. One pitfall of the controllers is choosing optimal controller gains for multi-input systems, as the number of tunable gains increases drastically with the number of extended state observers implemented.

Multiobjective optimization explored in Chapter 5 was tasked with determining optimal ADRC gains for the multi-input DC-SEA for nine independent control objectives. The objectives were the tracking error, control effort, percent overshoot, rise time, settling time, maximum input value, steady-state error, disengagement time, and the number of input direction changes. A model of the actuator was simulated with the RPD-NSGA-II evolutionary algorithm 300,000 times over 500 generations to obtain a population with diverse fitness values pertaining to each objective. The resulting controller gains were then implemented experimentally to demonstrate the performance of the optimizer and the multi-input controller.

The results obtained in this thesis determined that multimodal elastic actuators would be a favourable choice of actuation methods for applications regarding human-machine interaction. When elastic actuators are coupled with robust controllers, the range of applications are wide. Elastic actuators provide the advantages of introducing mechanical compliance, as well as a methodology for inferring the torque experienced at the output. Both of which are requirements for stable, safe, human-machine interaction.

In this thesis, the optimal trajectory planning based on the kinematic model determined in Chapter 2 can be used to minimize the effects of involuntary joint movements. This can be used as a tool for clinicians and device designers, as the clinician may select a path that minimizes discomfort or highlights subtle movements outside of the constrained workspace to administer rehabilitation. This is equivalent to selecting a position and orientation of the arm less prone to the effects of spasms or discomfort, or by intentionally trying to increase a patient's range of motion. Lastly, as an insight into the structure of an unknown cost function of a specific individual, one may analyze the path followed by the hand through the inverse kinematic model, compute the joint angles, and in doing so may be able to define an approximate cost function to be implemented in robotic rehabilitation and/or assistance. The insight provided by the model can also be used to develop rehabilitative devices tailored around the unique needs of a patient. Depending on the patient, the optimal kinematic structure of the rehabilitation device similar to those presented in Fig. 6.1 can

be determined. The total range of motion, both constrained and unconstrained, can be used as a tool in the design of a device created to interact with a patient. Depending on a professional physical therapist's recommendations, the device may be designed to follow a trajectory that provides an optimum rehabilitative effort to target joints.

6.2 Recommendations and Future Work

Further development in the area of designing rehabilitation devices, as well as actuators tasked with interacting with humans, could consist of:

- Developing a method for better relating input current of magnetic brakes to its output torque profile. Compensating for magnetic hysteresis was absolutely necessary, which acts as a deterrent for the many advantages of the passive actuator. This would provide a better measure of determining the input to apply to the controllable brake to obtain a desired output torque.
- Designing a robust concentric torsion spring with a linear range aimed around the intended torque profiles of the actuator. The design of the compact concentric torsion spring was a difficult endeavor and undoubtedly an entire design problem on its own. The elastic element must be designed to be robust, linear, have both sides easily accessible for displacement measurements, and maintain concentricity and bidirectionality. Ideally, elastic elements would also contain the ability to vary its spring constant, where the stiffness could increase for applications requiring large torques.
- Creating a more compact version of the actuator to be used in robot-aided rehabilitation devices. The devices can then undergo a series of vigorous user trials, where the validity of the rehabilitation devices is evaluated in a controlled setting. The devices could then eventually branch off to long distance teleoperation schemes, where two people distanced from one another can physically interact through the devices, an ideal scenario for teleoperated robot-assisted rehabilitation.
- A natural next step would be to create devices similar to those shown in Fig. 6.1. The figure demonstrates conceptual topologies for devices that could be used for robot-assisted upper-limb rehabilitation, where the design could be tailored for the unique needs and range of motion of a patient.

References

- [1] A. Bicchi and G. Tonietti, "Fast and" soft-arm" tactics [robot arm design]," *IEEE Robotics & Automation Magazine*, vol. 11, no. 2, pp. 22–33, 2004.
- [2] A. Hochstenbach-Waelen and H. A. Seelen, "Embracing change: practical and theoretical considerations for successful implementation of technology assisting upper limb training in stroke," *Journal of Neuroengineering and Rehabilitation*, vol. 9, no. 1, p. 52, 2012.
- [3] A. M. Ríos-Rincón, K. Adams, J. Magill-Evans, and A. Cook, "Playfulness in children with limited motor abilities when using a robot," *Physical & Occupational Therapy in Pediatrics*, vol. 36, no. 3, pp. 232–246, 2016.
- [4] N. Paneth, T. Hong, and S. Korzeniewski, "The descriptive epidemiology of cerebral palsy," *Clinics in Perinatology*, vol. 33, no. 2, pp. 251–267, 2006.
- [5] H. P. Van der Ploeg, A. J. Van der Beek, L. H. Van der Woude, and W. van Mechelen, "Physical activity for people with a disability," *Sports Medicine*, vol. 34, no. 10, pp. 639–649, 2004.
- [6] R. A. Macpherson, T. J. Lane, A. Collie, and C. B. McLeod, "Age, sex, and the changing disability burden of compensated work-related musculoskeletal disorders in canada and australia," *BMC public health*, vol. 18, no. 1, p. 758, 2018.
- [7] A. M. Bruder, N. Shields, K. J. Dodd, and N. F. Taylor, "Prescribed exercise programs may not be effective in reducing impairments and improving activity during upper limb fracture rehabilitation: a systematic review," *Journal of Physiotherapy*, vol. 63, no. 4, pp. 205–220, 2017.
- [8] J. Prall and M. Ross, "The management of work-related musculoskeletal injuries in an occupational health setting: the role of the physical therapist," *Journal of Exercise Rehabilitation*, vol. 15, no. 2, p. 193, 2019.
- [9] K. Burton and N. Kendall, "Musculoskeletal disorders," *BMJ*, vol. 348, 2014. [Online]. Available: <https://www.bmj.com/content/348/bmj.g1076>
- [10] H. Hoenig, J. A. Sanford, T. Butterfield, P. C. Griffiths *et al.*, "Development of a teletechnology protocol for in-home rehabilitation," *Journal of Rehabilitation Research and Development*, vol. 43, no. 2, p. 287, 2006.

- [11] P. S. Lum, C. G. Burgar, P. C. Shor, M. Majmundar, and M. Van der Loos, "Robot-assisted movement training compared with conventional therapy techniques for the rehabilitation of upper-limb motor function after stroke," *Archives of Physical Medicine and Rehabilitation*, vol. 83, no. 7, pp. 952–959, 2002.
- [12] V. Maheu, P. S. Archambault, J. Frappier, and F. Routhier, "Evaluation of the JACO robotic arm: Clinico-economic study for powered wheelchair users with upper-extremity disabilities," in *International Conference on Rehabilitation Robotics*, 2011, pp. 1–5.
- [13] B. Graf, A. Hans, J. Kubacki, and R. Schraft, "Robotic home assistant care-o-bot ii," in *Proceedings of the Engineering in Medicine and Biology Conference*, vol. 3. IEEE, 2002, pp. 2343–2344.
- [14] K. Kawamura, S. Bagchi, M. Iskarous, and M. Bishay, "Intelligent robotic systems in service of the disabled," *IEEE Transactions on Rehabilitation Engineering*, vol. 3, no. 1, pp. 14–21, 1995.
- [15] M. Najafi, M. Sharifi, K. Adams, and M. Tavakoli, "Robotic assistance for children with cerebral palsy based on learning from tele-cooperative demonstration," *International Journal of Intelligent Robotics and Applications*, pp. 1–12, 2017.
- [16] P. S. Lum, C. G. Burgar, M. Van der Loos, and P. C. Shor, "MIME robotic device for upper-limb neurorehabilitation in subacute stroke subjects: A follow-up study," *Journal of Rehabilitation Research and Development*, vol. 43, no. 5, p. 631, 2006.
- [17] H. I. Krebs, M. Ferraro, S. P. Buerger, M. J. Newbery, A. Makiyama, M. Sandmann, D. Lynch, B. T. Volpe, and N. Hogan, "Rehabilitation robotics: pilot trial of a spatial extension for MIT-Manus," *Journal of NeuroEngineering and Rehabilitation*, vol. 1, no. 1, p. 5, 2004.
- [18] E. Mohammadi, H. Zohoor, and M. Khadem, "Design and prototype of an active assistive exoskeletal robot for rehabilitation of elbow and wrist," *Scientia Iranica. Transaction B, Mechanical Engineering*, vol. 23, no. 3, p. 998, 2016.
- [19] D. Centonze, G. Koch, V. Versace, F. Mori, S. Rossi, L. Brusa, K. Grossi, F. Torelli, C. Prosperetti, A. Cervellino *et al.*, "Repetitive transcranial magnetic stimulation of the motor cortex ameliorates spasticity in multiple sclerosis," *Neurology*, vol. 68, no. 13, pp. 1045–1050, 2007.
- [20] J. F. McLaughlin, K. F. Bjornson, S. J. Astley, C. Graubert, R. M. Hays, T. S. Roberts, R. Price, and N. Temkin, "Selective dorsal rhizotomy: efficacy and safety in an investigator-masked randomized clinical trial," *Developmental Medicine & Child Neurology*, vol. 40, no. 4, pp. 220–232, 1998.
- [21] G. B. Prange, M. J. Jannink, C. G. Groothuis-Oudshoorn, H. J. Hermens, and M. J. IJzerman, "Systematic review of the effect of robot-aided therapy on recovery of the hemiparetic arm after stroke," *Journal of Rehabilitation Research and Development*, vol. 43, no. 2, p. 171, 2006.

- [22] W. S. Harwin, J. L. Patton, and V. R. Edgerton, “Challenges and opportunities for robot-mediated neurorehabilitation,” *Proceedings of the IEEE*, vol. 94, no. 9, pp. 1717–1726, 2006.
- [23] S. I. Lee, C. P. Adans-Dester, M. Grimaldi, A. V. Dowling, P. C. Horak, R. M. Black-Schaffer, P. Bonato, and J. T. Gwin, “Enabling stroke rehabilitation in home and community settings: A wearable sensor-based approach for upper-limb motor training,” *IEEE Journal of Translational Engineering in Health and Medicine*, vol. 6, pp. 1–11, 2018.
- [24] H. Yu, S. Huang, G. Chen, Y. Pan, and Z. Guo, “Human–robot interaction control of rehabilitation robots with series elastic actuators,” *IEEE Transactions on Robotics*, vol. 31, no. 5, pp. 1089–1100, 2015.
- [25] N. T. Pham, N. D. K. Nguyen, T. T. Nguyen, S. B. Kim *et al.*, “Development of series elastics actuators for physical rehabilitation devices,” in *International Conference on Advanced Engineering Theory and Applications*. Springer, 2016, pp. 702–712.
- [26] A. J. Veale and S. Q. Xie, “Towards compliant and wearable robotic orthoses: A review of current and emerging actuator technologies,” *Medical Engineering & Physics*, vol. 38, no. 4, pp. 317–325, 2016.
- [27] S.-H. Chen, W.-M. Lien, W.-W. Wang, G.-D. Lee, L.-C. Hsu, K.-W. Lee, S.-Y. Lin, C.-H. Lin, L.-C. Fu, J.-S. Lai *et al.*, “Assistive control system for upper limb rehabilitation robot,” *IEEE Transactions on Neural Systems and Rehabilitation Engineering*, vol. 24, no. 11, pp. 1199–1209, 2016.
- [28] K.-S. Lee, J.-H. Park, J. Beom, and H.-S. Park, “Design and evaluation of passive shoulder joint tracking module for upper-limb rehabilitation robots,” *Frontiers in Neurorobotics*, vol. 12, 2018.
- [29] R. Morales, F. J. Badesa, N. García-Aracil, J. M. Sabater, and C. Pérez-Vidal, “Pneumatic robotic systems for upper limb rehabilitation,” *Medical & Biological Engineering & Computing*, vol. 49, no. 10, p. 1145, 2011.
- [30] J. Klein, S. Spencer, J. Allington, J. E. Bobrow, and D. J. Reinkensmeyer, “Optimization of a parallel shoulder mechanism to achieve a high-force, low-mass, robotic-arm exoskeleton,” *IEEE Transactions on Robotics*, vol. 26, no. 4, pp. 710–715, 2010.
- [31] D. Caldwell and N. Tsagarakis, “Biomimetic actuators in prosthetic and rehabilitation applications,” *Technology and Health Care*, vol. 10, no. 2, pp. 107–120, 2002.
- [32] T. G. Sugar, J. He, E. J. Koeneman, J. B. Koeneman, R. Herman, H. Huang, R. S. Schultz, D. Herring, J. Wanberg, S. Balasubramanian *et al.*, “Design and control of Rupert: a device for robotic upper extremity repetitive therapy,” *IEEE Transactions on Neural Systems and Rehabilitation Engineering*, vol. 15, no. 3, pp. 336–346, 2007.

- [33] P. Culmer, A. Jackson, S. Makower, J. Cozens, M. Levesley, M. Mon-Williams, and B. Bhakta, “A novel robotic system for quantifying arm kinematics and kinetics: description and evaluation in therapist-assisted passive arm movements post-stroke,” *Journal of neuroscience methods*, vol. 197, no. 2, pp. 259–269, 2011.
- [34] M. Ding, J. Ueda, and T. Ogasawara, “Pinpointed muscle force control using a power-assisting device: System configuration and experiment,” in *Biomedical Robotics and Biomechanics, 2008. BioRob 2008. 2nd IEEE RAS & EMBS International Conference on*. IEEE, 2008, pp. 181–186.
- [35] H. Du, W. Xiong, Q. Li, L. Wang *et al.*, “Energy efficiency control of pneumatic actuator systems through nonlinear dynamic optimization,” *Journal of Cleaner Production*, vol. 184, pp. 511–519, 2018.
- [36] E. T. Wolbrecht, D. J. Reinkensmeyer, and J. E. Bobrow, “Pneumatic control of robots for rehabilitation,” *The International Journal of Robotics Research*, vol. 29, no. 1, pp. 23–38, 2010.
- [37] A. Umemura, Y. Saito, and K. Fujisaki, “A study on power-assisted rehabilitation robot arms operated by patient with upper limb disabilities,” in *Rehabilitation Robotics, 2009. ICORR 2009. IEEE International Conference on*. IEEE, 2009, pp. 451–456.
- [38] C. Pylatiuk, A. Kargov, I. Gaiser, T. Werner, S. Schulz, and G. Bretthauer, “Design of a flexible fluidic actuation system for a hybrid elbow orthosis,” in *Rehabilitation Robotics, 2009. ICORR 2009. IEEE International Conference on*. IEEE, 2009, pp. 167–171.
- [39] E. Treadway, Z. Gan, C. D. Remy, and R. B. Gillespie, “Toward controllable hydraulic coupling of joints in a wearable robot,” *IEEE Transactions on Robotics*, vol. 34, no. 3, pp. 748–763, 2018.
- [40] N. Vitiello, T. Lenzi, S. Roccella, S. M. M. De Rossi, E. Cattin, F. Giovacchini, F. Vecchi, and M. C. Carrozza, “Neuroexos: A powered elbow exoskeleton for physical rehabilitation,” *IEEE Transactions on Robotics*, vol. 29, no. 1, pp. 220–235, 2013.
- [41] M. O. Abe and N. Yamada, “Modulation of elbow joint stiffness in a vertical plane during cyclic movement at lower or higher frequencies than natural frequency,” *Experimental brain research*, vol. 153, no. 3, pp. 394–399, 2003.
- [42] D. W. Franklin, E. Burdet, R. Osu, M. Kawato, and T. E. Milner, “Functional significance of stiffness in adaptation of multijoint arm movements to stable and unstable dynamics,” *Experimental Brain Research*, vol. 151, no. 2, pp. 145–157, 2003.
- [43] A. Otten, C. Voort, A. Stienen, R. Aarts, E. van Asseldonk, and H. van der Kooij, “Limpact: A hydraulically powered self-aligning upper limb exoskeleton,” *IEEE/ASME transactions on mechatronics*, vol. 20, no. 5, pp. 2285–2298, 2015.

- [44] P. Polygerinos, Z. Wang, K. C. Galloway, R. J. Wood, and C. J. Walsh, “Soft robotic glove for combined assistance and at-home rehabilitation,” *Robotics and Autonomous Systems*, vol. 73, pp. 135–143, 2015.
- [45] A. B. Zoss, H. Kazerooni, and A. Chu, “Biomechanical design of the berkeley lower extremity exoskeleton (bleex),” *IEEE/ASME Transactions on Mechatronics*, vol. 11, no. 2, pp. 128–138, 2006.
- [46] C. Mavroidis, J. Nikitczuk, B. Weinberg, G. Danaher, K. Jensen, P. Pelletier, J. Prugnarola, R. Stuart, R. Arango, M. Leahey *et al.*, “Smart portable rehabilitation devices,” *Journal of NeuroEngineering and Rehabilitation*, vol. 2, no. 1, p. 18, 2005.
- [47] G. A. Pratt and M. M. Williamson, “Series elastic actuators,” *Intelligent Robots and Systems 95. Human Robot Interaction and Cooperative Robots*, *Proceedings. 1995 IEEE/RSJ International Conference on*, vol. 1, pp. 399–406, 1995.
- [48] H. Vallery, J. Veneman, E. Van Asseldonk, R. Ekkelenkamp, M. Buss, and H. Van Der Kooij, “Compliant actuation of rehabilitation robots,” *IEEE Robotics & Automation Magazine*.
- [49] D. W. Robinson, “Design and analysis of series elasticity in closed-loop actuator force control,” Ph.D. dissertation, Massachusetts Institute of Technology, 2000.
- [50] C. Rossa, J. Lozada, and A. Micaelli, “Design and control of a dual unidirectional brake hybrid actuation system for haptic devices,” *IEEE Transactions on Haptics*, vol. 7, no. 4, pp. 442–453, Oct 2014.
- [51] S. Zhang, S. Guo, Y. Fu, L. Boulardot, Q. Huang, H. Hirata, and H. Ishihara, “Integrating compliant actuator and torque limiter mechanism for safe home-based upper-limb rehabilitation device design,” *Journal of Medical and Biological Engineering*, vol. 37, no. 3, pp. 357–364, 2017.
- [52] S. Oh and K. Kong, “High-precision robust force control of a series elastic actuator,” *IEEE/ASME Transactions on Mechatronics*, vol. 22, no. 1, pp. 71–80, 2017.
- [53] F. Conti and O. Khatib, “A new actuation approach for haptic interface design,” *The International Journal of Robotics Research*, vol. 28, no. 6, pp. 834–848, 2009.
- [54] E. Sariyildiz, G. Chen, and H. Yu, “A unified robust motion controller design for series elastic actuators,” *IEEE/ASME Transactions on Mechatronics*, vol. 22, no. 5, pp. 2229–2240, 2017.
- [55] H.-C. Hsieh, D.-F. Chen, L. Chien, and C.-C. Lan, “Design of a parallel actuated exoskeleton for adaptive and safe robotic shoulder rehabilitation,” *IEEE/ASME Trans. Mechatronics*, vol. 22, no. 5, pp. 2034–2045, 2017.
- [56] J. Wu, J. Huang, Y. Wang, and K. Xing, “Rlresn-based pid adaptive control for a novel wearable rehabilitation robotic hand driven by pm-ts actuators,” *International Journal of Intelligent Computing and Cybernetics*, vol. 5, no. 1, pp. 91–110, 2012.

- [57] G. Wyeth, “Demonstrating the safety and performance of a velocity sourced series elastic actuator,” in *Robotics and Automation, 2008. ICRA 2008. IEEE International Conference on*. IEEE, 2008, pp. 3642–3647.
- [58] K. Kong, J. Bae, and M. Tomizuka, “A compact rotary series elastic actuator for human assistive systems,” *IEEE/ASME Transactions on Mechatronics*, vol. 17, no. 2, pp. 288–297, 2012.
- [59] B. Chen, X. Zhao, H. Ma, L. Qin, and W.-H. Liao, “Design and characterization of a magneto-rheological series elastic actuator for a lower extremity exoskeleton,” *Smart Materials and Structures*, vol. 26, no. 10, p. 105008, 2017.
- [60] A. H. Stienen, E. E. Hekman, H. Ter Braak, A. M. Aalsma, F. C. van der Helm, and H. van der Kooij, “Design of a rotational hydro-elastic actuator for an active upper-extremity rehabilitation exoskeleton,” in *Biomedical Robotics and Biomechatronics, 2008. BioRob 2008. 2nd IEEE RAS & EMBS International Conference on*. IEEE, 2008, pp. 881–888.
- [61] N. G. Tsagarakis, M. Laffranchi, B. Vanderborght, and D. G. Caldwell, “A compact soft actuator unit for small scale human friendly robots,” *Robotics and Automation, 2009. ICRA'09. IEEE International Conference on*, pp. 4356–4362, 2009.
- [62] S.-S. Yoon, S. Kang, S.-k. Yun, S.-J. Kim, Y.-H. Kim, and M. Kim, “Safe arm design with mr-based passive compliant joints and visco—elastic covering for service robot applications,” *Journal of Mechanical Science and Technology*, vol. 19, no. 10, pp. 1835–1845, 2005.
- [63] N. Paine, S. Oh, and L. Sentis, “Design and control considerations for high-performance series elastic actuators,” *IEEE/ASME Transactions on Mechatronics*, vol. 19, no. 3, pp. 1080–1091, 2014.
- [64] J. P. Cummings, D. Ruiken, E. L. Wilkinson, M. W. Lanighan, R. A. Grupen, and F. C. Sup, “A compact, modular series elastic actuator,” *Journal of Mechanisms and Robotics*, vol. 8, no. 4, p. 041016, 2016.
- [65] A. Calanca and P. Fiorini, “Understanding environment-adaptive force control of series elastic actuators,” *IEEE/ASME Transactions on Mechatronics*, vol. 23, no. 1, pp. 413–423, 2018.
- [66] H. Yu, S. Huang, G. Chen, and N. Thakor, “Control design of a novel compliant actuator for rehabilitation robots,” *Mechatronics*, vol. 23, no. 8, pp. 1072–1083, 2013.
- [67] M. Lauria, M.-A. Legault, M.-A. Lavoie, and F. Michaud, “Differential elastic actuator for robotic interaction tasks,” in *Robotics and Automation, 2008. ICRA 2008. IEEE International Conference on*. IEEE, 2008, pp. 3606–3611.

- [68] E. J. Rouse, L. M. Mooney, and H. M. Herr, “Clutchable series-elastic actuator: Implications for prosthetic knee design,” *The International Journal of Robotics Research*, vol. 33, no. 13, pp. 1611–1625, 2014.
- [69] T. Zhang and H. Huang, “Design and control of a series elastic actuator with clutch for hip exoskeleton for precise assistive magnitude and timing control and improved mechanical safety,” *IEEE/ASME Transactions on Mechatronics*, 2019.
- [70] C. Rossa, J. Lozada, and A. Micaelli, “Design and control of a dual unidirectional brake hybrid actuation system for haptic devices,” *IEEE Transactions on Haptics*, vol. 7, no. 4, pp. 442–453, 2014.
- [71] B. DeBoon, S. Nokleby, N. La Delfa, and C. Rossa, “Differentially-clutched series elastic actuator for robot-aided musculoskeletal rehabilitation,” in *2019 International Conference on Robotics and Automation (ICRA)*. IEEE, 2019, pp. 1507–1513.
- [72] U. Mettin, P. X. La Hera, L. B. Freidovich, and A. S. Shiriaev, “Parallel elastic actuators as a control tool for preplanned trajectories of underactuated mechanical systems,” *The International Journal of Robotics Research*, vol. 29, no. 9, pp. 1186–1198, 2010.
- [73] R. Alexander, “Three uses for springs in legged locomotion,” *International Journal of Robotics Research*, vol. 9, no. 2, pp. 53–61, 1990.
- [74] D. F. Häufle, M. Taylor, S. Schmitt, and H. Geyer, “A clutched parallel elastic actuator concept: Towards energy efficient powered legs in prosthetics and robotics,” pp. 1614–1619, 2012.
- [75] S. Toxiri, A. Calanca, J. Ortiz, P. Fiorini, and D. G. Caldwell, “A parallel-elastic actuator for a torque-controlled back-support exoskeleton,” *IEEE Robotics and Automation Letters*, 2017.
- [76] M. Plooiij, M. Wisse, and H. Vallery, “Reducing the energy consumption of robots using the bidirectional clutched parallel elastic actuator,” *IEEE Transactions on Robotics*, vol. 32, no. 6, pp. 1512–1523, 2016.
- [77] M. Plooiij, G. Mathijssen, P. Cherelle, D. Lefeber, and B. Vanderborght, “Lock your robot: A review of locking devices in robotics,” *IEEE Robotics & Automation Magazine*, vol. 22, no. 1, pp. 106–117, 2015.
- [78] M. Plooiij, W. Wolfslag, and M. Wisse, “Clutched elastic actuators,” *IEEE/ASME Transactions on Mechatronics*, vol. 22, no. 2, pp. 739–750, 2017.
- [79] D. Leach, F. Günther, N. Maheshwari, and F. Iida, “Linear multi-modal actuation through discrete coupling,” in *Intelligent Robots and Systems (IROS), 2012 IEEE/RSJ International Conference on*. IEEE, 2012, pp. 2437–2442.

- [80] D. Chapuis, X. Michel, R. Gassert, C.-M. Chew, E. Burdet, and H. Bleuler, “A haptic knob with a hybrid ultrasonic motor and powder clutch actuator,” pp. 200–205, 2007.
- [81] A. Tustin, “The effects of backlash and of speed-dependent friction on the stability of closed-cycle control systems,” *Journal of the Institution of Electrical Engineers-Part IIA: Automatic Regulators and Servo Mechanisms*, vol. 94, no. 1, pp. 143–151, 1947.
- [82] Z. Shi and Z. Zuo, “Backstepping control for gear transmission servo systems with backlash nonlinearity,” *IEEE Transactions on Automation Science and Engineering*, vol. 12, no. 2, pp. 752–757, 2014.
- [83] M. Nordin, J. Galic’, and P.-O. Gutman, “New models for backlash and gear play,” *International Journal of Adaptive Control and Signal Processing*, vol. 11, no. 1, pp. 49–63, 1997.
- [84] M. Nordin and P.-O. Gutman, “Controlling mechanical systems with backlash—a survey,” *Automatica*, vol. 38, no. 10, pp. 1633–1649, 2002.
- [85] S. Oh and K. Kong, “High-precision robust force control of a series elastic actuator,” *IEEE/ASME Transactions on Mechatronics*, vol. 22, no. 1, pp. 71–80, 2016.
- [86] M. Przybyła, M. Kordasz, R. Madoński, P. Herman, and P. Sauer, “Active disturbance rejection control of a 2dof manipulator with significant modeling uncertainty,” *Bulletin of the Polish Academy of Sciences: Technical Sciences*, vol. 60, no. 3, pp. 509–520, 2012.
- [87] X. Yang, J. Cui, D. Lao, D. Li, and J. Chen, “Input shaping enhanced active disturbance rejection control for a twin rotor multi-input multi-output system (trms),” *ISA Transactions*, vol. 62, pp. 287–298, 2016.
- [88] J. Pratt, B. Krupp, and C. Morse, “Series elastic actuators for high fidelity force control,” *Industrial Robot: An International Journal*, vol. 29, no. 3, pp. 234–241, 2002.
- [89] Y. Li, M. Zeng, H. An, and C. Wang, “Disturbance observer-based control for nonlinear systems subject to mismatched disturbances with application to hypersonic flight vehicles,” *International Journal of Advanced Robotic Systems*, vol. 14, no. 2, p. 1729881417699148, 2017.
- [90] Y. Lin, Z. Chen, and B. Yao, “Decoupled torque control of series elastic actuator with adaptive robust compensation of time-varying load-side dynamics,” *IEEE Transactions on Industrial Electronics*, 2019.
- [91] M. L. Corradini, A. Cristofaro, and G. Orlando, “Robust stabilization of multi input plants with saturating actuators,” *IEEE Transactions on Automatic Control*, vol. 55, no. 2, pp. 419–425, 2010.

- [92] R. W. Bohannon and M. B. Smith, "Interrater reliability of a modified ashworth scale of muscle spasticity," *Physical Therapy*, vol. 67, no. 2, pp. 206–207, 1987.
- [93] F. Biering-Sørensen, J. B. Nielsen, and K. Klinge, "Spasticity-assessment: a review," *Spinal Cord*, vol. 44, no. 12, pp. 708–722, 2006.
- [94] C. Rossa, M. Najafi, M. Tavakoli, and K. Adams, "Nonlinear workspace mapping for telerobotic assistance of upper limb in patients with severe movement disorders," in *2017 IEEE International Conference on Systems, Man, and Cybernetics (SMC)*. IEEE, 2017, pp. 2255–2260.
- [95] B. J. Borbély and P. Szolgay, "Real-time inverse kinematics for the upper limb: a model-based algorithm using segment orientations," *Biomedical Engineering Online*, vol. 16, no. 1, p. 21, 2017.
- [96] K. Wang, S. Li, C. Xu, and N. Yu, "An extended kinematic model for arm rehabilitation training and assessment," in *2016 International Conference on Advanced Robotics and Mechatronics (ICARM)*. IEEE, 2016, pp. 117–121.
- [97] A. Lioulemes, M. Theofanidis, and F. Makedon, "Quantitative analysis of the human upper-limb kinematic model for robot-based rehabilitation applications," in *2016 IEEE International Conference on Automation Science and Engineering (CASE)*. IEEE, 2016, pp. 1061–1066.
- [98] M. H. Barri, A. Widyotriatmo *et al.*, "Path reference generation for upper-limb rehabilitation with kinematic model," in *2018 IEEE International Conference on Robotics, Biomimetics, and Intelligent Computational Systems (Robionetics)*. IEEE, 2018, pp. 38–43.
- [99] R. Fazel-Rezai, E. Shwedyk, and S. Onyshko, "Three dimensional kinematic model of the upper limb with ten degrees of freedom," in *Proceedings of the 19th Annual International Conference of the IEEE Engineering in Medicine and Biology Society. Magnificent Milestones and Emerging Opportunities in Medical Engineering* (Cat. No. 97CH36136), vol. 4. IEEE, 1997, pp. 1735–1737.
- [100] W. Masinghe, G. Collier, A. Ordys, and T. Nanayakkara, "A novel approach to determine the inverse kinematics of a human upper limb model with 9 degrees of freedom," in *2012 IEEE-EMBS Conference on Biomedical Engineering and Sciences*. IEEE, 2012, pp. 525–530.
- [101] J. Lenarcic and A. Umek, "Simple model of human arm reachable workspace," *IEEE Transactions on Systems, Man, and Cybernetics*, vol. 24, no. 8, pp. 1239–1246, Aug 1994.
- [102] M. Benati, S. Gaglio, P. Morasso, V. Tagliasco, and R. Zaccaria, "Anthropomorphic robotics," *Biological Cybernetics*, vol. 38, no. 3, pp. 125–140, 1980.

- [103] B. Bolsterlee, D. H. Veeger, and E. K. Chadwick, "Clinical applications of musculoskeletal modelling for the shoulder and upper limb," *Medical & Biological Engineering & Computing*, vol. 51, no. 9, pp. 953–963, 2013.
- [104] R. Hartenberg and J. Denavit, "A kinematic notation for lower pair mechanisms based on matrices," *Journal of Applied Mechanics*, vol. 77, no. 2, pp. 215–221, 1955.
- [105] Y. Xia and J. Wang, "A dual neural network for kinematic control of redundant robot manipulators," *IEEE Transactions on Systems, Man, and Cybernetics, Part B (Cybernetics)*, vol. 31, no. 1, pp. 147–154, Feb 2001.
- [106] L. Sciavicco and B. Siciliano, "A solution algorithm to the inverse kinematic problem for redundant manipulators," *IEEE Journal on Robotics and Automation*, vol. 4, no. 4, pp. 403–410, 1988.
- [107] R. Alexander, "A minimum energy cost hypothesis for human arm trajectories," *Biological Cybernetics*, vol. 76, no. 2, pp. 97–105, 1997.
- [108] K. Ohta, M. M. Svinin, Z. Luo, S. Hosoe, and R. Laboissiere, "Optimal trajectory formation of constrained human arm reaching movements," *Biological Cybernetics*, vol. 91, no. 1, pp. 23–36, 2004.
- [109] D. Fraser and J. Potter, "The optimum linear smoother as a combination of two optimum linear filters," *IEEE Transactions on Automatic Control*, vol. 14, no. 4, pp. 387–390, 1969.
- [110] Y. Uno, M. Kawato, and R. Suzuki, "Formation and control of optimal trajectory in human multijoint arm movement," *Biological Cybernetics*, vol. 61, no. 2, pp. 89–101, 1989.
- [111] N. J. La Delfa and J. R. Potvin, "The arm force field method to predict manual arm strength based on only hand location and force direction," *Applied Ergonomics*, vol. 59, pp. 410–421, 2017.
- [112] V. Dietz and T. Sinkjaer, "Spastic movement disorder: impaired reflex function and altered muscle mechanics," *The Lancet Neurology*, vol. 6, no. 8, pp. 725–733, 2007.
- [113] J. F. Veneman, R. Kruidhof, E. E. Hekman, R. Ekkelenkamp, E. H. Van Asseldonk, and H. Van Der Kooij, "Design and evaluation of the LOPES exoskeleton robot for interactive gait rehabilitation," *IEEE Transactions on Neural Systems and Rehabilitation Engineering*, vol. 15, no. 3, pp. 379–386, 2007.
- [114] F. Vicentini, N. Pedrocchi, M. Malosio, and L. M. Tosatti, "Safenet: A methodology for integrating general-purpose unsafe devices in safe-robot rehabilitation systems," *Computer Methods and Programs in Biomedicine*, vol. 116, no. 2, pp. 156–168, 2014.

- [115] M. R. Tucker and R. Gassert, “Differential-damper topologies for actuators in rehabilitation robotics,” in *Engineering in Medicine and Biology Society (EMBC), 2012 Annual International Conference of the IEEE*. IEEE, 2012, pp. 3081–3085.
- [116] P. Beckerle, T. Verstraten, G. Mathijssen, R. Furnémont, B. Vanderborght, and D. Lefeber, “Series and parallel elastic actuation: Influence of operating positions on design and control,” *IEEE/ASME Transactions on Mechatronics*, vol. 22, no. 1, pp. 521–529, 2016.
- [117] N. Paine, S. Oh, and L. Sentis, “Design and control considerations for high-performance series elastic actuators,” *IEEE/ASME Transactions on Mechatronics*, vol. 19, no. 3, pp. 1080–1091, 2013.
- [118] H. Woo, B. Na, and K. Kong, “Design of a compact rotary series elastic actuator for improved actuation transparency and mechanical safety,” in *2017 IEEE International Conference on Robotics and Automation (ICRA)*. IEEE, 2017, pp. 1872–1877.
- [119] D. Leach, F. Günther, N. Maheshwari, and F. Iida, “Linear multimodal actuation through discrete coupling,” *IEEE/ASME Transactions on Mechatronics*, vol. 19, no. 3, pp. 827–839, 2013.
- [120] M. Moradi, “A genetic-multivariable fractional order pid control to multi-input multi-output processes,” *Journal of Process Control*, vol. 24, no. 4, pp. 336–343, 2014.
- [121] Y. Song, X. Huang, and C. Wen, “Robust adaptive fault-tolerant pid control of mimo nonlinear systems with unknown control direction,” *IEEE Transactions on Industrial Electronics*, vol. 64, no. 6, pp. 4876–4884, 2017.
- [122] R. M. Hirschorn, “Generalized sliding-mode control for multi-input nonlinear systems,” *IEEE Transactions on Automatic Control*, vol. 51, no. 9, pp. 1410–1422, 2006.
- [123] Y. Chang, “Adaptive sliding mode control of multi-input nonlinear systems with perturbations to achieve asymptotical stability,” *IEEE Transactions on Automatic Control*, vol. 54, no. 12, pp. 2863–2869, 2009.
- [124] H. Deng, Z. Xu, and H.-X. Li, “A novel neural internal model control for multi-input multi-output nonlinear discrete-time processes,” *Journal of Process Control*, vol. 19, no. 8, pp. 1392–1400, 2009.
- [125] J. S. Mehling, “Impedance control approaches for series elastic actuators,” Ph.D. dissertation, 2015.
- [126] Z. Huang, C. Zhang, Y. Zhang, and G. Zhang, “A data-driven online adp control method for nonlinear system based on policy iteration and nonlinear mimo decoupling adrc,” *Neurocomputing*, vol. 310, pp. 28–37, 2018.

- [127] C. Zhao, D. Li, J. Cui, and L. Tian, “Decentralized low-order adrc design for mimo system with unknown order and relative degree,” *Personal and Ubiquitous Computing*, vol. 22, no. 5-6, pp. 987–1004, 2018.
- [128] Z.-H. Wu and B.-Z. Guo, “Approximate decoupling and output tracking for mimo nonlinear systems with mismatched uncertainties via adrc approach,” *Journal of the Franklin Institute*, vol. 355, no. 9, pp. 3873–3894, 2018.
- [129] C. Lv, G. Huang, Z. Ouyang, J. Chen, and L. Bao, “Output regulation for a class of mimo uncertain stochastic nonlinear systems by active disturbance rejection control approach,” *Mathematical Problems in Engineering*, vol. 2019, 2019.
- [130] D.-H. Kim and J.-H. Oh, “Hysteresis modeling for torque control of an elastomer series elastic actuator,” *IEEE/ASME Transactions on Mechatronics*, 2019.
- [131] M. Malosio, G. Spagnuolo, A. Prini, L. M. Tosatti, and G. Legnani, “Principle of operation of rotwwc-vsa, a multi-turn rotational variable stiffness actuator,” *Mechanism and Machine Theory*, vol. 116, pp. 34–49, 2017.
- [132] Q. Zhu, Y. Mao, R. Xiong, and J. Wu, “Adaptive torque and position control for a legged robot based on a series elastic actuator,” *International Journal of Advanced Robotic Systems*, vol. 13, no. 1, p. 26, 2016.
- [133] S. Ozgoli and H. Taghirad, “Fuzzy error governor: A practical approach to counter actuator saturation on flexible joint robots,” *Mechatronics*, vol. 19, no. 6, pp. 993–1002, 2009.
- [134] B.-Z. Guo and Z.-L. Zhao, “On convergence of the nonlinear active disturbance rejection control for mimo systems,” *SIAM Journal on Control and Optimization*, vol. 51, no. 2, pp. 1727–1757, 2013.
- [135] J. Han, “From pid to active disturbance rejection control,” *IEEE transactions on Industrial Electronics*, vol. 56, no. 3, pp. 900–906, 2009.
- [136] J. Wang, S. Dodds, and W. Bailey, “Guaranteed rates of convergence of a class of pd controllers for trajectory tracking problems of robotic manipulators with dynamic uncertainties,” *IEE Proceedings-Control Theory and Applications*, vol. 143, no. 2, pp. 186–190, 1996.
- [137] Y. Huang and W. Xue, “Active disturbance rejection control: methodology and theoretical analysis,” *ISA Transactions*, vol. 53, no. 4, pp. 963–976, 2014.
- [138] G. Wu, L. Sun, and K. Y. Lee, “Disturbance rejection control of a fuel cell power plant in a grid-connected system,” *Control Engineering Practice*, vol. 60, pp. 183–192, 2017.
- [139] B. Ahi and A. Nobakhti, “Hardware implementation of an adrc controller on a gimbal mechanism,” *IEEE Transactions on Control Systems Technology*, 2017.

- [140] H.-L. Xing, J.-H. Jeon, K. Park, and I.-K. Oh, “Active disturbance rejection control for precise position tracking of ionic polymer–metal composite actuators,” *IEEE/ASME Transactions on Mechatronics*, vol. 18, no. 1, pp. 86–95, 2013.
- [141] Z.-L. Zhao and B.-Z. Guo, “On active disturbance rejection control for nonlinear systems using time-varying gain,” *European Journal of Control*, vol. 23, pp. 62–70, 2015.
- [142] K. Hu, X.-f. Zhang, and C.-b. Liu, “Unmanned underwater vehicle depth adrc based on genetic algorithm near surface,” *Acta Armamentarii*, vol. 34, no. 2, pp. 217–222, 2013.
- [143] H. Geng, H. Yang, Y. Zhang, and H. Chen, “Auto-disturbances-rejection controller design and it’s parameter optimization for aircraft longitudinal attitude,” *Journal of System Simulation*, vol. 22, no. 1, pp. 89–91, 2010.
- [144] F. Li, Z. Zhang, A. Armaou, Y. Xue, S. Zhou, and Y. Zhou, “Study on adrc parameter optimization using cpso for clamping force control system,” *Mathematical Problems in Engineering*, vol. 2018, 2018.
- [145] G. Hou, M. Wang, L. Gong, and J. Zhang, “Parameters optimization of adrc based on adaptive cpso algorithm and its application in main-steam temperature control system,” in *2018 13th IEEE Conference on Industrial Electronics and Applications (ICIEA)*. IEEE, 2018, pp. 497–501.
- [146] R.-l. Wang, B.-c. Lu, Y.-l. Hou, and Q. Gao, “Passivity-based control for rocket launcher position servo system based on adrc optimized by ipso-bp algorithm,” *Shock and Vibration*, vol. 2018, 2018.
- [147] Z. Yin, C. Du, J. Liu, X. Sun, and Y. Zhong, “Research on autodisturbance-rejection control of induction motors based on an ant colony optimization algorithm,” *IEEE Transactions on Industrial Electronics*, vol. 65, no. 4, pp. 3077–3094, 2018.
- [148] Y. Zhang, C. Fan, F. Zhao, Z. Ai, and Z. Gong, “Parameter tuning of adrc and its application based on cccsa,” *Nonlinear Dynamics*, vol. 76, no. 2, pp. 1185–1194, 2014.
- [149] D. Kalyanmoy *et al.*, *Multi objective optimization using evolutionary algorithms*. John Wiley and Sons, 2001.
- [150] K. Deb and D. Saxena, “Searching for pareto-optimal solutions through dimensionality reduction for certain large-dimensional multi-objective optimization problems,” in *Proceedings of the World Congress on Computational Intelligence (WCCI-2006)*, 2006, pp. 3352–3360.
- [151] J. A. Hernandez Mejia, O. Schütze, O. Cuate, A. Lara, and K. Deb, “Rds-nsga-ii: a memetic algorithm for reference point based multi-objective optimization,” *Engineering Optimization*, vol. 49, no. 5, pp. 828–845, 2017.

- [152] K. Deb and H. Jain, “An evolutionary many-objective optimization algorithm using reference-point-based nondominated sorting approach, part i: Solving problems with box constraints.” *IEEE Trans. Evolutionary Computation*, vol. 18, no. 4, pp. 577–601, 2014.
- [153] G. C. Ciro, F. Dugardin, F. Yalaoui, and R. Kelly, “A nsga-ii and nsga-iii comparison for solving an open shop scheduling problem with resource constraints,” *IFAC-PapersOnLine*, vol. 49, no. 12, pp. 1272–1277, 2016.
- [154] Y. Yuan, H. Xu, and B. Wang, “An improved nsga-iii procedure for evolutionary many-objective optimization,” in *Proceedings of the 2014 Annual Conference on Genetic and Evolutionary Computation*. ACM, 2014, pp. 661–668.
- [155] M. Elarbi, S. Bechikh, A. Gupta, L. B. Said, and Y.-S. Ong, “A new decomposition-based nsga-ii for many-objective optimization,” *IEEE Transactions on Systems, Man, and Cybernetics: Systems*, vol. 48, no. 7, pp. 1191–1210, 2018.
- [156] H. Li and Q. Zhang, “Multiobjective optimization problems with complicated pareto sets, moea/d and nsga-ii,” *IEEE Transactions on Evolutionary Computation*, vol. 13, no. 2, pp. 284–302, 2008.
- [157] H. Ishibuchi, Y. Setoguchi, H. Masuda, and Y. Nojima, “Performance of decomposition-based many-objective algorithms strongly depends on pareto front shapes,” *IEEE Transactions on Evolutionary Computation*, vol. 21, no. 2, pp. 169–190, 2016.
- [158] I. Das and J. E. Dennis, “Normal-boundary intersection: A new method for generating the pareto surface in nonlinear multicriteria optimization problems,” *SIAM Journal on Optimization*, vol. 8, no. 3, pp. 631–657, 1998.
- [159] K. Deb and D. Deb, “Analysing mutation schemes for real-parameter genetic algorithms,” *International Journal of Artificial Intelligence and Soft Computing*, vol. 4, no. 1, pp. 1–28, 2014.
- [160] K. Kumar, “Real-coded genetic algorithms with simulated binary crossover: studies on multimodal and multiobjective problems,” *Complex Systems*, vol. 9, pp. 431–454, 1995.
- [161] R. B. Agrawal, K. Deb, and R. Agrawal, “Simulated binary crossover for continuous search space,” *Complex Systems*, vol. 9, no. 2, pp. 115–148, 1995.
- [162] Z. Zhao, B. Liu, C. Zhang, and H. Liu, “An improved adaptive nsga-ii with multi-population algorithm,” *Applied Intelligence*, pp. 1–12, 2018.
- [163] A. Calanca and P. Fiorini, “Human-adaptive control of series elastic actuators,” *Robotica*, vol. 32, no. 8, pp. 1301–1316, 2014.

- [164] K. Kong, J. Bae, and M. Tomizuka, "Control of rotary series elastic actuator for ideal force-mode actuation in human-robot interaction applications," *IEEE/ASME Transactions on Mechatronics*, vol. 14, no. 1, pp. 105–118, 2009.
- [165] G. Smoljkic, G. Borghesan, D. Reynaerts, J. De Schutter, J. Vander Sloten, and E. Vander Poorten, "Constraint-based interaction control of robots featuring large compliance and deformation," *IEEE Transactions on Robotics*, vol. 31, no. 5, pp. 1252–1260, 2015.
- [166] Y. She, D. Meng, J. Cui, and H.-J. Su, "On the impact force of human-robot interaction: Joint compliance vs. link compliance," in *2017 IEEE International Conference on Robotics and Automation (ICRA)*. IEEE, 2017, pp. 6718–6723.
- [167] J. Kim, A. Alspach, and K. Yamane, "3d printed soft skin for safe human-robot interaction," in *2015 IEEE/RSJ International Conference on Intelligent Robots and Systems (IROS)*. IEEE, 2015, pp. 2419–2425.
- [168] M. Safeea and P. Neto, "Minimum distance calculation using laser scanner and imus for safe human-robot interaction," *Robotics and Computer-Integrated Manufacturing*, vol. 58, pp. 33–42, 2019.
- [169] P. Neto, M. Simão, N. Mendes, and M. Safeea, "Gesture-based human-robot interaction for human assistance in manufacturing," *The International Journal of Advanced Manufacturing Technology*, vol. 101, no. 1-4, pp. 119–135, 2019.

Appendix

ADRC Algorithm

The three extended state observers can be determined from the equalities: $\bar{x}_1^1 = \theta_m$, $\bar{x}_1^2 = \theta_b$, and $\bar{x}_1^3 = \theta_s$. The systems of equations for the subsystems are structured as follows:
Motor subsystem:

$$\begin{cases} \dot{\bar{x}}_1^1 = \bar{x}_2^1 \\ \dot{\bar{x}}_2^1 = -\frac{k_s}{J_m}\bar{x}_1^1 - \frac{b_m}{J_m}\bar{x}_2^1 + \frac{k_s}{J_m}\bar{x}_3^1 + D^1(t) + f_m(t, \Theta)V_m \\ y^1 = \bar{x}_1^1 \end{cases} \quad (1)$$

Brake subsystem:

$$\begin{cases} \dot{\bar{x}}_1^2 = \bar{x}_2^2 \\ \dot{\bar{x}}_2^2 = \frac{J_u k_s}{J}x_1^1 + \frac{J_s k_u}{J}x_1^2 + \frac{J_u(2b_d+b_b) - J_s(4b_d+4b_b-b_u)}{J}x_2^2 + \frac{J_s k_u - J_u k_s}{J}x_1^3 \\ + \frac{J_s(4b_d+b_u) - J_u(b_s+2b_d)}{J}x_2^3 + D^2(t) + f_{b1}(t, \Theta)V_b \\ y^2 = \bar{x}_1^2 \end{cases} \quad (2)$$

Spring subsystem:

$$\begin{cases} \dot{\bar{x}}_1^3 = \bar{x}_2^3 \\ \dot{\bar{x}}_2^3 = \frac{(4J_b - J_u)k_s}{J}x_1^1 + \frac{J_b k_u}{J}x_1^2 + \frac{J_b(4b_d+b_u) - J_u(2b_d+b_b)}{J}x_2^2 + \frac{J_b k_u - 4J_b k_s + J_u k_s}{J}x_1^3 \\ + \frac{J_u(b_s+2b_d) + J_b(b_u - 4b_s - 4b_b)}{J}x_2^3 + D^3(t) + f_{b2}(t, \Theta)V_b \\ y^3 = \bar{x}_1^3 \end{cases} \quad (3)$$

where $J = 4J_s J_b - J_u J_s - J_u J_b$. This can be converted to three extended state variables, each with their own total disturbance terms \bar{x}_3^i . The new system of equations become:

Motor subsystem:

$$\begin{cases} \dot{\bar{x}}_1^1 = \bar{x}_2^1 \\ \dot{\bar{x}}_2^1 = \bar{x}_3^1 + \frac{K_m K_v}{J_m R_a} V_m \\ y^1 = \bar{x}_1^1, \\ \bar{x}_3^1 = -\frac{k_s}{J_m}\bar{x}_1^1 - \frac{b_m}{J_m}\bar{x}_2^1 + \frac{k_s}{J_m}\bar{x}_3^1 + D^1(t) + \left(f_m(t, \Theta) - \frac{K_m K_v}{J_m R_a} \right) V_m \end{cases} \quad (4)$$

The linear approximation of the input function in this case is $f_m(t, \Theta) \cong \frac{K_m K_v}{J_m R_a}$. Therefore, $\bar{b}^1 = \frac{K_m K_v}{J_m R_a}$. Similarly for the brake subsystem:

$$\left\{ \begin{array}{l} \dot{\bar{x}}_1^2 = \bar{x}_2^2 \\ \dot{\bar{x}}_2^2 = \bar{x}_3^2 + \frac{K_h(J_u - 4J_s)}{R_b J} V_b \\ y^2 = \bar{x}_1^2, \\ \bar{x}_3^1 = \frac{J_u k_s}{J} x_1^1 + \frac{J_s k_u}{J} x_2^1 + \frac{J_u(2b_d + b_b) - J_s(4b_d + 4b_b - b_u)}{J} x_2^2 + \frac{J_s k_u - J_u k_s}{J} x_1^3 \\ \quad + \frac{J_s(4b_d + b_u) - J_u(b_s + 2b_d)}{J} x_2^3 + D^2(t) + \left(f_{b1}(t, \Theta) - \frac{K_h(J_u - 4J_s)}{R_b J} \right) V_b \end{array} \right. \quad (5)$$

The linear approximation of the input function in this case is $f_{b1}(t, \Theta) \cong \frac{K_h(J_u - 4J_s)}{R_b J}$. Therefore, $\bar{b}^2 = \frac{K_h(J_u - 4J_s)}{R_b J}$. Finally for the spring subsystem:

$$\left\{ \begin{array}{l} \dot{\bar{x}}_1^3 = \bar{x}_2^3 \\ \dot{\bar{x}}_2^3 = \bar{x}_3^3 - \frac{K_h J_u}{R_b J} V_b \\ y^3 = \bar{x}_1^3, \\ \bar{x}_3^1 = \frac{(4J_b - J_u)k_s}{J} x_1^1 + \frac{J_b k_u}{J} x_2^1 + \frac{J_b(4b_d + b_u) - J_u(2b_d + b_b)}{J} x_2^2 + \frac{J_b k_u - 4J_b k_s + J_u k_s}{J} x_1^3 \\ \quad + \frac{J_u(b_s + 2b_d) + J_b(b_u - 4b_s - 4b_b)}{J} x_2^3 + D^3(t) + \left(f_{b2}(t, \Theta) + \frac{K_h J_u}{R_b J} \right) V_b \end{array} \right. \quad (6)$$

The linear approximation of the input function in this case is $f_{b2}(t, \Theta) \cong -\frac{K_h J_u}{R_b J}$. Therefore, $\bar{b}^3 = -\frac{K_h J_u}{R_b J}$. The three extended state observers for the actuator are defined by:

Motor subsystem:

$$\left\{ \begin{array}{l} \hat{x}_1^1 = \hat{x}_2^1 - \beta_{01}^1 g_1^1(\theta_m, \theta_b, \theta_s, \theta_{bk}, \hat{y}^1(t)) \\ \hat{x}_2^1 = \hat{x}_3^1 - \beta_{02}^1 g_2^1(\theta_m, \theta_b, \theta_s, \theta_{bk}, \hat{y}^1(t)) + \bar{b}^1(t) u^1 \\ \hat{x}_3^1 = -\beta_{03}^1 g_3^1(\theta_m, \theta_b, \theta_s, \theta_{bk}, \hat{y}^1(t)) \\ \hat{y}^1 = \hat{x}_1^1 \end{array} \right. \quad (7)$$

where β_{0j}^1 , $j = 1, 2, 3$ are observer proportional coefficients selected by the designer. g_j^1 , $j = 1, 2, 3$ are observer error functions. The error function suggested from Han [135]

provide nonlinear observer error functions as:

$$\begin{aligned}
g_1^1(\theta_m, \theta_b, \theta_s, \theta_{bk}, \hat{y}^1(t)) &= (\hat{x}_1^1 - x_1^1) = ((\hat{\theta}_m + \hat{\theta}_{bk}) - \theta_m) \\
g_2^1(\theta_m, \theta_b, \theta_s, \theta_{bk}, \hat{y}^1(t)) &= fal(\hat{x}_1^1 - x_1^1, \alpha_1^1, h) = fal(\hat{x}_1^1 - x_1^1, 0.5, h) \\
g_3^1(\theta_m, \theta_b, \theta_s, \theta_{bk}, \hat{y}^1(t)) &= fal(\hat{x}_1^1 - x_1^1, \alpha_2^1, h) = fal(\hat{x}_1^1 - x_1^1, 0.25, h)
\end{aligned}$$

where the fal function is defined in Equation (4.25). Similarly the brake and spring subsystems, respectively, are:

$$\left\{ \begin{array}{l}
\hat{x}_1^2 = \hat{x}_2^2 - \beta_{01}^2 g_1^2(\theta_m, \theta_b, \theta_s, \theta_{bk}, \hat{y}^2(t)) \\
\hat{x}_2^2 = \hat{x}_3^2 - \beta_{02}^2 g_2^2(\theta_m, \theta_b, \theta_s, \theta_{bk}, \hat{y}^2(t)) + \bar{b}^2(t) u^2 \\
\hat{x}_3^2 = -\beta_{03}^2 g_3^2(\theta_m, \theta_b, \theta_s, \theta_{bk}, \hat{y}^2(t)) \\
\hat{y}^2 = \hat{x}_1^2 \\
g_1^2(\theta_m, \theta_b, \theta_s, \theta_{bk}, \hat{y}^2(t)) = (\hat{x}_1^2 - x_1^2) = (\hat{\theta}_b - \theta_b) \\
g_2^2(\theta_m, \theta_b, \theta_s, \theta_{bk}, \hat{y}^2(t)) = fal(\hat{x}_1^2 - x_1^2, \alpha_1^2, h) = fal(\hat{x}_1^2 - x_1^2, 0.5, h) \\
g_3^2(\theta_m, \theta_b, \theta_s, \theta_{bk}, \hat{y}^2(t)) = fal(\hat{x}_1^2 - x_1^2, \alpha_2^2, h) = fal(\hat{x}_1^2 - x_1^2, 0.25, h)
\end{array} \right.$$

$$\left\{ \begin{array}{l}
\hat{x}_1^3 = \hat{x}_2^3 - \beta_{01}^3 g_1^3(\theta_m, \theta_b, \theta_s, \theta_{bk}, \hat{y}^3(t)) \\
\hat{x}_2^3 = \hat{x}_3^3 - \beta_{02}^3 g_2^3(\theta_m, \theta_b, \theta_s, \theta_{bk}, \hat{y}^3(t)) + \bar{b}^3(t) u^3 \\
\hat{x}_3^3 = -\beta_{03}^3 g_3^3(\theta_m, \theta_b, \theta_s, \theta_{bk}, \hat{y}^3(t)) \\
\hat{y}^3 = \hat{x}_1^3 \\
g_1^3(\theta_m, \theta_b, \theta_s, \theta_{bk}, \hat{y}^3(t)) = (\hat{x}_1^3 - x_1^3) = ((\hat{\theta}_s + \hat{\theta}_{bk}) - \theta_s) \\
g_2^3(\theta_m, \theta_b, \theta_s, \theta_{bk}, \hat{y}^3(t)) = fal(\hat{x}_1^3 - x_1^3, \alpha_1^3, h) = fal(\hat{x}_1^3 - x_1^3, 0.5, h) \\
g_3^3(\theta_m, \theta_b, \theta_s, \theta_{bk}, \hat{y}^3(t)) = fal(\hat{x}_1^3 - x_1^3, \alpha_2^3, h) = fal(\hat{x}_1^3 - x_1^3, 0.25, h)
\end{array} \right.$$

Input Contribution

The total overall control law for the system can be described as follows:

$$u_q(t) = - \left(p_q^1 \frac{\hat{x}_3^1(t) - u_p^1}{\bar{b}^1} + p_q^2 \frac{\hat{x}_3^2(t) - u_p^2}{\bar{b}^2} + p_q^3 \frac{\hat{x}_3^3(t) - u_p^3}{\bar{b}^3} \right) \quad (8)$$

where $u_q(t)$ is the overall control input to the plant, $q = 1$ relates to the motor voltage and $q = 2$ relates to the brake input voltage, p_q^i , $i = 1, 2, 3$ are proportional input contribution

gains, and u_p^i , $i = 1, 2, 3$ are the proposed input contribution for each of the three nonlinear feedback combiners. Depending on the type of feedback combiner chosen, the overall control law could be described as any of the following equations:

$$\begin{aligned}
u_q(t) = p_q^1 & \frac{k_1^1((\hat{\theta}_m + \hat{\theta}_{bk}) - \theta_m) + k_2^1(\dot{\hat{\theta}}_m - \dot{\theta}_m) - \hat{x}_3^1(t)}{\bar{b}^1} \\
& + p_q^2 \frac{k_1^2(\hat{\theta}_b - \theta_b) + k_2^2(\dot{\hat{\theta}}_b - \dot{\theta}_b) - \hat{x}_3^2(t)}{\bar{b}^2} \\
& + p_q^3 \frac{k_1^3((\hat{\theta}_s - \hat{\theta}_{bk}) - \theta_s) + k_2^3(\dot{\hat{\theta}}_s - \dot{\theta}_s) - \hat{x}_3^3(t)}{\bar{b}^3} \quad (9)
\end{aligned}$$

$$\begin{aligned}
u_q(t) = p_q^1 & \frac{(k_1^1 \text{fal}((\hat{\theta}_m + \hat{\theta}_{bk}) - \theta_m, \gamma_1^1, h) + k_2^1 \text{fal}(\dot{\hat{\theta}}_m - \dot{\theta}_m, \gamma_2^1, h)) - \hat{x}_3^1(t)}{\bar{b}^1} \\
& + p_q^2 \frac{(k_1^2 \text{fal}(\hat{\theta}_b - \theta_b, \gamma_1^2, h) + k_2^2 \text{fal}(\dot{\hat{\theta}}_b - \dot{\theta}_b, \gamma_2^2, h)) - \hat{x}_3^2(t)}{\bar{b}^2} \\
& + p_q^3 \frac{(k_1^3 \text{fal}((\hat{\theta}_s - \hat{\theta}_{bk}) - \theta_s, \gamma_1^3, h) + k_2^3 \text{fal}(\dot{\hat{\theta}}_s - \dot{\theta}_s, \gamma_2^3, h)) - \hat{x}_3^3(t)}{\bar{b}^3} \quad (10)
\end{aligned}$$

$$\begin{aligned}
u_q(t) = p_q^1 & \frac{-\text{fhan}((\hat{\theta}_m + \hat{\theta}_{bk}) - \theta_m, c^1(\dot{\hat{\theta}}_m - \dot{\theta}_m), r_1^1, h_1^1) - \hat{x}_3^1(t)}{\bar{b}^1} \\
& + p_q^2 \frac{-\text{fhan}(\hat{\theta}_b - \theta_b, c^2(\dot{\hat{\theta}}_b - \dot{\theta}_b), r_1^2, h_1^2) - \hat{x}_3^2(t)}{\bar{b}^2} \\
& + p_q^3 \frac{-\text{fhan}((\hat{\theta}_s - \hat{\theta}_{bk}) - \theta_s, c^3(\dot{\hat{\theta}}_s - \dot{\theta}_s), r_1^3, h_1^3) - \hat{x}_3^3(t)}{\bar{b}^3} \quad (11)
\end{aligned}$$

The first and second equations above relate to combined linear and nonlinear PD controllers, respectively. Note that the three equations above are suggested, however, many possible control laws exist.

ADRC Optimization Gains

Table 1: Optimizable Gains: Active Disturbance Rejection Controller

Gain	Description	Bounds [min max]
Transient Profile Generator Gains		
r_0^i	Transient profile aggressiveness factor i	[0, 1000]
h_0^i	Transient profile precision coefficient i	[0, 1]
Observer Gains for Dual Integral Plants		
β_{01}^i	Observer i proportional gain 1	[0, 10]
β_{02}^i	Observer i proportional gain 2	[1, 1000]
β_{03}^i	Observer i proportional gain 3	[1, 10000]
α_1^i	Observer i nonlinear convergence rate 1	[0, 1]
α_2^i	Observer i nonlinear convergence rate 2	[0, 1]
Input Aggregation Gains (i th Input, j th NFC)		
p_i^j	Contribution gain for input i from the j th NFC	[0, 1]
PD Controller		
k_1^i	Proportional error gain for subsystem i	[0, 10000]
k_2^i	Derivative error gain for subsystem i	[0, 10000]
Nonlinear PD Controller		
k_1^i	Proportional error gain for subsystem i	[0, 10000]
k_2^i	Derivative error gain for subsystem i	[0, 10000]
γ_1^i	Feedback combiner i nonlinear convergence rate 1	[0, 1]
γ_2^i	Feedback combiner i nonlinear convergence rate 2	[0, 1]
Nonlinear Controller		
r_1^i	Aggressiveness factor for subsystem i	[0, 100]
h_1^i	Precision coefficient for subsystem i	[0, 1]

Simulation Output

Generation 500: Best Results

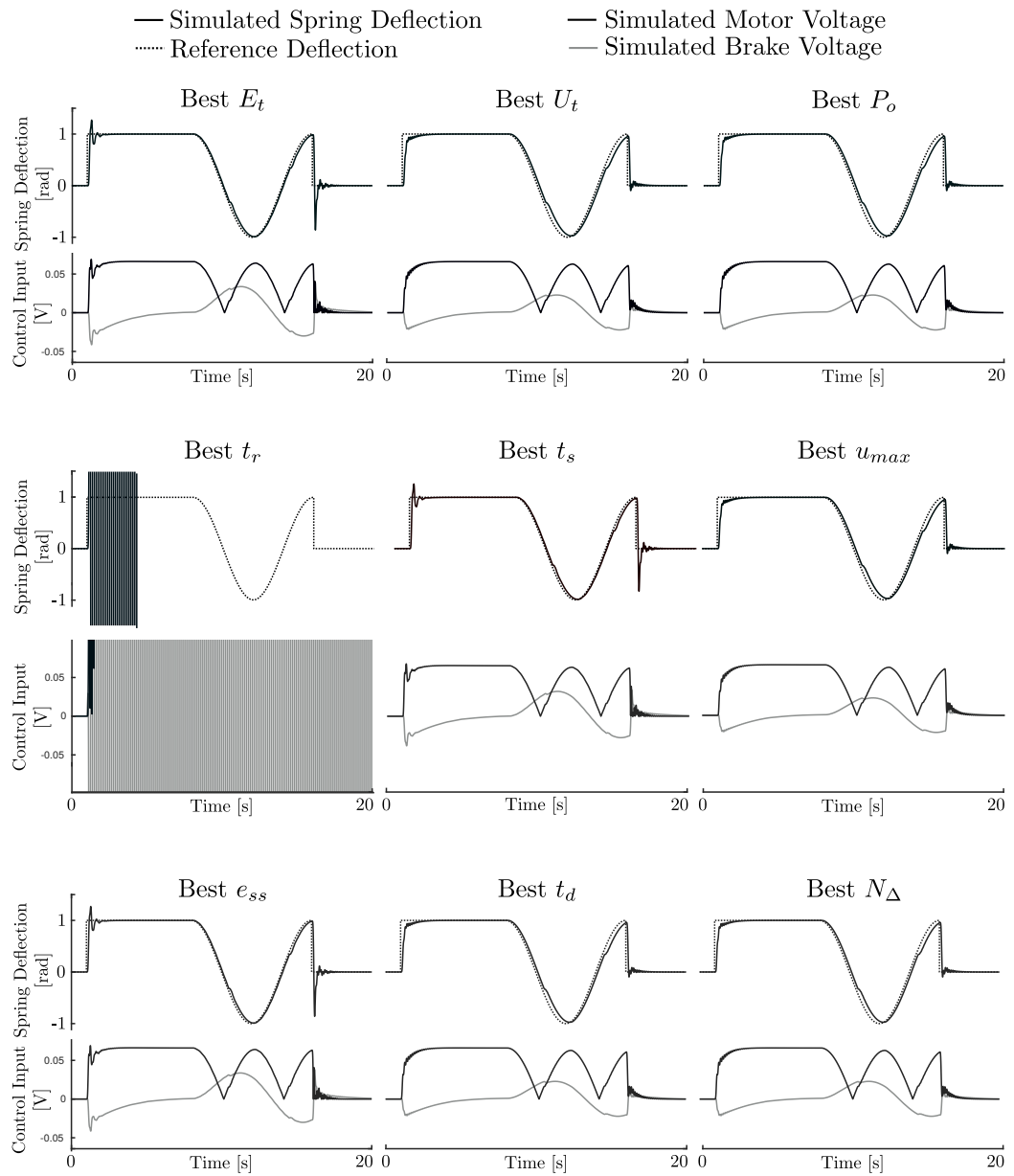


Figure 2: Best performing objectives after 500 generations.